LBL-36547
UC-404

Center for Advanced Materials

CAM

Structural Influences on the Work Hardening Behavior of Aluminum

D. Chu
(Ph.D. Thesis)

December 1994

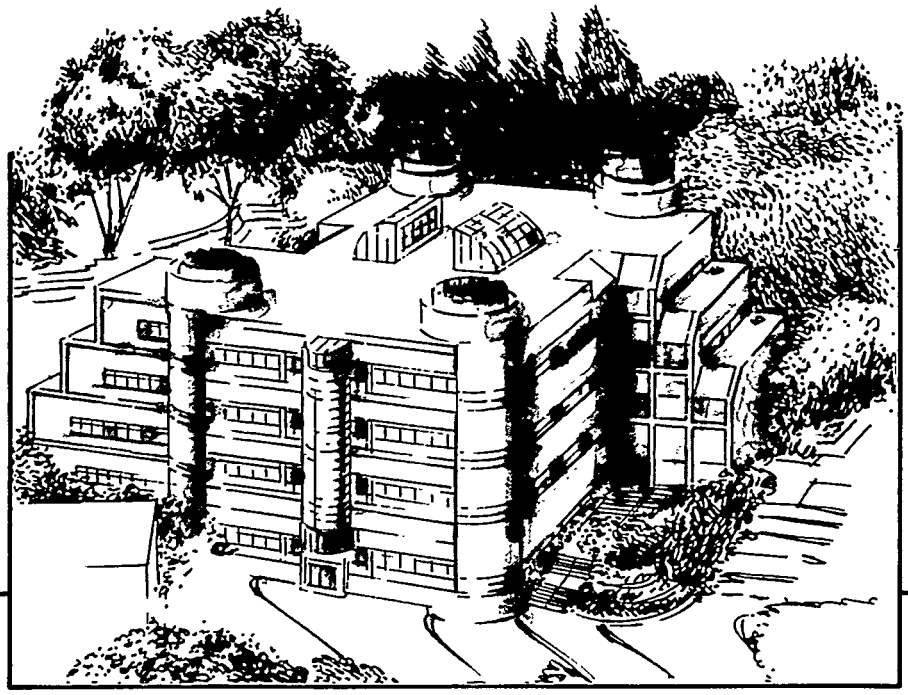

Materials and Chemical Sciences Division

Lawrence Berkeley Laboratory • University of California

ONE CYCLOTRON ROAD, BERKELEY, CA 94720 • (415) 486-4755

Prepared for the U.S. Department of Energy under Contract DE-AC03-76SF00098

LBL-36547
UC-404

Structural Influences on the Work Hardening Behavior of Aluminum

David Chu
Ph.D. Thesis

Materials Science and Mineral Engineering Department
University of California, Berkeley

and

Center for Advanced Materials
Materials Sciences Division
Lawrence Berkeley Laboratory
University of California
Berkeley, CA 94720

December 1994

This work was supported by Rockwell International and the Director, Office of Energy Research, Office of Basic Energy Sciences, Materials Sciences Division, of the U.S. Department of Energy under Contract No. DE-AC03-76SF00098. D. Chu was supported by a Rockwell International Fellowship.

Structural Influences on the Work Hardening Behavior of Aluminum

David Chu

Ph.D. Dissertation

Abstract

The influence of various grain and subgrain morphologies on the low temperature work hardening behavior of pure aluminum is studied by means of a series of tensile tests. Plotting the work hardening rate as a function of true stress, the work hardening behavior is found to be separable into two distinct regimes. Both regimes are approximated by a line such that $\Theta = \Theta_0 - K_2\sigma$, where Θ_0 is the theoretical work hardening rate at zero stress and K_2 is related to the dynamic recovery rate. The first or early deformation regime exhibits greater values of Θ_0 and K_2 and can extend up to the first 10% strain of tensile deformation. The existence of this early deformation regime is contingent on the existence of a pre-existent dislocation substructure from a previous straining. The actual values of Θ_0 and K_2 associated with the early deformation regime are dependent on the strength and orientation of the pre-existent dislocation substructure relative to the new strain path. At high enough temperatures, this pre-existent dislocation substructure is annealed out, resulting in the near elimination of the early deformation regime.

In comparison, the latter regime is dominated by the initial grain and/or subgrain morphology and exhibit lower values of Θ_0 and K_2. The actual value of K_2 in the latter regime is strongly dependent on the existence of a subgrain morphology. Recrystallized or well-annealed microstructures exhibit greater values of K_2 than microstructures that remain partially or fully unrecrystallized. The higher K_2 value is indicative of a more rapid dynamic recovery rate and a greater degree of strain relaxation. The ability to achieve a more relaxed state produces a low-energy cellular dislocation substructure upon deformation. The introduction of subgrains hinders the evolution of a low-energy dislocation cell network, giving way to a more random distribution of the dislocation density. The lack of a cellular dislocation substructure, increases the difficulty of dynamic recovery processes, hence resulting in a lower value of K_2.

TABLE OF CONTENTS

TABLE CAPTIONS v

FIGURE CAPTIONS vii

ACKNOWLEDGEMENTS xiv

INTRODUCTION 1
- Motivation 1
- Applications 3
  - *Strength and Toughness of Structural Aluminum Alloys* 3
  - *Formability of Aluminum Alloys* 5
- Objective 6

THEORY 7
- Work Hardening Models: Fundamentals 7
  - *General Constitutive Law for Plasticity* 7
- Work Hardening Models: Single Parameter Models 9
  - *Kocks-Mecking Model* 9
  - *Kuhlmann-Wilsdorf Model: Mesh-Length Theory* 12
  - *Early Regime Work Hardening Models* 16
- Work Hardening Models: Influence of Structure 17
  - *Expansion from Single Crystal to Polycrystals* 17
  - *Influence of Grain, Subgrain, and Cell Size* 18
  - *Influence of Dislocation Substructure* 22
- Summary 24

EXPERIMENTAL PROCEDURE 25
- Materials and Microstructure 25
- Testing 26
- Transmission Electron Microscopy 27

EXPERIMENTAL RESULTS 28
- KSL Specimens 28
  - *Initial Microstructure* 28
  - *Tensile Properties* 28
  - *Tensile Behavior* 29
  - *Deformed Microstructure - Latter or Fully Plastic Regime* 31
  - *Deformed Microstructure - Early Regime* 32
- LBL Specimens 33
  - *Tensile Properties: LBL1 Specimens* 33
  - *Tensile Behavior: LBL1 Specimens* 34
  - *Tensile Properties: LBL2 Specimens* 35
  - *Tensile Behavior: LBL2 Specimens* 35

Additional Tests and Results 36
Reannealed Specimens 36
Pre-Compressed Specimens 37

DISCUSSION 40
Work Hardening Behavior 40
Latter or Fully Plastic Regime 40
Early Regime 42
Implications to Work Hardening Models 43
Kocks-Mecking Model 44
Kuhlmann-Wilsdorf Model 46
Early Regime 47
Implications to Mechanical Properties 48

FURTHER COMMENTS 50
Influence of Subgrains on the Work Hardening Behavior 50
Influence of Solutes on the Work Hardening Behavior 51
Influence of Precipitates on the Work Hardening Behavior 52

SUMMARY AND CONCLUSIONS 54

REFERENCES 56

TABLES 65

FIGURES 75

TABLE CAPTIONS

Table I: Temperatures used for annealing treatments. All specimens were held at specified temperature for 3 hours followed by a furnace cool.

Table II: Engineering tensile properties of KSL specimens (99.94% aluminum) in various annealing conditions.

Table III: Work hardening parameters for KSL specimens according to the Kocks-Mecking model (Equation (20)).

Table IV: Calculated Taylor factors for the microstructures tested in this work assuming only texture effects.

Table V: Engineering tensile properties of LBL1 specimens (99.96% aluminum) in various annealing conditions and orientations.

Table VI: Engineering tensile properties of LBL2 specimens (99.96% aluminum) in various orientations.

Table VII: Work hardening parameters for LBL specimens according to the Kocks-Mecking model (Equation (20)).

Table VIII: Work hardening parameters for LBL specimens according to the Kocks-Mecking model (Equation (20)). Reannealing of the recrystallized microstructure causes K_2 of the latter regime to decrease to a value approaching the value obtained for the recovered microstructure.

Table IX: Engineering tensile properties of KSL specimens (99.94% aluminum) in various annealing conditions.

Table X: Work hardening parameters for recrystallized and pre-compressed recrystallized microstructures according to the Kocks-Mecking model (Equation (20)). Pre-compression produces an early regime with a higher slope. The slope of the latter regime remains unchanged.

Table XI: Engineering tensile properties of KSL specimens (99.94% aluminum) in various annealing conditions.

Table XII: Work hardening parameters for recrystallized and pre-compressed recrystallized microstructures according to the Kocks-Mecking model (Equation (20)). Pre-compression produces an early regime with a higher slope. The slope of the latter regime remains unchanged.

Table XIII: Work hardening parameters for aluminum-magnesium specimens and pure aluminum specimens in the recrystallized and recovered condition according to the Kocks-Mecking model (Equation (20)). Dimensions in left column indicate grain sizes. Addition of magnesium causes K_2 to decrease to a value approaching the value obtained for the pure aluminum recovered microstructure.

Table XIV: Engineering tensile properties of aluminum-magnesium specimens and pure aluminum specimens in the recrystallized and recovered condition. Dimensions in left column indicate grain sizes. Addition of magnesium produces an increase in both strength and elongation. Note that the pure aluminum recovered microstructure exhibits the greatest yield strength. However, the higher work hardening rate achieved with the addition of magnesium produces greater ultimate strengths in the magnesium-bearing specimens.

FIGURE CAPTIONS

Figure 1: Schematic depicting the dependency of the strain to failure on the flow strength and work hardening rate: a) Dashed lines exhibit increase in the strain to failure resulting from an increase in the work hardening rate; b) Increase in yield strength may counteract this improvement in work hardening, resulting in a decrease in the strain to failure.

Figure 2: Schematic plot of the stress-strain curve for a single crystal oriented for single slip illustrating the three stages of work hardening.

Figure 3: Schematic illustrating the derivation of the dislocation storage rate in Equation (7). The edge dislocation moves a distance Λ through the cube under the applied shear stress τ.

Figure 4: Schematic illustrating the Kocks-Mecking model. Typical work hardening curve obtained from tensile tests is shown by the dashed line.

Figure 5: Schematic demonstrating the similarity between the physical description given by the Kocks-Mecking model in a) and the Mesh-Length theory in b). Note that the heterogeneity of the dislocations in the Mesh-Length theory results in a homogeneity in the dislocation tangles.

Figure 6: Schematic illustrating a multiple structure parameter model based on the foundation of the Kocks-Mecking model. Figure a) shows the two work hardening curves associated with two different structure parameters. Figure b) shows the bi-linear plot resulting from the addition of the two curves in Figure a). Figure c) and d) show the extension of Figures a) and b) to an n-parameter model as highlighted by the dashed and shaded line in Figure d).

Figure 7: Schematic illustrating the theoretical influence of texture on the work hardening behavior.

Figure 8: Schematic illustrating the influence of grain size on the work hardening behavior assuming no change in the evolution of the dislocation substructure after yielding.

Figure 9: a) Work hardening rate versus true stress plot for aluminum extrapolated from computer generated stress versus grain size (in μm) curves in reference 148, Figure 6a. Curves for smaller grain sizes are in bold to emphasize increase in work hardening slope. b) Schematic of extrapolated work hardening versus true stress plot highlighting the trend shown in a).

Figure 10: Schematic showing the stress-strain curves in a), and corresponding work hardening curves in b), for both positive and negative transients. In both a) and b), the bold line represents the curve of the second loading condition without prestraining.

Figure 11: Schematic illustration showing the dimensions of tensile specimens. All dimensions are in inches.

Figure 12: Optical micrographs of the four microstructures tested in this study. (XBB 9310-6739)

Figure 13: Stress-strain curves and work hardening curves for the two recrystallized specimens. Slight increase in flow stress difference with increasing strain in a) indicates increasing Hall-Petch slope with strain. This increase, however, does not significantly affect the slope of the work hardening curve. Compare b) with Figures 8 and 9.

Figure 14: Plot of the work hardening rate versus true stress for the four microstructures: unrecrystallized (URX), recovered (REC), partially recrystallized (PRX), and recrystallized (REX). Both the unrecrystallized and recovered microstructures exhibit the same work hardening behavior after approximately 200 MPa.

Figure 15: Stress-strain curves for the four microstructures: unrecrystallized (URX), recovered (REC), partially recrystallized (PRX), and recrystallized (REX). Both unrecrystallized and recovered specimens achieve the strength level, approximately 250 MPa, despite the large difference in elongation. The partially recrystallized microstructure appears to parallel the recrystallized microstructure at low strains and the recovered microstructure at high strains.

Figure 16: Schematic illustrating the results from the work hardening analysis on the four microstructures shown in Figures 14 and 15.

Figure 17: TEM micrograph highlighting a triple point grain boundary of the recrystallized microstructure prior to deformation. Except for the few artifacts left from the electropolishing and sample preparation, the microstructure is relatively absent of any internal structure. Zone axis is near $[0\bar{1}1]$. (XBB 9408-5013)

Figure 18: TEM micrograph of the recrystallized microstructure after deformation to a true stress of 178 MPa (25.8 ksi), approximately 26.8% true strain. Note the strong formation of a cellular dislocation structure. Zone axis is $[0\bar{1}1]$. (XBB 9408-5000)

Figure 19: TEM micrograph of the recrystallized microstructure after deformation to a true stress of 178 MPa (25.8 ksi), approximately 26.8% true strain. Note that the cell structure is elongated approximately 45° from the loading direction which is parallel to the initial rolling direction. Zone axis is near [0$\bar{1}$1]. (XBB 9408-5001)

Figure 20: TEM micrograph of the recrystallized microstructure after deformation to a true stress of 168 MPa (24.4 ksi), approximately 22.3% true strain. Micrograph shows that the dislocation cell walls lie parallel to the (111) and (200) planes. Zone axis is [0$\bar{1}$1]. (XBD 9408-5006)

Figure 21: TEM micrograph of the recrystallized microstructure after deformation to a true stress of 178 MPa (25.8 ksi), approximately 26.8% true strain. Micrograph shows an extreme case in which the cellular structure is relatively symmetrical in configuration. Note the sharpness of the grain boundary (marked by arrows) suggesting the lack of grain boundary influence on the deformation process and evolution of the dislocation cell structure. Zone axis is [0$\bar{1}$1]. (XBD 9408-5002)

Figure 22: TEM micrograph of the recovered microstructure prior to deformation. Note the well developed subgrain morphology in contrast to the recrystallized microstructure in Figure 17. Zone axis is near [0$\bar{1}$1]. (XBB 9408-4997)

Figure 23: TEM micrograph of the recovered microstructure prior to deformation. Note the well developed subgrain morphology in contrast to the recrystallized microstructure in Figure 17. Zone axis is near [0$\bar{1}$1]. (XBB 9408-4996)

Figure 24: TEM micrograph of the recovered microstructure prior to deformation. Diffraction patterns show that the subgrain boundaries are low angle misorientations. The center of the [0$\bar{1}$1] zone axis is labelled by an O. Zone axis is near [0$\bar{1}$1]. (XBB 9408-5014)

Figure 25: TEM micrograph of the recovered microstructure prior to deformation. Note the existence of some dislocation substructure within the subgrain interior. Zone axis is near [0$\bar{1}$1]. (XBB 9408-4999)

Figure 26: TEM micrograph of the recovered microstructure prior to deformation. Note the existence of some dislocation substructure within the subgrain interior. Zone axis is near [0$\bar{1}$1]. (XBB 9408-4998)

Figure 27: TEM micrograph of the recovered microstructure after deformation to a true stress of 226 MPa (32.8 ksi), approximately 21.8% true strain. Note the more random dislocation arrangement compared to the recrystallized microstructure upon straining in Figures 18 through 21. The majority of dislocations appear to accumulate at the subgrain boundaries. Some regions (upper left) exhibit a more homogeneous dislocation arrangement. Zone axis is $[0\bar{1}1]$. (XBB 9408-4994)

Figure 28: TEM micrograph of the recovered microstructure after deformation to a true stress of 226 MPa (32.8 ksi), approximately 21.8% true strain. Note the strong accumulation of dislocations at the subgrain boundaries. Zone axis is $[0\bar{1}1]$. (XBB 9408-4993)

Figure 29: TEM micrograph of the recovered microstructure after deformation to a true stress of 226 MPa (32.8 ksi), approximately 21.8% true strain. The accumulation of dislocations is not as strong in this region as compared to Figure 28. However, the tendency for the dislocations to accumulate at the subgrain boundaries still exists. Zone axis is $[0\bar{1}1]$. (XBB 9408-4995)

Figure 30: TEM micrograph of the unrecrystallized microstructure after deformation to a true stress of 226 MPa (32.8 ksi), approximately 14.1% true strain. Similar to the recovered microstructure, the dislocations tend to accumulate at the subgrain boundaries. Some regions (upper left) exhibit a more homogeneous dislocation arrangement. Zone axis is $[0\bar{1}1]$. (XBB 9408-4990)

Figure 31: TEM micrograph of the unrecrystallized microstructure after deformation to a true stress of 226 MPa (32.8 ksi), approximately 14.1% true strain. Similar to the recovered microstructure, the dislocations tend to accumulate at the subgrain boundaries. Some regions (right hand side) exhibit a more homogeneous dislocation arrangement. Zone axis is $[0\bar{1}1]$. (XBB 9408-4988)

Figure 32: Optical micrograph of the partially recrystallized structure showing the evolution of deformation after a) 2% strain, b) 5% strain, c) 10% strain, and d) 15% strain. The recovered region is on the left side of each micrograph. Note that the recovered region exhibits greater out-of-plane rotation than the recrystallized region. (XBB 9306-3999)

Figure 33: TEM micrograph of the unrecrystallized microstructure prior to deformation. Note the existence of both narrow (A) and wide (B) dislocation bands across the subgrain interior. Zone axis is near $[0\bar{1}1]$. (XBD 9408-5103)

Figure 34: Schematic illustrating the difference between TEM specimen orientations between this study (A), and references 56, 75, 76, and 79 (B).

Figure 35: TEM micrographs of the unrecrystallized microstructure prior to deformation. Diffraction analysis of the wide dislocation band, indicated by the arrow, reveals the existence of at least two slip systems. The upper micrograph is offset to the left. Zone axis is near $[0\bar{1}1]$. (XBD 9408-5104)

Figure 36: TEM micrograph of the unrecrystallized microstructure after deformation to a true stress of 178 MPa (25.8 ksi), approximately 4.1% true strain. Much of the internal dislocation structure has dissolved (compare to Figures 30 and 31). Zone axis is $[0\bar{1}1]$. (XBB 9408-5101)

Figure 37: TEM micrograph of the recovered microstructure after deformation to a true stress of 178 MPa (25.8 ksi), approximately 10.1% true strain. Note the high degree of strain contrast indicating the high deformation activity at the subgrain boundaries. Dislocations generated from the subgrain boundaries can be seen at the arrow. Zone axis is $[0\bar{1}1]$. (XBD 9408-4989)

Figure 38: TEM micrograph of the recovered microstructure after deformation to a true stress of 178 MPa (25.8 ksi), approximately 10.1% true strain. The early stages of a dislocation network can be seen (upper right). Dislocations generated from the subgrain boundaries can be seen at the arrow. Zone axis is $[0\bar{1}1]$. (XBD 9408-4991)

Figure 39: TEM micrograph of the recovered microstructure after deformation to a true stress of 178 MPa (25.8 ksi), approximately 10.1% true strain. Diffraction analysis indicates that the dislocation network, indicated by the arrows, consists of dislocations generated from the subgrain boundary. Zone axis is $[0\bar{1}1]$. (XBD 9408-5099)

Figure 40: Plots of the work hardening rate versus true stress for LBL1 specimens in the recrystallized condition. Two curves represent specimens tested at different orientations relative to the rolling direction a) as tested and b) after recalculating the 45° plot ($\theta/1.05^2$ versus $\sigma/1.05$).

Figure 41: Plots of the work hardening rate versus true stress for LBL1 specimens in the unrecrystallized condition. Two curves represent specimens tested at different orientations relative to the rolling direction a) as tested and b) after recalculating the 90° plot ($\theta/1.08^2$ versus $\sigma/1.08$).

Figure 42: Plots of the work hardening rate versus true stress for LBL2 specimens in the unrecrystallized condition. Note the near parallel slope of the latter regimes of the 0° and 90° orientations.

Figure 43: Schematic illustrating the difference between the recovered and reannealed microstructures. Both microstructures contain subgrains. However, the manner by which these subgrains are achieved differ.

Figure 44: TEM micrograph of the reannealed microstructure prior to deformation. Note that the subgrains on the left are close in orientation with each other but exhibit a large misorientation across the grain boundary marked by arrows. Zone axis is near [001]. (XBD 9408-5010)

Figure 45: TEM micrograph of the reannealed microstructure prior to deformation. Most of the disocation cell structure has coalesced into subgrain boundaries. Lack of sharpness at the boundaries indicates an incomplete recovery process. Compare to Figures 18 through 21. Zone axis is near [001]. (XBB 9408-5009)

Figure 46: TEM micrograph of the reannealed microstructure prior to deformation. Most of the disocation cell structure has coalesced into subgrain boundaries. Lack of sharpness at the boundaries indicates an incomplete recovery process. Compare to Figures 18 through 21. Zone axis is near [001]. (XBB 9408-5008)

Figure 47: Plot of the work hardening rate versus true stress for the recovered (REC), recrystallized (REX), and reannealed (REN) microstructures. Slopes of the latter regime for the three microstructures are highlighted by the shaded lines. Note that the latter regime of the reannealed microstructure follows nearly parallel to the recovered microstructure.

Figure 48: TEM micrograph of the reannealed microstructure after deformation to a true stress of 189 MPa (27.4 ksi), approximately 25.1% true strain. Note the absence of a cellular dislocation structure. Dislocations accumulate at the subgrain boundaries similar to the recovered and unrecrystallized microstructure after deformation. Compare to Figures 27 through 31. Zone axis is [001]. (XBB 9408-5005)

Figure 49: TEM micrograph of the recovered microstructure after deformation to a true stress of 189 MPa (27.4 ksi), approximately 25.1% true strain. Note the absence of a cellular dislocation structure. Dislocations accumulate at the subgrain boundaries similar to the recovered and unrecrystallized microstructure after deformation. Compare to Figures 27 through 31. Zone axis is [001]. (XBB 9408-5004)

Figure 50: Schematic illustrating the strain path of the pre-compressed specimens. Compare to Figure 42.

Figure 51: Plot of the work hardening rate versus true stress for the recrystallized and the pre-compressed recrystallized microstructures. Slopes of the latter regime for the two microstructures are highlighted by the shaded lines. Note the existence of a greater early regime in the pre-compressed microstructure.

Figure 52: Plot of the work hardening rate versus true stress for the recovered and the pre-compressed recovered microstructures. Aside from a slight difference in the early regime, the work hardening curves for both microstructures are nearly identical.

Figure 53: Schematic illustrating the different evolutionary paths of the dislocation network. The cellular dislocation structure that develops in the recrystallized microstructure allows for a higher dynamic recovery rate and steeper drop in the work hardening rate with stress. The subgrain morphology inherent to the recovered and unrecrystallized microstructures eliminates the cellular dislocation structure, reducing the dynamic recovery rate.

Figure 54: Plot of the work hardening rate versus true stress for the recrystallized (REX) and recovered (REC) microstructures. Shaded lines are calculated using Equation (50). Note the excellent fit of the predicted work hardening behavior for the recovered microstructure.

Figure 55: Plot of the work hardening rate versus true stress for the magnesium-bearing solid solutions and pure aluminum samples in the recrystallized (REX) and recovered (REC) conditions. Shaded lines represent the linear approximations used to obtain the parameters in Table XIII. Note that the addition of solutes accomplishes the same effect as the introduction of subgrains.

Figure 56: Schematic illustrating the influence of precipitates on the very-early work hardening regime. An increase in the slope of the very-early work hardening regime will result in an increase in the uniform elongation (Equation (54)).

ACKNOWLEDGEMENTS

Thanks are extended to Trey Bradley, Ferdinand Bartels, and Choongun Kim for taking the time to discuss my results and provide helpful comments during the course of this study. Their ideas and suggestions during our many discussions repeatedly refocussed my sights whenever my own thoughts began to stray from the end goal. Thanks are also extended to Jin Chan and Carol Tseng for their assistance in various experiments and analysis. A very special thanks to Mahesh Chandramoulli for his expertise and assistance in the TEM analysis and Professor George Johnson who provided the alternative viewpoint of my research.

Enough thanks cannot be given to the people of the Morris Group, past and present who, through their warmth and caring, created a surrounding in which this work progressed with little difficulty and Bill Morris who, through his vision, understanding, and clarity of thought, has provided the environment within which so many, such as I, have found success.

Primary funding for this work was provided through a Rockwell International Fellowship. Additional support was provided by the Director, Office of Energy Research, Office of Basic Energy Science, Material Sciences Division of the U.S. Department of Energy under Contract No. DE-AC03-76SF00098. Thanks are also due to Masahiro Yanagawa of Kobe Steel in Japan for providing the material for this study. Special thanks are also extended to James Wu, John Holtius, Chip Flor, and Peter Reugg who, as part of the technical support staff at Lawrence Berkeley Laboratory, provided their time and expertise during the course of this research.

Lastly, but most importantly, I would like to thank those who through their friendship, encouragement, and presence, provided me with the reasons to continue and perservere during my graduate studies. My family and "The Clan" have been a constant source of support through the years. May the love between all of us never fade.

INTRODUCTION

Motivation

One of the ultimate goals of Materials Science is to develop a procedure that can accurately predict the plastic response of a given material from a finite set of microstructural parameters. Once such a procedure is formulated, the mechanical behavior of a given material can be optimized for specific applications. The realization of this goal, however, is not trivial. Unlike models that relate the flow stress of a material to only the transient microstructural state, the prediction of the material's plastic response requires understanding the manner by which these microstructural features bring the material to its present state and influence the evolution of this state upon further deformation. This task is further complicated by the inherent non-uniformity of plastic deformation. This is particularly true for deformation processes involving dislocation slip which is both discrete and directional. This non-uniformity represents major obstacles to an overall understanding of deformation. The desire to solve the questions involved with these obstacles has prompted numerous research efforts spanning the past sixty years.

Studies in the area of deformation have historically been conducted on four levels that differ in the length-scale at which they describe the microstructure. These can be categorized as the atomistic, substructure, macrostructure, and continuum levels. Much of the difficulty associated with producing a general deformation model arises from the complexities involved in expanding our fundamental understanding of deformation to include all four of these levels. A survey of the literature reveals that the majority of our fundamental understanding resides at the two extreme scales: atomistic and continuum. The former level, which represents the smallest physical scale, includes all relevant properties of those features that provide resistance to dislocation slip; this comprises the bulk of the original dislocation studies, calculations, and theories introduced by such famous names as Orowan[1-6], Polyni[7], Taylor[8,9], Peierls[10], Nabarro[11,12], and Frank[13] that emerged during the middle third of this century. Studies at this level typically involve the calculation of dislocation glide resistance due to the lattice, solutes, precipitates, and other individual dislocations. The majority of atomistic models that have resulted from these studies are very well established and are reviewed extensively within the accumulation of conference proceedings[14-16] and individual texts[17-24]. In a similar fashion, the concepts and mathematics that were first developed within the field of continuum mechanics and then applied to the theory of plasticity are also well established.[25-27]

By themselves, the application of the concepts and models introduced in these two levels to work hardening is somewhat limited. The interaction of a single dislocation and its strain field with other structural features at the atomistic level fails to address the role of the same dislocation within a large aggregation of dislocations. In the same light, continuum models typically omit many of the inherent heterogeneities associated with deformation processes. It is therefore necessary to provide links between atomic scale

interactions, such as dislocation-dislocation interactions and solute-dislocation interactions, and continuum models. This necessarily requires an understanding of how structural features within both the substructure (dislocation arrangements) and macrostructure (grain morphology) influence the subsequent deformation behavior. Unfortunately, the current understanding of dislocation interactions with features at the substructure and macrostructure levels is comparatively limited. Although considerable efforts and successes have been made toward outlining the evolution, development, and arrangement of dislocations in well-annealed metals[28,29], the influence of pre-existing heterogeneities on the evolution and development of the dislocation arrangements remains unclear.

The current task is to improve our basic understanding of the structural features that reside in these two middle levels, and their influence on work hardening. This fundamental knowledge can then be used to span the gap between the atomistic and continuum scales. However, structural features at the substructure and macrostructure scale are typically the result of the synergistic influences of various atomic scale interactions. It is therefore difficult to ascertain from a modeling point of view which set of these structural features are to be considered and how, as a set, these features are to be accounted for. Although the influence of these features on deformation may be relatively well understood on an individual basis, their interactions with each other are not. Because of the complexities associated with this overwhelming task, much of the effort in the area of deformation and work hardening has concentrated on identifying regimes of deformation in which a single structural feature dominates. The most common structural feature chosen for this singular role is the dislocation density, because of its ability to span the different scales of deformation. On one level, the dislocation density represents a collection of individual dislocations and therefore retains an atomistic characteristic. However, it is also a measurable quantity and hence can be used to quantify the amount of overall deformation that has accrued on a macroscopic level.

It is easily debatable that such a single structure parameter model is too simplistic. For any deformation mechanism, there exists a characteristic length below which deformation is observed to be heterogeneous. For deformation by slip, these heterogeneities are typically revealed by the non-uniform distribution and arrangement of the dislocations. Much of this deformation heterogeneity can be attributed to the discrete and directional character of dislocation slip. In general, the dislocation density cannot account for these non-uniformities. However, heterogeneities also exist at the level of the macrostructure. Features such as subgrain and grain morphologies, grain size distribution, and the overall texture increase the degree of deformation heterogeneity. As a result, models which rely solely on the dislocation density as a structural description are typically valid only after a sufficient amount of deformation has accumulated (greater than five to ten percent strain). Beyond this minimum strain, the heterogeneities become better masked by the increasing dislocation density and deformation can again be considered uniform. A study by Chu and Morris[30] corroborates the phenomenon described above. Their findings show that the work hardening rate in aluminum and

aluminum-magnesium alloys can exhibit varying behaviors prior to some lower limit. Although these deviations in the early work hardening behavior are typically limited to small strains, their work has shown them to be significant enough to alter the subsequent mechanical properties.[30] Further work by Chu, Tseng, and Morris[31], and Tseng[32] suggest that these early deviations are due to differences in the initial grain structure.

Tseng[32] has shown that differences in the initial grain structure also produce different work hardening behaviors at large strains. This strongly suggests that there are heterogeneities associated with the initial grain structure that are not limited to small strains and are able to influence the overall deformation behavior. This result is particularly pertinent to structural aluminum alloys. Nearly all aluminum alloys used in structural applications are precipitation hardened. Consequently, the strength of these alloys is predicated on the characteristics of the various precipitate phases within the microstructure which in turn is determined by the aging treatment. The aging treatment is typically fixed in order to maintain the strength level required of these alloys which consequently fixes the subsequent mechanical behavior. These early results are promising as they suggest an alternative means by which improvements in the work hardening behavior and subsequent mechanical properties can be obtained through modifications of the microstructure at the polygranular level prior to the aging treatment. The potential for such an improvement is particularly salient for those materials that typically experience small strains in real engineering applications. Two examples of such applications are discussed below. For these applications, understanding the sources of these early deviations may provide means to tailor a material's mechanical properties. The promise of these improvements provides the motivation for this study.

Applications

Strength and Toughness of Structural Aluminum Alloys

The initial selection of a material for any structural application is most often governed by its combination of strength and fracture toughness. Since the strength and fracture toughness at a given temperature almost invariably exhibit an inverse relation to one another, it becomes necessary to optimize this combination. Unfortunately, our current understanding of the factors that control strength and toughness is limited, thus making the successful optimization process a fortuitous occurrence rather than one resulting from "good fundamental science".

Continuing research on the mechanisms controlling yield and fracture show that the first concern is a change in the primary fracture mode. The most familiar fracture mode change is the ductile-brittle transition, where fracture is observed to change from a microvoid coalescence mechanism at higher temperatures to cleavage upon a drop in temperature below the ductile-brittle transition temperature.[33,34] This transition often leads to dramatic drops in ductility and in many cases results in catastrophic failures.[35] Fracture mode transitions of this type are most common to body-centered cubic materials such as ferritic steels because of the large temperature sensitivity of the Pierels-Nabarro

stress contribution to the yield strength. Face-centered cubic materials such as aluminum, on the other hand, remain ductile due to their ability to accommodate localized stresses through extensive deformation; hence a ductile-brittle transition is not observed.

Upon the preservation of a ductile fracture mode, the mechanisms controlling yield and fracture have been shown to be associated with the work hardening characteristics of the material.[36-39] Although the various theories are based on different limiting criteria, they all lead to models of the general form

$$K_c \propto \varepsilon_f^a \, n^b \sqrt{E\sigma_y} \qquad (1)$$

where K_c is the fracture toughness or critical stress intensity factor above which a crack is no longer stable, E is the elastic modulus, σ_y is the yield strength, ε_f is the strain to failure, n is the strain hardening rate, and a and b are constants with values typically between zero and one. Typically, an increase in the yield stress will lead to an increase in the fracture toughness. However, the strain to failure may decrease significantly which may subsequently lead to a decrease in the fracture toughness.[40] Examples of this interdependency between strength, elongation, work hardening, and fracture toughness can be observed through overlaid plots of the work hardening rate, $d\sigma/d\varepsilon$, and the true stress, σ, versus ε, the true strain. Such plots have been used extensively by Lloyd and coworkers to study the deformation behavior of various aluminum alloys under torsion[41] as well as bulge test conditions[42]. Such overlay plots have also been used to study the macroscopic tensile behavior of aluminum-lithium alloys at cryogenic temperatures.[43-47] In tension, geometric instability occurs when the strain hardening rate equals the true stress ($d\sigma/d\varepsilon = \sigma$).[48] This instability is often found to coincide with failure in structural aluminum alloys.[43-47]

Figure 1 shows a schematic depicting the interdependence between the strain to failure, flow strength, and work hardening rate. In general, increases in the work hardening rate will result in an increase in the strain to failure (Figure 1a). A series of aluminum-copper and aluminum-copper-lithium alloys studied by Glazer, et al.[43-44], Glazer[45], Chu[46], and Chu and Morris[47], exhibit this behavior with decreasing temperatures. In most materials, however, the increase in the work hardening rate at lower test temperatures is accompanied by an increase in the yield strength which increases the subsequent stress level, resulting in a decrease in the strain to failure (Figure 1b). It is apparent that the ability to change the work hardening behavior without drastically influencing the flow stress will lead to an increase in ductility (Figure 1a). Earlier results show that this is indeed possible through changes in the grain structure.[31,32]

The early work hardening behavior becomes particularly important in many of these high-strength, high-toughness aluminum alloys as a result of their inherent low elongations. In general, these low elongations are a result of the higher strength, which shortens the work hardening curve similar to that shown in Figure 1b. It is apparent that with the higher strengths and lower elongations, the early part of the work hardening curve becomes a large percentage of the total deformation. Early deviations in the work

hardening curve can therefore have a pronounced influence on the subsequent mechanical properties. An example of this is provided by a series of studies on the aluminum-copper-lithium alloy 2090 in the peak-aged condition which revealed elongation values as low as 2%.[32,46,49] In this case, tensile specimens remain in the early work hardening stage and do not enter the large strain regime prior to the intervention of failure. The early work hardening behavior hence becomes a predominant influence.

The future generations of high-strength, high-toughness, aluminum alloys for structural applications will require a better understanding of the structural influences on deformation. This is particularly true for those alloys in which elongation will be further sacrificed for greater strength. In this event, the work hardening rate and the role by which the grain structure influences both the overall work hardening behavior as well as the early work hardening rate will have a large bearing on the subsequent fracture toughness (Equation (1)). For these engineering alloys, it is obvious that single parameter work hardening models are inapplicable. A more general constitutive law must therefore be sought to include the influence of other structural features.

Formability of Aluminum Alloys

In recent years, it has become increasingly important to develop automobiles that are safe for the global environment, and yet do not sacrifice passenger safety, comfort, or vehicle performance. Because of the growing impact of automobiles globally, the automotive industry has been forced to actively pursue solutions to the various environmental problems presented by the continuously increasing number of vehicles. A review of these problems and their potential solutions is given by Kurihara[50-52].

The four key environmental issues that relate to the automobile are global warming, air pollution, destruction of the ozone layer, and waste disposal. At least the first three issues can be directly influenced by improved fuel economy. Methods for improving fuel economy can be divided into two main groups: direct and indirect. Direct improvement in fuel economy can be achieved through greater engine or power transfer efficiency as well as reduced air resistance, while indirect improvements are primarily achieved through weight reduction.[50] Although both direct and indirect means of improvement are important, the relative importance of weight-reduction is steadily increasing as the technologies for direct improvements in fuel economy are approaching their limits. As a result of these issues, the automobiles of tomorrow will likely require significant reductions in weight. To accomplish this, the amount of light weight alloys replacing the steel used presently for body parts and other structural components must increase. Leading candidates for such light weight alloys are aluminum-based.[50-53]

In response to this weight reduction issue, the amount of aluminum alloys used in automobiles has doubled over the past twenty years.[51] However, much of this increase is due to the decrease in the amount of steel used, both through improved processing and improved design. Further weight reductions may require more widespread use of aluminum alloys, specifically in outer body panels.[49,50] However, aluminum alloys exhibit poorer formability characteristics compared to steels, creating a major

impediment to their widespread use in automobiles. Although a considerable amount of research has focused on the deformation and formability characteristics of aluminum alloys[41,42,54-57], our general understanding still remains less than that for steels. In order to meet these weight reduction demands, a thorough understanding of the work hardening behavior of aluminum, both at large strains as well as within the early deviations, is necessary.

Although it is not obvious that early deviations will have a large bearing on the forming process, there is reason to believe that they may. Surface inaccuracies result from elastic recovery and are generally initiated by a non-uniform stress distribution during forming.[58] The difference in stress states between any two given regions is primarily due to the different strain paths each region follows during the forming operation. In addition, the work hardening rate is still relatively high at small strains which may lead to large variations in the flow stress.

Objective

The influence of grain structure on the work hardening behavior of aluminum is investigated by means of a series of tensile tests and microscopic analyses. The reasons for returning to pure aluminum are to eliminate the influence of other structural features such as precipitates and solutes that have hindered a clear analysis in earlier studies. In particular, the dislocation substructure is examined by transmission electron microscopy as a function of initial microstructure and degree of deformation. Observations are correlated to the work hardening behavior determined from specimens pulled in tension. The results of this work may provide answers to the many ambiguities that surround our current understanding of the microstructural influences on work hardening and are directly applicable to the development of structurally based constitutive equations in aluminum alloys.

THEORY

Work Hardening Models: Fundamentals

It is well accepted that there are three well-defined stages of deformation in cubic materials. Figure 2 shows a schematic of a typical stress-strain curve for a single crystal depicting the three stages. Stage I, commonly referred to as "easy glide", is a region characterized by slip along a single system and subsequent low work hardening rates. The extent of Stage I work hardening is highly dependent on crystal orientation, metal purity, and temperature, as well as crystal size and shape. Stage I is rarely seen in polygranular materials except for metals that are well annealed and of very high purity. Stage II hardening refers to a linear hardening region in which both the dislocation density and work hardening rate increase rapidly. Stage II is characterized by the pile up of dislocations on the slip system defined during Stage I. In general, Stage II exhibits work hardening rates that are approximately 100 times greater than those measured in Stage I. The extent of Stage II hardening is dependent on the stacking fault energy. When the stacking fault energy is low, dislocation motion along a single slip plane is energetically favorable. In the case of aluminum, however, the stacking fault energy is high, allowing dislocations to cross-slip around dislocation tangles and other obstacles on the original slip plane. Consequently, Stage II hardening is rarely observed for aluminum. During Stage III or "parabolic" hardening, mechanically and thermally activated softening processes such as cross-slip become important. The work hardening rate begins to decline as the balance between hardening and softening shifts. The resulting stress-strain curve during Stage III follows a roughly parabolic path. Although a Stage IV and even a Stage V hardening regime have been observed[59-60], they are absent in tension tests due to the initiation of necking.

Because of the high stacking fault energy, structural aluminum alloys exhibit only Stage III hardening. Unfortunately, serious efforts focused on understanding work hardening in Stage III have only begun within the past two decades. Although a number of theories have been devised to explain both Stage I and Stage II hardening, the expansion of these theories to include Stage III has been met with considerable difficulty. Much of this difficulty has stemmed from the problem of defining the mechanisms of dislocation motion responsible for Stage III work hardening. As a consequence, Stage III work hardening theories remain relatively incomplete.

General Constitutive Law for Plasticity

Much of the work in the area of work hardening has been directed towards the construction of a constitutive law that may accurately predict the plastic response of a material. In general, this consists of a set of equations that describe the state of a material through a number of structure parameters (S_1, S_2, S_3,...). These equations are typically written in differential form as a set of coupled equations consisting of a rate-of-flow equation and a set of structure-change equations:

$$\dot{\varepsilon} = f_0(\sigma, \dot{\sigma}, T; S_1, S_2, S_3, ...) \qquad (2a)$$

$$dS_1 = f_1(\sigma, \dot{\sigma}, T; S_1, S_2, S_3, ...)dt \quad (2b)$$

$$dS_2 = f_2(\sigma, \dot{\sigma}, T; S_1, S_2, S_3, ...)dt \quad (2c)$$

$$dS_3 = f_3(\sigma, \dot{\sigma}, T; S_1, S_2, S_3, ...)dt. \quad (2d)$$

When the strain rate varies monotonically with stress, Equations (2) can be inverted to give:

$$\sigma = \bar{f}_0(\dot{\varepsilon}, T; S_1, S_2, S_3, ...) \quad (3a)$$

$$dS_1 = \bar{f}_1(\dot{\varepsilon}, T; S_1, S_2, S_3, ...)dt \quad (3b)$$

$$dS_2 = \bar{f}_2(\dot{\varepsilon}, T; S_1, S_2, S_3, ...)dt \quad (3c)$$

$$dS_3 = \bar{f}_3(\dot{\varepsilon}, T; S_1, S_2, S_3, ...)dt \quad (3d)$$

This alternative description relates both the external variables, strain rate, $\dot{\varepsilon}$, and temperature, T, and the internal structure parameters to the flow stress, σ, which represents a direct macroscopic measure of the state of the material.

Deformation studies are typically directed toward defining various structural features and describing their individual influence on the state of the material. From this, a set of constitutive equations can be derived. The list of potentially important microstructural features which may play a role in the deformation behavior of a metal, however, is very large. Such features range from the atomic scale, including the nature of dislocation interactions, to more large scale features such as the overall texture. Attempts to describe the role of these parameters on the plastic behavior are complicated by the mutual interaction between two or more microstructural features. From Equations (2) and (3), it can be seen that not only is the flow stress influenced by the structure parameters, but the evolution of the structure parameters themselves are influenced by each other.

Due to the multiplicity of microstructural effects, most of the success in the area of deformation studies have come from efforts that concentrate on reducing Equations (2) and (3) to only include a single structure parameter. The construction of such a model employs the concept of a saturation stress. It is assumed that a structural feature, upon sufficient deformation, will reach a steady state. Once this equilibrium state is reached, the structural feature no longer changes with continued deformation and therefore does not contribute to any further change in the mechanical state of the material. A single structure parameter model is valid if one structural feature has an equilibrium state or saturation stress that is significantly greater than those saturation stresses associated with all other structural features, or conversely, all but one structural feature have equilibrium states or saturation stresses which are essentially insignificant.

One of the benefits of a single structure parameter model is that the saturation stress defines a uniqueness of state. The microstructure of a material containing a single structure parameter will become fixed or "saturated" at the equilibrium state. Equations (3) will then reduce to

$$S_s = f(\dot{\varepsilon}, T). \quad (4)$$

Provided that the equilibrium structure is a monotonic function of both the strain rate and temperature, a unique, saturated state can be defined by the two external variables only. It then follows that the saturation stress itself is also uniquely defined by the strain rate and temperature, resulting in the structure insensitive constitutive equation,

$$\sigma_s = f(\dot{\varepsilon}, T). \quad (5)$$

Numerous experiments have confirmed the uniqueness of this saturation stress for metals under both uniaxial tension[61,62] and compression[61,63].

Work Hardening Models: Single Parameter Models

Kocks-Mecking Model

The most notable single parameter work hardening model currently used to describe Stage III deformation behavior was first presented by Kocks[62] and Mecking[64]. The model was first developed from experiments on pure, well-annealed, polygranular metals. In the model, the dislocation density is the dominating microstructural feature. This choice of structural features necessarily limits the model to large strains, the reasons for which have been discussed previously. Despite its overall simplicity, the semi-empirical model continues to stand as the most widely accepted work hardening model. Since its conception, the model has proved useful in its description of the work hardening behavior in both pure metals and dilute solid solutions. Although numerous efforts have concentrated on modifying this model, the basic structure remains intact.

The basic formulation of the model makes use of the empirically found relation,

$$\tau = \tau_0 + \alpha G b \sqrt{\rho}. \quad (6)$$

where α is a constant on the order of unity, G is the shear modulus, b is the Burger's vector, ρ is the dislocation density, and τ_0 is the friction stress, the resistance of the matrix to dislocation glide. The proportionality between the square root of the dislocation density and stress has been established both experimentally and theoretically.[65-67]

Increases in the dislocation density must be a result of the applied strain. The rate at which the dislocation density increases with strain can be written, in general, as a sum of two components,

$$\frac{d\rho}{d\gamma} = \frac{d\rho}{d\gamma}\Big|_h - \frac{d\rho}{d\gamma}\Big|_s. \quad (7)$$

where the subscripts, h and s, represent those mechanisms which contribute to the hardening and softening, respectively, of the material. The hardening term on the right hand side of Equation (7) represents the rate at which dislocations are stored. This rate can be obtained through a simple model.

Consider a cube containing an edge dislocation subjected to a shear stress τ, as shown in Figure 3. If the dislocation moves a distance Λ, the top half of the cube is displaced by a distance $(\Lambda/L)b$, with respect to the bottom half, where L is the dimension of the cube. The corresponding shear strain is

$$\gamma = \frac{\Lambda b}{L^2}. \tag{8}$$

For N dislocations, Equation (8) becomes

$$\gamma = \frac{N\Lambda b}{L^2}, \tag{9}$$

where Λ now represents the dislocation mean free path. The total length of dislocations is NL. The dislocation density, ρ, is obtained by dividing the total length of dislocations by the volume of the cube, N/L^2. Substituting into Equation (9) gives

$$\gamma = \rho b \Lambda. \tag{10}$$

The dislocation mean free path, Λ, can be assumed to be proportional to the mean dislocation spacing, λ, which in turn is inversely proportional to the square root of the dislocation density,

$$\Lambda = \alpha\lambda = \frac{\alpha}{\sqrt{\rho}}. \tag{11}$$

Combining Equation (10) and (11) gives

$$\gamma = \alpha b\sqrt{\rho} \tag{12}$$

The derivative is then

$$\frac{d\rho}{d\gamma}\Big|_h = k_1\sqrt{\rho} \tag{13}$$

where the burger's vector and the constant of proportionality, α, has been incorporated into the constant k_1.

The softening term in Equation (7) is the rate at which dislocation annihilation occurs. This decrease in the dislocation density is due to dynamic recovery processes that occur among the previously stored dislocations.[68] Consider an area, dA, on a favored slip plane along which a dislocation with a burger's vector, b, sweeps across. The number of dislocations already existing within this area is equal to ρdA. This value represents the number of recovery sites available to the sweeping dislocation. The total change in dislocation length due to recovery within the area, dA, is $L_R\rho dA$ where L_R is the average recovered length per dislocation. The recovered dislocation density is obtained by dividing by the volume δdA,

$$d\rho = \frac{L_R \rho\, dA}{\delta dA} = \frac{L_R \rho}{\delta}, \tag{14}$$

where δ is the spacing between slip planes. The corresponding shear strain associated with the sweeping dislocation is

$$d\gamma = \frac{b}{\delta}. \tag{15}$$

Dividing Equation (14) by Equation (15) gives

$$\frac{d\rho}{d\gamma}\Big|_s = \frac{L_R \rho}{b} = k_2 \rho \tag{16}$$

Substituting Equations (13) and (16) into Equation (7) gives,

$$\frac{d\rho}{d\gamma} = k_1\sqrt{\rho} - k_2\rho. \tag{17}$$

Combining Equation (17) with the derivative of Equation (6) with respect to ρ results in an equation which describes the evolution of the work hardening rate,

$$\theta = \frac{d\tau}{d\gamma} = \frac{d\tau}{d\rho}\frac{d\rho}{d\gamma} = \frac{\alpha G b}{2\sqrt{\rho}}(k_1\sqrt{\rho} - k_2\rho) = \frac{\alpha G b k_1}{2} - \frac{k_2}{2}(\tau - \tau_o). \tag{18}$$

where the shear stress, τ, replaces the dislocation density via Equation (6). This can be further reduced to

$$\theta = \theta_o - K_2\tau \tag{19}$$

where K_2 replaces $k_2/2$, and θ_o is the work hardening rate obtained when the work hardening curve is extrapolated back to a stress value equal to zero. This zero stress work hardening rate is independent of strain rate and depends on temperature only through the temperature dependence of the shear modulus. For a well-annealed polygranular metal consisting of randomly oriented grains, Equation (19) is easily modified for tensile tests by multiplying both the work hardening rate and true stress by appropriate powers of the Taylor factor[69] so as to give

$$\Theta = \frac{d\sigma}{d\varepsilon} = \Theta_o - K_2\sigma. \tag{20}$$

where σ and ε represent the tensile stress and tensile strain, respectively. Details of this derivation are discussed in a later section. Equation (20) is shown schematically in Figure 4. Actual curves taken from tensile tests will exhibit a drop in the work hardening rate from a value equal to the elastic modulus at approximately the yield strength. Deviations under tensile conditions also occur near the necking criterion, when the work hardening rate equals the true stress, due to geometric considerations. Torsion tests have established that the linear decrease in the work hardening rate continues well below the necking criterion prior to exhibiting Stage IV deformation behavior.[59,60]

Kocks[62] has referred to the two terms on the right hand side of Equation (19) as the thermally independent and thermally dependent terms, respectively. The first term, θ_o, is further found to be relatively insensitive to different FCC polycrystalline materials. This constant is measured to be on the order of G/200 for pure FCC polycrystals. A statistical argument is provided for this constancy claiming that a fixed proportionality exists between the average spacing and size of "hard" areas within the initial matrix.[70] The latter, thermally dependent term, is, in essence, a dynamic recovery term which is

controlled by the thermally activated process of cross-slip. Consequently, K_2 will decrease with decreasing temperature and increasing strain rate, resulting in a greater saturation stress.

The Kocks-Mecking model implies that Stage III work hardening occurs when dynamic recovery processes become important. This assumption has come under scrutiny, particularly in light of the smooth transition commonly observed between Stage II and Stage III work hardening behaviors. Kuhlmann-Wilsdorf argues that this smooth transition indicates an absence of a significant change in the dislocation rearrangement.[71,72] However, a shift in the dominant deformation process should lead to a transient discontinuity in the stress-strain curve which is not observed.

A second shortcoming of the Kocks-Mecking model is the lack of a full structural description. This necessarily limits the use of the Kocks-Mecking model to well-annealed, single and polycrystals. As discussed previously, the dislocation density does not account for heterogeneities in the dislocation network. Even within pure materials, heterogeneities in the arrangement of the dislocation density are inherent due to the directionality of slip. Extensive observations and analysis of these heterogeneities can be found in the literature.[56,73-79] It is reasonable to assume that these heterogeneities will be further influenced by other structural features at the macroscopic scale, particularly during the early stages of deformation when the dislocation density is still relatively low.

Kuhlmann-Wilsdorf Model: Mesh-Length Theory

Kuhlmann-Wilsdorf addresses the issue of non-uniform dislocation arrangements by incorporating the formation of dislocation cells, dislocation lattice structures, and other low energy dislocation substructures often observed during straining in what is referred to as the Mesh-Length theory.[71,72,80] These cell structures and lattice structures are typically defined by walls of high dislocation density which surround interiors of low dislocation density. Kuhlmann-Wilsdorf argues that these low energy dislocation substructures are a natural consequence of the need for dislocations to reduce the resolved shear stress component acting on them. To reduce this stress to a level equal or below that of the frictional stress, dislocations rearrange themselves into cellular-like structures. In this manner, the respective resolved shear stresses from neighboring dislocations are mutually screened.[71,81,82] A series of papers by Bassim and Kuhlmann-Wilsdorf confirms this reduction in the resolved shear stresses between screw dislocations in hexagonal structures.[83-87] Computer calculations show that such three-dimensional "checkerboard" arrangements within FCC materials also exhibit particularly low strain energies.[88]

In the Kuhlmann-Wilsdorf model, the shear stress, $\tau_{s.}$, required to move dislocations is assumed to be independent of the frictional stress, τ_o, required to activate the dislocations such that the total shear stress, τ, on the system is

$$\tau = \tau_o + \tau_{s.} \qquad (21)$$

Dislocation motion requires the system to be at a high enough stress level so that free dislocations within the existing dislocation network may bow out. Following the theory of Frank and Read[89], this stress can be written as

$$\tau_s = \frac{\alpha G b}{y} \tag{22}$$

where α is a constant near unity, and y is the free dislocation link length, or mesh-length, between two resisting obstacles. This mesh-length will, in general, be proportionally related to the mean dislocation spacing, Λ, by a proportional factor, m, so that

$$\tau_s = \frac{\alpha G b}{m\Lambda}. \tag{23}$$

Applying the inverse proportionality between the mean dislocation spacing and the square root of the dislocation density in Equation (12) gives

$$\tau_s = \frac{\alpha G b \sqrt{\rho}}{m}, \tag{24}$$

which, with the exception of the constant factor m, resembles Equation (6).

The Kuhlmann-Wilsdorf model introduces two additional parameters, β and g, which provide a statistical description of the dislocation arrangement. The first parameter, β, describes the fraction of mobile dislocations that are stored in the dislocation network. The change in the stored dislocation density, $d\rho$, is then,

$$d\rho = \beta d\rho_m \tag{25}$$

where ρ_m is the density of mobile dislocations. The change in strain is also a function of the mobile dislocation density,

$$d\gamma = d\rho_m b L \tag{26}$$

where L is the mean free path of the mobile dislocations. Combining Equations (25) and (26) results in the dislocation storage rate,

$$\frac{d\rho}{d\gamma} = \frac{\beta}{bL}. \tag{27}$$

Equation (27) differs from Equation (11) in two aspects: the multiplying factor of β and the parameter, L, which differs from the mean dislocation spacing, Λ, used in the Kocks-Mecking construction.[62,64] Whereas the mean dislocation spacing is a statistical average based on all dislocations, the mean free path in Equation (27) does not require a fixed relationship between the distance traveled by a dislocation and the dislocation density. However, it is recognized that the mean free path must be coupled with the dislocation density in some manner. To resolve this, the Kuhlmann-Wilsdorf model introduces the second parameter, g, such that

$$L = g\Lambda \tag{28}$$

where g is a constant on the order of 100 during Stage II deformation.[71,72,75,81]

For materials that form cell structures upon deformation, the mean free path, L, can be replaced with the dislocation cell diameter, D. Dislocation cells are typically observed to extend nearly parallel to the primary slip plane with only short interconnecting links across the primary slip planes.[73,90] Hence, the dislocation cells can be assumed to be roughly circular and stretched out along the glide plane so that the volume of a cell is

$$V = \frac{\pi D^2}{4}\delta, \tag{29}$$

where δ is the thickness of the cell a direction normal to the primary slip plane. Equations (25) through (27) then become

$$d\rho = \beta d\rho_m = \frac{\beta N \pi D}{V} \tag{30}$$

$$d\gamma = \frac{Nb}{\delta} = \frac{Nb\pi D^2}{4V} \tag{31}$$

and

$$\frac{d\rho}{d\gamma} = \frac{4\beta}{bD} \tag{32}$$

respectively. Taking the derivative of Equation (21) and combining with Equations (12), (28), and (32) gives the work hardening rate as

$$\theta = \frac{d\tau_s}{d\gamma} = \frac{\alpha G b}{2m\sqrt{\rho}}\frac{4\beta}{bD} = \frac{2\alpha G}{m\sqrt{\rho}}\frac{\beta}{g\Lambda} = \frac{2\alpha G}{m}\frac{\beta}{g}, \tag{33}$$

where the variation of the friction stress, τ_o, with strain is considered to be negligible. During Stage II hardening, the Mesh-Length theory carries the assumption of "similitude". This is the assumption that upon deformation and the ensuing increase in the dislocation density, all geometric relations remaining constant; the dislocation arrangement simply shrinks in scale. When this assumption of similitude holds, both β and g remain constant, resulting in a constant work hardening rate.[71,72,75,81,91] However, similitude eventually breaks down, causing the ratio, β/g, to decrease, marking the beginning of Stage III work hardening.

There are two hypotheses for the loss of similitude. The first asserts that Stage III hardening begins when the mean free path ceases to decrease further despite the continuing decrease in the mean dislocation spacing. For those materials exhibiting the formation of dislocation cells, this translates to a cessation of dislocation cell shrinkage. The dislocation cell diameter, D, remains constant while the mean dislocation spacing, Λ, continues to decrease, thus causing g to increase and the subsequent work hardening rate, θ, to fall. A second hypothesis offered for explaining the onset of Stage III hardening is the occurrence of cross-slip. At high enough stresses, dislocations are able to overcome obstacles by cross-slipping onto an intersecting slip plane. The dislocation mobility therefore increases, and the fraction of the mobile dislocation density stored in the dislocation network, β, decreases.

A number of models have been proposed based on this assumption of cross-slip. The most notable model was proposed by Seeger and coworkers in which cross-slip is assumed to nucleate as a result of a pileup of screw dislocations against a Lomer-Cottrell lock.[92,93] Some arguments have been raised against such a change in the deformation mechanism. In particular, this change in the dominating dislocation motion mechanism cannot account for the smooth transition from Stage II to Stage III hardening.[71,72] In addition, cross-slip has been observed during Stage II deformation, well before the onset of Stage III deformation. Nonetheless, cross-slip does appear to play some crucial role. By far, the strongest evidence supporting the importance of cross-slip during Stage III work hardening is given by Mecking and coworkers, who were able to normalize the Stage III work hardening behaviors obtained from various face-centered-cubic metals by taking into account their respective differences in stacking fault energies.[94]

It is interesting to note that the Kuhlmann-Wilsdorf model does not strictly require the mechanism of dynamic recovery. This is unlike the Kocks-Mecking model, which is based on the occurrence of dynamic recovery during Stage III work hardening. Instead, the Mesh-Length theory makes use of the parameter β to control the rate at which dislocations are stored. This decrease in the value of β, however, may be due in part to the increased chance for the mutual annihilation of mobile dislocations. This makes the parameter β somewhat similar to the parameter K_2 in the Kocks-Mecking model.

Despite the incorporation of non-uniform dislocation arrangements, the Mesh-Length theory is similar to the Kocks-Mecking model in that it lacks a sufficient structural description. During both Stage II and Stage III work hardening, the primary structural feature is the cell or lattice substructure. Other structural features do not come into play except through the parameters of β and g or through a change in the frictional stress, τ_o, which only shifts the overall stress level at which the deformation process occurs. Changes in β will alter the ease of cross-slip and subsequently the rate at which the cell or lattice substructure forms. Likewise, changes in g will predetermine the initial scale of the dislocation substructure. In both cases, however, the configuration of the substructure remains the same. In other words, the non-uniformity of the dislocation arrangement assumed in the Mesh-Length theory is itself consistent and homogeneous, although on a larger length-scale than that described by Kocks and Mecking. Figure 5 demonstrates this similarity between the two models schematically.

It remains unclear how and to what extent dislocation cells influence the work hardening behavior. The fact that the Kocks-Mecking model and the Kuhlmann-Wilsdorf model follow along similar lines of reasoning, with the exception of the length-scales described, emphasizes this void in our understanding. The Kocks-Mecking model argues that the motion of dislocations is governed by the development of hard regions which initiate along parallel slip planes which eventually impinge along directions normal to the glide plane.[70] As these dislocation tangles grow, the motion of dislocations becomes increasingly difficult regardless of whether these tangles are themselves arranged in a cellular structure or not. The formation of cells is therefore a consequence of the

deformation process and may be considered as having no direct influence on the work hardening behavior. In contrast, the work hardening model presented by Kuhlmann-Wilsdorf states that the formation of dislocation cells or a dislocation lattice provides a limit to the motion of dislocations through the material as well as a structure that the dislocation density must conform to.[71,80]

Early Regime Work Hardening Models

Both the Kocks-Mecking model and the Mesh-Length theory assume that the static arrangement of dislocations is homogeneous. This homogeneity must also extend in a dynamic sense. Specifically, the process by which the dislocation arrangement progresses must not change. At low strains, however, the dislocation density is still relatively small, allowing other structural features to prevail over the natural arrangement process. This may lead to deviations from a simple work hardening model during the early stages of deformation. It is obvious that the derivation of a more general work hardening model will require an expansion of the number of structure parameters employed. However, it remains unclear which of these structural features should be incorporated into a work hardening model. The situation is made even more difficult by the large number of definable structural features, any combination of which may be responsible for deviations in the work hardening behavior.

A reexamination of the concepts leading to Equations (4) and (5) shows that a breakdown in the single structure parameter model at low strains is expected. Let σ_{s1} and σ_{s2} represent the saturation stresses associated with the two dominating structural features such that σ_{s1} is greater than σ_{s2}. For simplicity, let both structural features lead to equations similar in form to Equation (20) but with different values for Θ_o and K_2. The two equations are depicted schematically in Figure 6a. If the work hardening rates associated with the individual structure parameters are assumed to be additive, a bi-linear work hardening plot will result (Figure 6b). Assuming that the additive attribute is common to all work hardening plots, the extension of this analysis to include n structure parameters with continuously decreasing values of the saturation stress, all of which are associated with linear equations similar to Equation (20), would result in a work hardening plot that curves sharply upward at low stresses (Figure 6d). The characteristics illustrated in Figure 6d are typical of most structural aluminum alloys.

Estrin and Mecking have considered an alternative reasoning for the non-linear work hardening behavior at early strains. In their modification of the Kocks-Mecking model, a particle strengthened material that contains a mean particle spacing, λ, is considered.[95] These particles fix the dislocation mean free path. The evolution of the dislocation density must now incorporate the two structure parameters, ρ and λ, so that Equation (17) resembles

$$\frac{d\rho}{d\gamma} = \frac{k_1}{\lambda} - k_2\rho. \qquad (34)$$

By assuming λ to be constant, thus eliminating a $d\lambda/d\gamma$ term, Estrin and Mecking obtain a complex polynomial function for the work hardening rate,

$$\frac{d\tau}{d\gamma} = \frac{d\tau}{d\rho}\frac{d\rho}{d\gamma} = \frac{\alpha G b}{2\sqrt{\rho}}\left(\frac{k_1}{\lambda} - k_2\rho\right) = \frac{\alpha G b k_1}{2\lambda\sqrt{\rho}} - \frac{\alpha G b k_2\sqrt{\rho}}{2}. \quad (35)$$

Substituting Equation (6) for the dislocation density results in

$$\frac{d\tau}{d\gamma} = \frac{\alpha^2 G^2 b^2 k_1}{2\lambda\tau} - \frac{k_2\tau}{2} = \frac{K_1}{\tau} - K_2\tau \quad (36)$$

which bears a marked similarity to the n-parameter curve of Figure 6d.

Ashby argues that any microstructure more complex than a single crystal must be treated as a "plastically non-homogeneous material", due to the existence of grain boundaries which necessarily impose gradients of plastic deformation.[96] With this mind, Ashby proposes a model that avoids the problem of selecting a second distinctly different structural feature by separating the dislocation density into two independent components: "statistically stored" and "geometrically necessary". During the early stages of deformation, "geometrically necessary" dislocations dominate in order to accommodate the deformation gradients between neighboring grains. The slip length associated with the "geometrically necessary" dislocations, λ_g, is characteristic of the microstructure. The most common feature used to describe this slip length is the grain size. Since the grain size is independent of strain, the "geometrically necessary" dislocation density, ρ_g, increases linearly with strain. However, the slip length associated with the "statistically stored" dislocations, λs, decreases with further straining due to the increasing degree of random interactions among an increasing population of dislocations. Consequently, the "statistically stored" dislocations, ρ_s, accumulate more rapidly and eventually, after sufficient straining, dominate the deformation behavior. The strain required for this transfer of dominance increases with decreasing values of λ_g.

Work Hardening Models: Influence of Structure

Theories of dislocation motion, combined with numerous empirical models, provide a guide as to the manner by which changes in testing environment, namely temperature and strain rate, will influence the work hardening behavior. As described earlier, Kocks finds that both a decrease in temperature and an increase in strain rate will decrease the slope exhibited by the work hardening rate versus true stress curve.[62] Although it is much less understood, a similar mapping exists between the work hardening behavior and structural features. In this section, results from earlier investigations are reviewed. The findings suggest that the various structural features, similar to the external parameters, may also be categorized by the manner by which they alter the work hardening rate versus true stress curve.

Expansion from Single Crystals to Polycrystals

In 1938, Taylor expanded the then-present understanding of deformation by dislocation slip in single crystal deformation to a polycrystalline structure containing a collection of randomly oriented grains.[97] His successful model provided an understanding of how slip is possible within a crystal aggregate such that the boundaries

of neighboring grains remain in contact after slipping has taken place. A later complementary theory by Bishop and Hill further formalized the concept of discrete sets of stress states in FCC materials.[97,98]

One of the many concepts that emerged from this pioneering work is the Taylor factor. The Taylor factor results from the assumption that the macroscopic work undergone by a material in creating a unit strain must equal the summation of work done by the individual dislocations that move to accommodate the unit strain. Mathematically, this equality can be written as

$$\sigma d\varepsilon = \Sigma \tau d\gamma, \tag{37}$$

where the summation on the right hand side is over all slip systems that are activated to accommodate the macroscopic strain. Taylor[97] and Bishop and Hill[98,99] have both shown that the minimum number of slip systems required to accommodate any macroscopic strain conditions is five. Assuming that the shear stress to move a dislocation is equal among the different slip systems, Equation (37) can be rewritten as

$$\sigma d\varepsilon = \tau \Sigma d\gamma. \tag{38}$$

The Taylor factor is simply the ratio between the macroscopic properties and the properties of the slip systems;

$$M = \frac{\sigma}{\tau} = \frac{\Sigma d\gamma}{d\varepsilon}. \tag{39}$$

The Taylor factor associated with a given polycrystalline material is obtained by averaging the independent Taylor factors associated with each individual grain. For a material consisting of a completely random set of grain orientations, the Taylor factor is calculated to be approximately 3.06.[97-99]

Applying Equation (39), the work hardening rate of a polygranular material, Θ, becomes

$$\Theta = \frac{d\sigma}{d\varepsilon} = \frac{d(M\tau)}{d\gamma/M} = M^2 \frac{d\tau}{d\gamma} = M^2 \theta, \tag{40}$$

where θ represents the work hardening curve for a single crystal, and the summation is dropped by assuming that the average contribution from each slip system is equal. Further experiments by Kocks on well-annealed polycrystals show that the validity of Equation (40) requires that θ be obtained from single crystals oriented for multiple slip; specifically, the <111> or <100> tensile directions.[69,100] Using Equations (39) and (40), plots of the work hardening rate versus true stress will demonstrate greater slopes with increasing Taylor factors. Figure 7 illustrates this graphically.

Influence of Grain, Subgrain, and Cell Size

One of the inherent shortcomings of Taylor's analysis is the lack of information about grain boundaries. Taylor's model assumes that each grain responds to an applied strain as a single unit, rotating about different axes, and that the character of the grain boundaries separating the individual grains do not influence the deformation

process.[96,101] However, there is considerable evidence that deformation near grain boundaries differs from that within the grain interiors.[102] The various models that have been proposed to explain the influence of grain boundaries have been reviewed by Li and Chou[103], and Thompson[104]. More recently, a review by Lasalmonie and Strudel also contains the extension of these models to creep and fatigue.[105] Some of the concepts emerging from these various models and their effect on the work hardening behavior are described below.

The first attempt to understand the influence of grain boundaries concentrated on the effect of grain size on the yield strength. This pioneering work resulted in what is termed the Hall-Petch relation[106,107],

$$\sigma_y = \sigma_i + k_y d^{-n}, \tag{41}$$

where d is the grain size, n is a constant on the order of 0.5, σ_i is the friction stress, and k_y is a constant which is associated with the ease of slip propagation across grain boundaries. Petch and coworkers have accumulated data from a number of different steels that are well described by Equation (41).[107-115] Additional data obtained from tests on copper[116], silver[117], aluminum[118], nickel[119,120], tungsten[121], niobium[122], chromium[123], and other metals[115,124-128] are also found to obey Equation (41). The Hall-Petch relation is founded on the concept that grain boundaries act as obstacles to slip transmission from grain to grain. As a result, dislocations must pile-up at the grain boundaries, the maximum length of the pile-up being fixed by the grain size.[107,108] Comprehensive reviews of the mathematics involved in deriving Equation (41) based on this pile-up concept is given by Weertman and Weertman[20], and Li and Chou[103]. It should be noted that for materials that have been cold-worked and recovered, the size parameter in Equation (41) is often found to be comparably represented by the subgrain size, although the values of the parameters σ_i and k_y are different.[129-135]

A second rationale for explaining the validity of Equation (41) is the inverse proportionality between the grain size and the volume fraction of grain boundaries. If one assumes that the grain boundaries are all of the same character and comprise of misfit dislocations, then the volume fraction of grain boundaries is proportional to the dislocation density.[136,137] Replacing the grain size, d, in Equation (41) with $1/\rho$ results in Equation (6), where k_y is equivalent to $\alpha G b$. This alternative reasoning is particularly attractive since it suggests that Equation (41) can be expanded to describe the flow stress during deformation. Equation (41) then becomes,

$$\sigma = \sigma_i(\varepsilon) + \frac{k_y(\varepsilon)}{\sqrt{d}} \tag{42}$$

where the left hand side is the flow stress and the friction stress as well as the Hall-Petch slope may be functions of strain. Armstrong, et al., find Equation (42) to be descriptive for mild steel (BCC), zinc (HCP), and 70/30 brass (FCC).[115] Their results indicate that the Hall-Petch slope, k_y, for these materials remains relatively constant up to strains of 20%. This is unlike the friction stress which increases with strain. Comparable work on aluminum[138-140], copper[141], iron and steels[108,142-144], and other metals[137,145], have also

shown good fits with Equation (42). These results indicate that a decrease in the grain size only alters the overall stress level at which deformation occurs; the overall deformation mechanism remains unchanged. This effect reveals itself in a work hardening versus true stress plot as a simple shift to higher stresses, the slope of the work hardening curve remaining constant (Figure 8). Note that the larger grain size microstructures also provide for greater elongations since the shift of the work hardening curve to lower stresses allows the work hardening rate to decrease to lower values prior to reaching the necking criterion.

Despite the initial success of Equation (42) in describing the flow stress, there is overwhelming evidence that Equation (42) is not general to all materials. The strongest evidence is presented by Thompson and Baskes who find that the stress-strain curves for both polycrystalline copper and aluminum of different grain sizes cross thus invalidating Equation (42) which requires a monotonic increase in the stress-strain mapping with decreasing grain size.[146] Plots of the Hall-Petch type (σ versus $1/\sqrt{d}$) show that k_y is not a constant but varies from negative values to positive values with decreasing grain size, the variation increasing at higher strains. Ashby first offered an explanation for the observed deviations from linearity, asserting that the local hardening behavior near the grain boundaries must differ from that within the grain interior.[96] Following Ashby's idea, two classes of theories have arisen to explain the influence of grain boundaries.[103,147-149] The first asserts that the grain boundaries act as dislocation sources[103,147], while the second assumes that the hardening behavior near the grain boundaries differs from that within the interior[148,149]. In both cases, the mechanism at or near the grain boundaries dominates the deformation process at low strains. The increase in the dislocation density at higher strains increases the density of dislocation interactions within the grain, which eclipses those mechanisms at or near the grain boundaries.

Following the analysis of Ashby[96], Thompson, Baskes, and Flanagan develop a mathematical theory which considers the change in the slip distance of both the "geometrically necessary" and "statistically stored" dislocations.[148] Whereas Ashby assumes that the two types of dislocations are physically indistinguishable, Thompson, et al., contend that each type will dominate in certain regions of the microstructure. Following Equation (6), an appropriate description of the flow stress should therefore have the form,

$$\sigma = \sigma_0 + V_s k_s \sqrt{\rho_s} + V_g k_g \sqrt{\rho_g} \qquad (43)$$

where V_g and V_s are the volume fractions of regions dominated by the "geometrically necessary" and "statistically stored" dislocations respectively, and both k_g and k_s are constants. Since the slip distance associated with the "geometrically necessary" dislocations is fixed by the microstructure, in particular, the grain size, d, ρ_g is proportional to 1/d. On the other hand, the "statistically stored" dislocations are randomly distributed and must follow Equation (12). The area, V_g, is assumed to encompass a volume that extends from the grain boundary by some grain boundary width, δ. Assuming that the grains are spherical, the volume fraction of the

"geometrically necessary" dislocations is δ/d. The grain boundary width, δ, can be replaced with the slip distance, λ_s, since if the grain boundary width was larger, the smaller slip distance would allow "statistically stored" dislocations to reside within the grain boundaries. The resulting equation is

$$\sigma = \sigma_0 + \frac{\lambda_s}{d}\frac{K_g}{\sqrt{d}} + (1 - \frac{\lambda_s}{d})\frac{K_s}{\lambda_s} \qquad (44)$$

where the new constants, K_g and K_s, incorporate k_g and k_s as well as their respective multiplying factors. By fitting Equation (44) to experimental data, a hyperbolic-like relationship between the slip distance, λ_s, and strain is determined.[148] Through an extrapolation of the computer generated data of Thompson, Baskes, and Flanagan, a graphical representation of the grain size effect can be obtained for aluminum. Figure 9, which illustrates this effect, differs slightly from that represented in Figure 8 in two principal ways: (1) the work hardening curve appears to reach a minimum at approximately 5 to 6 μm and (2) below this grain size, the slope of the work hardening curve increases. This latter effect causes the stress-strain curve to level off more rapidly after an initially steep rise at lower strains, thus causing the crossing of curves.

Ashby's contradiction to a simple Hall-Petch relation suggests that the appropriate size parameter to describe the deformation of metals is not a fixed value, such as the grain size, but in fact, must change during the course of deformation. In particular, the distance through which a dislocation is allowed to slip must change with strain. One possible explanation for this is that the deformation process is governed by the dislocation cell size rather than the grain size. Embury, Keh, and Fisher suggest that the flow stress would be better described by a modified Hall-Petch relation in which the size parameter, d, in Equation (42) is representative of the cell size rather than the grain size.[150] Since dislocation cell walls become substantial obstacles after sufficient strain, the mean free path of the mobile dislocations becomes a strong function of the cell diameter. Fujita and Tabata come to the same conclusion for aluminum.[151] A review of additional supporting data by Staker and Holt for copper, aluminum and iron indicates that the exponent n in Equation (41) is equal to 1 for substructure calculations.[66] The success of the Mesh-Length theory proposed by Kuhlmann-Wilsdorf also lends credence to this idea.[71,72,80]

The various findings discussed above appear to provide a relatively thorough understanding of the influence of grain structures as well as substructures on the flow stress. Young and Sherby suggest that the various grain and substructure features can be separated into respective regions of dominance.[152] The influence of cell boundaries will dominate the deformation behavior when the cell size is below a certain value, approximately 0.4 μm. This upper limit, however, is dependent on the grain or subgrain size, increasing to higher cell sizes with increasing grain or subgrain sizes. Since the cell size characteristically decreases with straining, one would expect the dominating structural feature to change from the grain size or grain boundary to the cell size or cell boundary with increasing strain. For example, at a grain or subgrain size of approximately 40μm, the limiting cell size is about 1 μm. Hansen further stipulates that

although not dominant, the grain size will strongly affect the manner by which the cell size dominates hardening due to the strain accommodation processes involved during deformation.[153] This is particularly relevant for very small grain sizes which may suppress the formation of cells altogether.[154]

Recent work in the area of grain size effects has concentrated on determining how the distribution of grain sizes influences the reliability of Equation (42).[155-157] A log normal distribution of grain sizes is observed in both aluminum[158,159] and titanium[160,161] samples undergoing a cold-work and annealing process. This non-uniformity in the grain size distribution results in a deviation from the Hall-Petch equation. Although this deviation is relatively small, it is believed to be responsible for the scatter in the various Hall-Petch type analyses found in the literature.[156] A better agreement with the Hall-Petch equation is obtained when the amount of cold work prior to annealing is increased. This reduces the recrystallization temperature as well as the subsequent grain size distribution.[158,161]

Influence of Dislocation Substructure

The majority of investigations in the area of deformation and work hardening have concentrated on the development of the dislocation substructure and macrostructure, including texture, within an initially well-annealed metal. However, processes involving large deformations, such as sheet forming, typically entail complex loading conditions. This has led to substantial efforts by the automotive industry to understand the influence of basic forming operations on the mechanical properties of steel sheet products. During metal forming operations, the sheet material is subjected to complex strains. In addition, sequential stamping operations are often used. In general, the mechanical conditions responsible for plastic instability under such complex loading schemes are well simulated.[162] However, the means by which structural features lead to these instabilities are only partly understood. In order to gain more insight into this problem, numerous experiments involving changes in strain path have been conducted.

There is substantial evidence indicating that the deformation structure plays a significant role in tests involving a change in loading conditions. Both the ensuing strength and work hardening properties are found to be severely influenced. Wagoner and Laukonis have shown that early transients in work hardening are a result in changes in the strain path rather than changes in the loading.[163] The evolution of the ensuing substructure is also strongly dependent on the amplitude and direction of the change in strain path.[164-168] The observed behaviors can be separated into two categories as described by Doucet and coworkers: positive and negative transients (Figure 10).[169-171] Positive transients are marked by a high subsequent yield stress upon reloading followed by a reduced work hardening rate. This type of behavior is typically observed in tests involving an orthogonal change in the strain path.[165,166,172-178] In aluminum, the prestraining can lead to an increase in the strength level above that obtained by normal uniaxial tension, which results in early failure in aluminum.[172] By comparison, a negative transient is typified by a lowering of the subsequent yield stress upon reloading,

followed by an increase in the initial work hardening rate. This behavior is observed in tests involving a stress reversal or a Bauschinger sequence.[178-184]

Substantial efforts have been made to link the observed macroscopic behavior with the evolution of the deformed substructure. The accumulated experimental results indicate that the cellular structure provides at least a guideline for the observed macroscopic behavior.[185-194] Work on single crystal <111> aluminum by Hasegawa and coworkers suggest that the negative transient observed in stress reversal tests is a result of the dissolution of the cell structure developed during the initial prestraining.[186-189,192] The cellular substructure is polarized in the direction of the initial strain path such that dislocations of like sign accumulate along the same side of a cell wall. Dislocations on the opposing side are of the opposite sign. Upon a stress reversal the outermost dislocations enter a relatively dislocation free cell interior. The mutual annihilation of dislocations of opposite signs entering the cell interior from diametrically opposed sides results in an initial reduction in the dislocation density and a subsequent drop in the yield stress. This polarization and dissolution of the dislocation cells have also been observed in other materials.[190,191,193,194]

The polarization of cells indicates that there is an inherent directionality associated with the formation of the cellular structure. Fernandes and coworkers have shown experimentally that the cell walls form initially on active slip planes and are then stabilized by walls forming on secondary systems[191,194], corroborating earlier observations on cellular structures[73,90]. Microbands immediately form on previously latent systems, upon a reloading in an orthogonal direction. The difficulty associated with the new microbands crossing the preexisting dislocation substructure results in a rise in the yield strength.[175,176] The subsequent transient is concomitant with the rearrangement of the dislocation substructure. The majority of dislocations generated during the initial prestraining disappear due to interactions with mobile dislocations on the new active slip systems.[193] A review of experimental results by Rauch indicates that the resultant strength level in the new direction, as well as the transient, increases with greater prestrains, suggesting that stronger pre-existing dislocation substructures are unable to completely dissolve.[195]

Despite the apparent link between the hardening behavior and the dislocation substructure, it is still unclear whether the evolution of the cellular structure, both prior to and following a change in the strain path, influences the work hardening behavior or is simply an artifact of the macroscopic process. Vincent[196], and later Johnson and coworkers[197,198], investigated the influence of a preexisting cellular dislocation substructure in low carbon steels under monotonic loading conditions. By varying the temperature at which specimens were prestrained, the work hardening behavior as a function of the existence of dislocation cells was examined. Dislocation cells were first formed through prestrainings of up to 20% at room temperature. Specimens were then tested at a lower test temperature at which the formation of dislocation cells is suppressed. Comparison of the subsequent stress-strain curve with that obtained from an uninterrupted test at the same lower temperature revealed no change in the work

hardening behavior although the observed strain shift indicates that the existence of cells produces a shift in the work hardening curve to slightly higher stresses. This lack of influence is a consequence of the sluggish motion of screw dislocation within the cell interiors that dominate the deformation behavior despite the formation of dislocation cells.[198]

The insensitivity of the work hardening behavior to the cellular structure may not be so surprising when considering the analysis of Young and Sherby.[152] TEM micrographs from Johnson's work indicate a cell size measuring approximately 1.5 to 2.0 μm which may still be too large for the cellular structure to be dominant. Johnson, however, argues that the lack of influence is an indication that the formation of cells and the flow stress are not mutually dependent; the cell walls do not necessarily affect the flow stress.[198] The model presented by Mughrabi, which reveals that long range stresses are inevitable in cell structures and that these long range stresses are intimately related to the deformation process, provides at least a possibility that the cell walls are indeed ineffective.[199]

It should be noted that the discussion above has been isolated to pure metals. There are obviously numerous other structural artifacts, such as solutes, dispersoids, and precipitates, which will influence the work hardening behavior. An analysis of these effects, however, is beyond the scope of this work.

Summary

The various theories and concepts presented above highlight much of the current understanding of work hardening. Various models such as those presented by Kocks-Mecking and Kuhlmann-Wilsdorf and coworkers provide a basis from which a general understanding of work hardening can be pursued. Despite extensive efforts concentrated on a number of different aspects of this goal, the question still remains as to the influence of the structural features at both the dislocation substructure and the grain structure scales. If indeed the source of work hardening is isolated to the atomistic scale, then the grain structure may indeed have little influence. However, the results reviewed above indicate that this is not necessarily true. Earlier experiments indicate that the grain structure influences the work hardening behavior at both large and small strains.[30-32,46,47,49] The early deviations have a particularly significant influence on the subsequent mechanical properties of aluminum alloys typically exhibiting low ductility.[30-32]

The current work attempts to isolate structural features at the grain structure level and their influences on the work hardening behavior. The experiments and results presented in this treatise should provide evidence that may assist in expanding our current understanding of the work hardening behavior in aluminum alloys as well as to all materials in general.

EXPERIMENTAL PROCEDURE

Materials and Microstructure

The primary material used in this investigation was high purity aluminum received by Lawrence Berkeley Laboratory in the form of flat tensile specimens machined from 3 mm thick sheets such that the tensile axis is parallel to the rolling direction. Dimensions of the tensile specimens are shown in Figure 11. The purity level was determined by mass spectroscopy to be no greater than 99.94%. Initial processing of the aluminum was done at Kobe Steel, Ltd (KSL) in Japan. The aluminum was melted, cast into ingot form in air atmosphere, and then annealed at 480°C for 24 hours. Ingots were then hot-rolled at 480°C to a thickness of 5mm followed by a cold-rolling to a final thickness of 3 mm (40% reduction).

An additional sequence of tests were done in order to investigate some of the more outstanding issues uncovered by the examination of KSL specimens. Two batches of tensile specimens, referred to as LBL1 and LBL2, were processed at Lawrence Berkeley Laboratory from cast ingots received from Alcoa. Starting ingots were machined from the cast ingot, annealed and hot-rolled to a thickness of 9.5 mm (0.375 in.) at 450°C. The purity level for the two ingots was determined by mass spectroscopy to be no greater than 99.96%. The resulting sheets were scaled and cold-rolled 50% and 60% respectively. Tensile specimens were machined in one of three orientations, parallel, perpendicular, or 45° to the rolling direction. Specimen dimensions are identical to those obtained from KSL (Figure 11).

All specimens were polished to a 15 μm grit size prior to any annealing and subsequent testing to minimize any macroscopic surface effect. Selected samples were polished further to a 0.05 μm grit size to facilitate the observation of slip relief patterns on the surface during testing. Because of the limited number of specimens procured from each LBL batch, all detailed microstructural analysis in this work was conducted on tensile specimens received from KSL. Larger rolling facilities available at Kobe Steel provided larger sheet sections from which multiple specimens were obtained. The larger sheet sections also provided better microstructural consistency from specimen to specimen. Results obtained from LBL1 and LBL2 tensile specimens were limited to tensile test data only.

KSL specimens were processed to provide a wide range of different grain structures. The four primary microstructures, as-received or unrecrystallized (URX), recovered (REC), partially recrystallized (PRX), and recrystallized (REX), were obtained by annealing tensile specimens at different temperatures for three hours followed by a furnace cool. Annealing temperatures for each condition are listed in Table I. A second recrystallization treatment was performed to produce a larger grain size. The annealing temperature for this microstructure is also shown in Table I. The macroscopic grain structure of KSL specimens for each condition was examined by optical microscopy. Optical samples were polished to 0.05 μm and etched using a 5% sodium hydroxide solution for 30 seconds followed by Keller's reagent (2.5% HNO_3, 1.5% HCl, 0.5% HF

(40%), balance H_2O) for two to four minutes. Etched samples were examined on a Nikon Epiphot-TME. Grain and subgrain sizes for the various microstructures were determined by the Heyn lineal intercept method.[200] Additional heat treatments were done to produce other microstructures to investigate trends indicated by these four microstructures.

Testing

All tensile testing was conducted at 77K (liquid nitrogen). This test temperature was chosen primarily to isolate the deformation mechanism of slip. Additionally, the lower test temperature avoided the higher strain rate sensitivity at room temperature which caused necking immediately after yielding in the unrecrystallized microstructure. The subsequent low elongations did not provide a sufficient deformation range for comparison with the other microstructures.

All tensile tests were conducted in a servo-hydraulic testing machine equipped for cryogenic testing under displacement control. Displacement rates for each specimen were chosen to correspond to an engineering strain rate of approximately 10^{-4} per second within the plastic regime. Specimen elongation was monitored by a clip gauge inserted between pins screwed into the tensile specimen at the top and bottom of the gauge length. The pins were spring-loaded to prevent slippage due to the reduction in cross-sectional area during tensile deformation. The engineering strain rate was found to increase with increasing strain due to the deformation and work hardening of material outside the gage length. This phenomenon, however, is counteracted by the increase in the instantaneous gage length. The subsequent variations in the true strain rate were found to be less than five percent. At the relatively low strain rate of 10^{-4} per second, this variation is negligible.

Engineering stress and strain data was collected via computer. The data were then converted to true stress and true strain values by assuming volume conservation during uniform elongation. The resulting true stress-true strain curve was approximated by a spline fit, from which the instantaneous work hardening rate, $d\sigma/d\varepsilon$, was calculated. Work hardening curves are presented as a function of true stress so as to be comparable to data found in the literature.[30-32,62,64,67,94,180,189,192,193,201-203] This type of plot is often used in order to eliminate strain, which is not a thermodynamic variable and cannot be used to describe the state of a given material, from the analysis. Such plots facilitate the separation and identification of various effects, both external and internal, on the structural development of work hardening for tensile specimens under various testing conditions.[45] The resolution of the strain measurements was 0.0002% strain and the precision exhibited was 0.006% strain. Likewise, the resolution and precision of the load measurements were 0.075 and 0.3 pounds respectively. An error analysis based on these precisions revealed an average uncertainty in the calculated values of the work hardening rate of approximately 1.5%, seldom exceeding 3% for the entire plastic range.

Transmission Electron Microscopy

Transmission electron microscopy (TEM) was conducted on KSL tensile specimens both prior to and after straining in order to investigate the influence of the initial grain structure on the evolution and development of the dislocation substructure. TEM samples were prepared parallel to the rolling plane by mechanically grinding to 0.13 mm (0.005 in.) and punching 3 mm discs. The discs were electropolished at 18-20 volts using a double jet polishing technique at -30°C in a 4:1 mixture of methanol and nitric acid. All observations were conducted on a Philips 400 transmission electron microscope at an accelerating voltage of 100 kV. Dislocation substructures were examined by tilting samples to either the [001] or $[0\bar{1}1]$ zone axis closest to the rolling plane normal. The $[0\bar{1}1]$ zone axis was preferred since it is the only zone axis that provides two sets of (111) planes. However, for microstructures exhibiting a strong cube texture, the [001] zone axis was opted for to avoid high tilt angles.

EXPERIMENTAL RESULTS

KSL Specimens

Initial Microstructure

Optical micrographs of the four primary microstructures analyzed in this study are shown in Figure 12. The elongated character of the unrecrystallized, recovered, and partially recrystallized structures are typical of rolled aluminum. The grain size of the recrystallized microstructure was measured to be 110 μm while the grain size of the recrystallized grains within the recrystallized regions of the partially recrystallized microstructure was measured to be about 30 to 40 μm. The grain size of the second recrystallized microstructure (not shown in Figure 12) was measured to be 185 μm. The observed homogeneity of features at the optical scale indicates a small deformation gradient through the thickness of the original sheet material as well as a homogeneous heat treatment. This homogeneity is best demonstrated by the partially recrystallized microstructure which exhibits a relatively random distribution of recrystallized regions.

Tensile Properties

Engineering stress and strain properties obtained from the various microstructures tested in tension are listed in Table II. The decrease in strength with increasing annealing temperature is typical of pure metals. Higher temperatures increase the thermal activation of both vacancies and dislocations, the latter contributing to a greater incidence of mutual annihilations between dislocation segments of opposite signs. The subsequent decrease in the dislocation density results in a decrease in the yield strength. A Hall-Petch type analysis on the two recrystallized samples (Equation (41)) indicates a Hall-Petch slope of 0.05 MPa$\sqrt{m}$ which is consistent with other values reported by Hansen[138], and Thompson, et al.[148] (0.02–0.07). A comparison plot of the stress-strain curves for the two different grain sizes reveals a slightly increasing deviation between the flow stresses with increasing strain, indicating that the Hall-Petch slope is an increasing function of strain (Figure 13a). This is in contrast to the findings of a constant Hall-Petch slope reported by Hansen[138], and Al-Haidary, et al.[139,140]. Figure 13b, however, shows that the increasing Hall-Petch slope does not change the slope of the work hardening curve but instead shifts the curve along the stress axis. This trend is identical to the schematic illustrated in Figure 8 suggesting that the grain size alters only the "background" or "back" stress but does not change the evolution of the dislocation structure. The decrease in grain and subgrain size with decreasing annealing temperatures may account for some of the increase in strength within the recovered and unrecrystallized specimens although the difference in the characteristics of the grain boundary structures between the recovered and recrystallized specimens make a Hall-Petch type analysis between the two structures unreliable.

One of the more interesting results is the occurrence of a peak in the elongation data. Increases in the elongation are typically observed for greater annealing temperatures and subsequent lower strengths. However, Table II shows that the

elongation peaks for the recovered microstructure and then decreases slowly with greater annealing temperatures. Then greater annealing treatments also produces a drop in the strength level to below 20 MPa. The slow decreasing trend in the elongation observed from the recovered to the recrystallized microstructure suggests that the grain structure associated with the recovered microstructure is more amenable to extensive deformation than a recrystallized structure. Measurements of the total elongation emphasize this peak in ductility, further corroborating the ease of extensive strain in the recovered microstructure. It has been hypothesized that this improved ductility may be due to the reduction in grain boundary misorientations.[30,31] The recrystallization process produces higher grain boundary misorientations which increase the difficulty of slip transmission from grain to grain.

Tensile Behavior

Examination of the failed samples reveals substantial necking prior to final failure. The large differences between the total and uniform elongation values attest to this. Cross-sectional areas at the final failure site of all specimens were less than 25% of the initial cross-sectional area and show failure by simple shear. Anisotropy is observed in the necked region due primarily to the geometry of the cross-section. The degree of this anisotropy tended to increase with lower annealing temperatures. This is most likely due to the retention of the rolled characteristics at the lower annealing temperatures. These characteristics were consistent for both KSL and LBL specimens.

Figure 14 shows the plots of the work hardening rates as a function of true stress for the four different microstructures tested at 77K. Note that only the recrystallized microstructure exhibits a single line work hardening curve. The other three microstructures exhibit increasing degrees of deviation during the early stages of deformation with lower annealing temperatures. The unrecrystallized microstructure, which received no annealing treatment, exhibits the strongest bi-linear characteristic. The early deviation in the unrecrystallized microstructure occurs only within the first 6% strain. The latter regime, therefore comprises the bulk of the deformation process. The initial dip observed for the recovered and partially recrystallized microstructures is a result of either impurity segregation to dislocations or the existence of dislocation tangles which remain intact during the annealing treatment. Because of the low impurity levels, the latter is more probable. The fact that the recrystallized sample exhibits only a small dip also supports this reasoning. The peak in the elongation data for the recovered microstructure is matched by a minimum in the work hardening rate extrapolated to zero stress. The zero stress work hardening rate decreases from approximately 1600 MPa for the recrystallized microstructure to a minimum of 900 MPa for the recovered microstructure. For the unrecrystallized microstructure, the zero stress work hardening increases to just above 1000 MPa.

Extrapolation of the linear regimes of the various work hardening curves provides the work hardening parameters as described by the Kocks-Mecking model in Equation (20).[62,64] Table III lists these parameters for the four KSL microstructures tested. The

slope associated with the latter regime can be seen to increase over two-fold from the recovered microstructure to the recrystallized microstructure. Table III also indicates that the slope of the early regime for all three annealed microstructures is roughly the same value. This suggests that for these three microstructures, the early regime is a short transient resulting from a hysterisis effect and not a microstructural effect.

Note that the initial work hardening rate associated with the latter deformation regime varies with the microstructure. The initial work hardening rate of 1720 MPa obtained for the recrystallized microstructure gives a ratio of 0.064 when divided by the shear modulus for pure aluminum (approximately 27000 MPa). This is consistent with the value of 0.06 determined empirically by Kocks for well-annealed pure FCC polycrystals.[62] However, similar calculations for the partially recrystallized, and both recovered and unrecrystallized samples exhibit increasing deviations from Kocks' value, 0.056 and 0.041 respectively. The lower values may be an indication of a texture effect. To check the possibility of a texture effect, Kocks' data is assumed to be obtained from a polygranular sample containing a completely random set of grain orientations ($M \cong 3.06$). Assuming that the deviations from the empirical value 0.06 are due to texture only, corrective Taylor factors for the microstructures used in this work can be calculated from Equation (40). Table IV shows the results of these calculations. The minimum value of 2.53 measured for the Taylor factor is within the range of values for deformation in FCC materials calculated by Chin.[204] Consequently, the change in slope of the latter regime may be attributed to the difference in texture. However, further results to be discussed later, indicate that texture plays a much lesser role.

An interesting point in the data is the overlap of the work hardening plots obtained from the unrecrystallized and recovered microstructures (Figure 14). This overlap can also be seen in Table III where the slope and saturation stress for the latter regime of both unrecrystallized and recovered microstructures are nearly identical. At stresses above approximately 200 MPa, both specimens follow similar deformation paths. Subsequently, both unrecrystallized and recovered samples achieve the same strength level. Differences in the mechanical properties between the two microstructures are therefore due to the work hardening behaviors of the two microstructures during the early stages of deformation. Corresponding stress-strain curves (Figure 15) indicate that the reduction of the first linear regime associated with the unrecrystallized microstructure results in an improved elongation as tabulated in Table II.

Another point of interest is the stress-strain behavior of the partially recrystallized microstructure (Figure (15)). At low strains, the partially recrystallized microstructure parallels that of the recrystallized. Beyond approximately 15 percent strain, however, the stress-strain curve of the partially recrystallized microstructure deviates from that of the recrystallized and begins to parallel the stress-strain curve of the recovered microstructure. This suggests that at low strains, the work hardening behavior of the partially recrystallized microstructure is dominated by mechanisms associated with the recrystallized region whereas at high strains, the dominant mechanism resides within the recovered regions.

The results discussed above establish the bi-linear character of the work hardening behavior in aluminum. For the unrecrystallized specimen, the change in slope that marks the shift from one deformation regime to another occurs at approximately 190 MPa. This stress value corresponds to a true strain of 6.5%. Comparison of this value to the measured uniform and total elongations of 26.4% and 46% for the unrecrystallized microstructure indicates that the early deformation regime constitutes a substantial fraction of the deformation process. The extent of the early regime decreases with increasing annealing temperature; the recrystallized specimen exhibits essentially no early deviation in work hardening. The latter or fully plastic regime that follows the change in slope exhibits a flatter profile than the early regime. The actual slope associated with the fully plastic regime increases with increasing annealing temperature. A schematic summarizing these general observations is shown in Figure 16. Results of a TEM investigation on the two deformation regimes are shown below.

Deformed Microstructure - Latter or Fully Plastic Regime

Figure 17 shows the recrystallized microstructure (110 μm grain size) prior to deformation. Diffraction pattern analysis indicates that the misorientations of the grains are greater than 10°. Upon deformation, a relatively well defined cell structure forms as shown in Figure 18. Figure 19 shows that the cell structure tends to be elongated in the direction of greatest shear, 45° from the loading direction. Actual measured angles varied between 30° and 60° from specimen to specimen. Schmitt has also observed a similar variation about 45° in the angle between the loading direction and primary direction of dislocation cells in copper. Figure 20 shows that the cell boundaries are perpendicular to both the [111] and [200] directions. The aspect ratio of the dislocation cells also varied from grain to grain. Figure 21 shows an extreme case in which the dislocation cells exhibit a symmetrical square configuration. This is most likely due to the chance orientation of the particular grains such that two major slip systems are activated simultaneously. Note also the sharpness of the grain boundary in Figure 21, suggesting that the grain boundary has little influence on the deformation process and the evolution of the dislocation cell structure.

Figures 22 and 23 show the recovered microstructure prior to deformation at two different magnifications. Unlike the recrystallized microstructure, the recovered microstructure contains a well-developed subgrain morphology. The average subgrain size was measured to be 2.2 μm. Diffraction analysis reveals that the misorientation between adjacent subgrains is on the order of a few degrees (Figure 24). Some evidence of a residual dislocation substructure, as shown in Figures 25 and 26, indicates a slightly less than fully recovered microstructure. Figure 27 shows the recovered microstructure after straining into the fully plastic regime. Unlike the cellular dislocation structure found in the recrystallized microstructure, the dislocation arrangement within the recovered microstructure upon a large deformation is observed to be much more random. Although there appears to be a tendency for dislocations to accumulate at the subgrain boundaries, as highlighted in Figures 28 and 29, there are some regions in which the dislocation density is relatively homogeneous. Figures 30 and 31 show the same two

features within the unrecrystallized microstructure after deformation to the same stress level.

Results from a slip relief study on a pre-polished partially recrystallized specimen are shown in Figure 32. Although slip is observed to occur in both the recrystallized and recovered regions, the unrecrystallized region exhibits a greater degree of roughening. This roughening increases in intensity with further straining. Earlier work has shown this out-of-plane rotation to be associated with both lower test temperature in the aluminum-copper-lithium alloys 2090.[32,205] This result led to the hypothesis that the out-of-plane rotation was an additional deformation mechanism. The current results obtained from pure aluminum indicate that in addition to the lower test temperature, an appropriate microstructure must also be present in order for out-of-plane rotation to be observed.

Deformed Microstructure - Early Regime

Figure 33 shows the unrecrystallized microstructure prior to deformation. The initial microstructure exhibits a mixture of subgrain boundaries and a pre-existing dislocation substructure typical of cold-rolling. The dislocation substructure, in general, consists of dislocation bands running roughly parallel to one another. Bay, Hansen and coworkers have conducted extensive microscopy studies on the microstructure of pure aluminum after rolling.[56,75,76,79] Their description consists of a structural hierarchy in which individual dislocation cells are grouped into cell blocks. These cell blocks are themselves separated by dense dislocation walls and microbands. A comparison of the microstructure observed by Bay, Hansen, and coworkers, with the unrecrystallized microstructure in this work shows general similarities. The one prominent difference observable is the presence of wide dislocation walls in this work. These walls measure up to approximately 0.5 μm in width. One cause of this may be the difference in specimen orientation. TEM specimens in this study are oriented parallel to the plane of the rolled sheet, whereas Bay, Hansen, and coworkers, use specimens perpendicular to the width of the sheet (Figure 34). However, a more likely reason for the slight difference in rolled structure is the greater purity aluminum (99.996%) used in the work of Bay, Hansen, and coworkers.[56,75,76,79] Compared to the 99.94% purity aluminum used in this work, 99.996% represents over a 90% decrease in the impurity concentration. The greater impurity concentration may increase the likelihood of the interaction between a mobile dislocation and a dispersoid. The subsequent dislocation tangles then act as barriers to dislocation glide promoting the growth of extensive dislocation walls. A diffraction analysis reveals that the wide dislocation walls consist of dislocations of different systems (Figure 35).

Upon a light tensile straining into the early deformation regime, the dislocation substructure of the unrecrystallized microstructure is found to be of lesser strength (Figure 36). The overall appearance of the lightly deformed structure is comparatively cleaner than before deformation (Figures 33 and 35). Gaps in the dislocation bands as well as the decreased width of the dislocation walls themselves suggest that the pre-existing dislocation substructure dissolves upon deformation. A similar dissolution of the

pre-existing dislocation structure is also observed in low carbon steel. Gracio finds that the dislocation structure created during prestraining tends to evolve into one characteristic of the new loading condition.[168] This dissolution and rearrangement of the dislocation substructure occur during a short transient in the work hardening behavior after reloading. Schmitt and coworkers find a similar example in copper.[193] Further deformation beyond the early deformation regime eliminates the existence of this extensive dislocation structure altogether.

In contrast to the unrecrystallized microstructure, the recovered microstructure is nearly absent of any internal dislocation substructure prior to deformation (Figures 22 through 26). Although there is evidence of a slight residual dislocation substructure, as documented in Figures 25 and 26, the microstructure is much cleaner compared to the unrecrystallized condition (Figures 33 and 35). Comparison of the unrecrystallized and recovered structure also indicates a tightening of the subgrain boundaries as well as a slight coarsening of the subgrains during the low temperature annealing treatment. However, no major modification of the texture is expected. Figure 37 shows the recovered microstructure after deformation to the same stress level as the deformed unrecrystallized microstructure in Figure 36. In contrast to Figures 22 through 26, a dislocation substructure is now apparent. The large amount of strain contrast near the subgrain boundaries indicates that most of the dislocation activity is generated at the subgrain boundaries. This is reasonable because of the absence of an internal structure within the subgrain Such dislocation generation can be seen in Figures 37 through 39. Figure 38 demonstrates the general randomness of the dislocation substructure along with the beginnings of a dislocation network. A two-beam diffraction analysis shows that the dislocation tangles within the subgrains are composed of dislocations generated from neighboring sides of the same subgrain (Figure 39). Further deformation produces a high density of forest dislocations that dominates the deformation process (Figures 27 through 29).

LBL Specimens

Tensile Properties: LBL1 specimens

The task of the first LBL batch was to address the issue of texture in both the recrystallized and unrecrystallized microstructure. Engineering stress and strain properties obtained from LBL1 specimens are listed in Table V. For both the recrystallized and unrecrystallized microstructures, orientations were chosen to achieve the greatest degree of texture difference relative to the rolling direction. For the recrystallized structure, which contains a strong cube texture, this requires specimens machined 45° from the rolling direction whereas for the unrecrystallized, the greater texture difference is achieved with specimens oriented 90° from the rolling direction. A comparison of the mechanical properties with those of the KSL samples (Table II) reveals a drop in the strength level along with a corresponding increase in the elongations. For the unrecrystallized microstructure, this drop in strength and corresponding increase in elongation occurs despite the increased amount of cold-work introduced in the LBL1

specimens (50% cold rolling compared to 40% for KSL samples), indicating a strong sensitivity of the mechanical properties to the overall purity of the aluminum. A similar tradeoff between LBL1 and KSL specimens in the recrystallized condition can also be attributed to this impurity effect.

The increase in both yield and ultimate strengths associated with the off-angle test orientations is an expected effect of texture. For both microstructures, the increase in strength level is accompanied by a decrease in the uniform elongation. Both these effects may be attributed to the increase in the Taylor factor as shown by Equation (39). Assuming that the differences in properties are due to texture only, a ratio of the Taylor factors for the different orientations can be calculated by taking the ratio of yield strengths. For the recrystallized microstructure this produces a ratio of 1.06 relative to the yield strength parallel to the rolling direction. This ratio is sustained at the ultimate strengths, decreasing only slightly to a value of 1.04 when considering the true stresses at the necking point, σ_u, which can be calculated by the equation,

$$\sigma_u = s_u (1 + e_u) \tag{45}$$

where s_u is the engineering ultimate strength, and e_u is the elongation at the ultimate strength. The greater than one ratio is reasonable considering the relatively stronger cube texture features, (100)[001], typically observed with annealed aluminum microstructures. For the cube orientation, the tensile axis associated with the 45° specimens will be parallel to the [011] direction which by the calculations of Chin is a harder orientation.[204] The near unity value attests to the near random set of orientations achieved during the annealing process. On the other hand, a similar calculation for the unrecrystallized microstructure produces values of 1.08 at yield and 0.97 at necking. The lack of consistency in this ratio suggests that texture is not the only significant factor in the more complex microstructure.

Tensile Behavior: LBL1 specimens

Figure 40a shows the plots of the work hardening rates as a function of true stress for the recrystallized microstructure at 77 K for the two orientations, 0° and 45° from the rolling direction. Assuming that the ratio of Taylor factors associated with the different orientations is similar to the ratio of yield strengths (~1.05), the plot for the 45° specimen can be recalculated using Equations (39) and (40). The result, shown in Figure 40b, reveals a very good fit between the two curves within the bulk of the work hardening plot. The overlapping work hardening curves in Figure 40b suggest that for the recrystallized microstructure, texture is a dominant factor in determining the overall shape of the work hardening curve.

A similar plot of the work hardening curves for the unrecrystallized microstructures for the two orientations, 0° and 90°, reveals a contrasting response (Figure 41). Both orientations exhibit bi-linear work hardening curves similar in character to those of the KSL unrecrystallized microstructure. Unlike the work hardening plot obtained for the recrystallized specimens, the two orientations of the unrecrystallized microstructure are not completely parallel. As shown in Figure 41a, the 90° specimen

exhibits a steeper drop during the early work hardening regime relative to the 0° specimen. The near overlap of the work hardening curves associated with the two different orientations of the LBL1 unrecrystallized microstructure at large stresses is analogous to the KSL unrecrystallized and recovered microstructures. At stresses above approximately 150 MPa, both orientations follow similar deformation paths and subsequently reach approximately the same strength level. Similar to the KSL recovered microstructure, the lower work hardening rate associated with the 0° oriented specimen during the early regime results in a greater ductility relative to the 90° oriented specimen. Unlike the recrystallized microstructure, applying Equations (39) and (40) to the two curves in Figure 41a does not bring the two curves into coincidence, but rather causes the two curves to diverge, corroborating the earlier result that texture is not the only significant factor in the more complex microstructure.

Tensile Properties: LBL2 specimens

The results shown in Figure 41 raise a number of interesting issues. In particular, the near overlap of the 0° and 90° work hardening curve at high strains suggests that orientation is not a significant factor in the fully plastic regime. The task of the second LBL batch was to further investigate the bi-linear characteristics observed in the work hardening curves of the unrecrystallized microstructure. These tests are in essence interrupted deformation tests similar to those conducted by previous investigators.[162-197] Schmitt and coworkers have defined the parameter α, which is the inner product of the unit strain tensors involved.[163] The inner product, α, ranges from 1 to -1, the latter value of -1 representing a Bauschinger test. If we assume the initial rolling of the aluminum sheet is done in plane strain, then by definition, the unrecrystallized specimen represents an α of 0.87 which Rauch refers to as a pseudo-continuous test.[194]

Engineering stress and strain properties obtained from LBL2 specimens are listed in Table VI. Yield strength values for the 0° and 90° orientations are higher by approximately 12% for comparable orientations of the LBL1 specimens. This can be attributed to the greater amount of cold rolling experienced by the LBL2 sheet (approximately 60% cold reduction). Lower yield and ultimate strengths are measured at 45° from the rolling direction. This in-plane anisotropy is typical in rolled aluminum. A similar drop in the strength at 45° is also observed in the aluminum-copper-lithium alloy 2090.[46,49] Variations in strength as large as 15% have been reported.[46] In comparison, the variation in strengths for the LBL2 samples is only about 10%. The greater in-plane anisotropy obtained in the 2090 alloy is believed to be due to the heterogeneous nucleation of the plate precipitate T_1, along favored {111} planes.[206,207] A non-uniform distribution of these precipitates with respect to the four {111} variants results, which dictates the dependence of the strength with specimen orientation.

Tensile Behavior: LBL2 specimens

Figure 42 shows the work hardening curves for the three orientations in the unrecrystallized condition. Similar to the LBL1 samples, both the longitudinal and long-transverse orientations exhibit a bi-linear work hardening curve. Unlike the LBL1

samples, however, the two work hardening curves associated with the fully plastic regime do not overlap, but instead, exhibit a large shift. Nonetheless, the slope appears to be roughly constant for both 0° and 90° orientations. Table VII lists the measured work hardening parameters as described by the Kocks-Mecking model in Equation (20) for the LBL specimens. Note that except for the 45° orientation, the slopes of the latter regime for all LBL specimens are all on the same order as that obtained for the KSL unrecrystallized microstructure. In contrast to the 0° and 90° orientations, the work hardening curve obtained for the unrecrystallized specimens pulled at 45° from the rolling direction suggests that the latter deformation regime is never fully achieved.

The 90° orientation exhibits an increase in the early regime slope compared to the 0° orientation. This can be observed in Figure 42 as well as the measured values listed in Table VII. The increase in slope for the 90° orientation corroborates similar observations in the LBL1 specimens. Comparing the two LBL batches, however, the early regime slope measured for the LBL2 batch in both 0° and 90° orientations is greater than those measured for the LBL1 batch. This may be the result of the greater amount of cold rolling experienced by the LBL2 batch (60%) versus the LBL1 batch (50%). In addition, the early regime slopes of the 0° orientations are both less than the early regime slope measured for the KSL unrecrystallized specimen suggesting that the purity level of the material may also be important. A slight increase in slope between 0° and 90° orientations can also be seen in the latter regime slopes. However, because of the already low values, around 3 and 4, the difference in the latter regime slopes is less noticeable (Figure 42).

Comparing the two LBL batches, the early regime slope measured for the LBL2 batch in both 0° and 90° orientations is greater than those measured for the LBL1 batch. This may be the result of the greater amount of cold rolling experienced by the LBL2 batch (60%) versus the LBL1 batch (50%). In addition, the early regime slopes of the 0° orientations are both less than the early regime slope measured for the KSL unrecrystallized specimen suggesting that the purity level of the material may also be important.

Additional Tests and Results

Reannealed Specimens

Further tests on KSL samples were conducted in order to shed additional light on some of the more obvious questions produced by the results obtained. The first such question is the surprising consistency in the value of the slopes measured for the latter regimes of the recovered and unrecrystallized specimens. The above results suggest that the orientation of the subgrains is inconsequential to the work hardening process. In order to further document this finding, a recrystallized specimen was pulled to approximately 25% engineering strain and then reannealed at 225°C to recover the cellular structure into subgrains. This deformation routine differs from the recovered specimen which receives a 40% rolling prior to the recovery process and thus produces a

different subgrain morphology. Figure 43 shows a schematic demonstrating this difference.

The primary difference between the reannealed and recovered microstructures is the texture or distribution of subgrain orientations. Since the dislocation cells which form within the recrystallized microstructure are related to the original orientation of the grain, the resulting reannealed microstructure consists of colonies of closely oriented subgrains. The size of the colonies is necessarily on the order of the original grain size. The colonies themselves, however, are randomly oriented. Figure 44 shows the effect of this reannealing process near a grain boundary. Subgrains within the same grain are close in orientation, but exhibit a high degree of misorientation with subgrains in the adjacent grain. Note also that the subgrains are oriented about the [001] zone axis which is consistent with the cube texture typically observed in a recrystallized microstructure. The subgrain size was measured to be approximately 1.9 μm. As shown earlier, the recovered microstructure exhibits subgrains that are similarly oriented (Figures 22 through 26). Comparison between the two microstructures reveals that the reannealed sample contains less well-defined subgrains, the subgrain boundaries in many cases appearing like dense dislocation walls (Figures 45 and 46). Remnants of the cellular structure can also be seen. This lack of a complete recovery process is due to the lower amount of initial deformation (25% tension) incurred by the reannealed sample compared to the recovered sample (40% rolling). The smaller amount of deformation hinders the recovery process which relies on a high dislocation density.

Figure 47 shows the work hardening curves for the microstructures concerned. A comparison of the curves reveals that the reannealed specimen does not evolve back to the original recrystallized deformation path, in contrast to the recovered specimen which eventually overlaps the work hardening curve of the unrecrystallized specimen. More surprisingly, the slope of the latter regime measured for the reannealed sample is comparable to the slope exhibited by the recovered and unrecrystallized microstructures. A slope analysis shown in Table VIII shows this drop. The reannealing of the recrystallized microstructure causes K_2 of the latter regime to decrease significantly. The value of 3.95 measured for the reannealed microstructure approaches the value obtained for the recovered microstructure. Figures 48 and 49 show that the change in slope between the latter regimes of the recrystallized and reannealed structures is accompanied by a loss in the cellular dislocation substructure. The cellular dislocation substructure is replaced by one similar in features as that observed for the recovered and unrecrystallized microstructure (Figures 27 through 31), although the tendency for the dislocations to accumulate at the subgrain boundaries is stronger for the reannealed microstructure.

Pre-Compressed Specimens

Whereas the above tests on reannealed specimens establish the dominance of the subgrain within the latter deformation regime, a second set of tests was conducted to establish the dominance of a pre-existing dislocation density on the early deformation regime. Recrystallized tensile specimens were lightly compressed along the thickness

direction at room temperature prior to a tensile deformation. Figure 50 shows a schematic of the deformation path. The purpose of this compression is to introduce a dilute dislocation substructure which is different from the tensile direction. This is in essence a two-strain path deformation. Compared to the unrecrystallized specimens which undergo a rolling procedure prior to a tensile deformation, the compression represents a more drastic change in strain path. Schmitt and coworkers have defined the parameter, α, as the dot product between the two unit strain vectors describing the strain path before and after a path change.[164] A value of 1 represents a continuous test with no change in strain path, which values of 0 and -1 represent orthogonal and stress reversals respectively. The value of α calculated for the pre-compressed specimen is -0.17 which is significantly different from the value of 0.87 for the KSL unrecrystallized specimens.

Table IX shows the tensile properties obtained for the pre-compressed recrystallized specimen after a 3% compression along with those obtained by the recrystallized specimen for comparison. The increase in the yield strength indicates the strengthening effect of the dislocation substructure introduced during the pre-compression. The corresponding increase in the elongation is somewhat surprising, although this may be the result of the negative α value which indicates a slight stress reversal. Figure 51 shows the work hardening curves for the pre-compressed recrystallized specimen along with that of the recrystallized microstructure. The most outstanding feature is the near parallel nature of the curves in the fully plastic deformation regime. Measurements of the latter regime slopes reveal similar values for K_2 (Table X). In addition, the pre-compressed specimen exhibits a drop to lower work hardening rates. This drop in the work hardening rate along with the increase in the yield strength is typical of a positive transient, as described by Doucet and coworkers[168-170]. The near parallel behaviors of the two fully plastic regimes suggest that the pre-existent dislocation substructure does not influence the development of the deformed microstructure but does influence the stress level required for the development.

Near the necking criterion, the work hardening curve associated with the pre-compressed recrystallized microstructure bends again and meets up with the curve obtained for the recrystallized microstructure. This may signify that the deformation structure becomes identical at very high stresses. However, because of the proximity of this effect to the necking criterion, it is believed that this overlap is a geometric effect and is mostly coincidental. Furthermore, if it is assumed that the two curves do join, one may expect that the elongation after necking would be identical for the two microstructures. Table IX shows that this is not the case.

Another important feature to note is the short early deformation regime that precedes the fully plastic regime for the pre-compressed microstructure. Stress-strain data shows that the early regime extends 2% which is comparable to the 3% pre-compression. This suggests that the early regime is directly associated with the dislocation substructure produced by the pre-compression. Table X lists the slope of this early regime. Compared to the slopes of the early regimes measured for the unrecrystallized specimens (Tables III, VI, and VII), the early slope for the pre-

compressed specimen is significantly greater. This may be due in part to the drastic change in strain path experienced by the pre-compressed specimen.

Specimens containing a recovered microstructure were also pre-compressed for comparison. Table XI shows the tensile properties of the recovered microstructure after a 3% compression along with those obtained from the recovered microstructure. The increase in the yield strength is significantly less than that observed between the pre-compressed recrystallized and recrystallized microstructures. This is an indication of the lower early work hardening rate measured for the recovered microstructure. Figure 52 shows the work hardening curves for both recovered and pre-compressed recovered microstructures. In contrast to the pre-compressed recrystallized microstructure (Figure 51), the pre-compressed recovered microstructure exhibits a work hardening curve that follows along the original work hardening curve exhibited by the recovered specimen. Table XII shows that the work hardening parameters for the two microstructures are nearly identical. This overlap indicates that the pre-existent dislocation substructure in the recovered microstructure influences neither the development of the deformed microstructure nor the stress level required for the evolution of the deformed structure. The influence of the slight drop in the early work hardening rate determined for the pre-compressed recovered microstructure leads to the slightly higher uniform elongation value (Table XI).

DISCUSSION

Work Hardening Behavior

The most outstanding result obtained from this work is the existence of two distinct and separable deformation regimes. These deformation regimes are distinguishable from one another by their different slopes when plotting the work hardening rate versus true stress. Although the difference in slopes does not necessarily indicate a change in the deformation mechanism, it does indicate a change in the manner by which deformation evolves. Furthermore, the results indicate that each deformation regime is associated with a different structural feature.

Latter or Fully Plastic Regime

The evidence indicates that the latter, or fully plastic, regime is associated with the formation of a cellular dislocation substructure. When a dislocation cell structure develops, as is observed upon the deformation of a well-annealed structure (Figures 18 through 21), a relatively rapid drop in the work hardening curve results (Table III and IV). The mutual occurrence of a cellular structure and this rapid drop in the work hardening rate is not surprising. There is considerable evidence indicating the tendency to form a cellular dislocation structure with increasing temperature. Consequently, it is believed that the formation of a cellular dislocation structure is a result of dynamic recovery mechanisms which allow the reduction of the elastic strain energy during large deformations.[72,80,82,91,199,208] Studies show that the dislocation walls are sites for dislocation dipoles. These dislocation dipoles are characterized by dislocations on opposite sides of the dislocation cell wall being on the same slip system but of opposite sign.[70,186-189,192] This allows the mutual annihilation of dislocations to occur readily and thus results in a relatively large recovery rate. According to the Kocks-Mecking model (Equation 20), this produces a steep slope.[62,64,68]

The greater dynamic recovery rate may also be due to the reduction in the number of active slip planes. Bay, Hansen and coworkers have shown that the formation of a cellular dislocation substructure results from the fragmentation of the initial microstructure into cell blocks.[56,76,79] These cell blocks are further subdivided into dislocation cells. The key element in this fragmentation model is that Taylor's requirement of five slip systems during deformation is satisfied collectively by adjacent cell blocks and not by each cell block individually. Therefore, for any given region, the number of slip systems is generally smaller than five as suggested by Taylor's model[97]. This reduction in the number of slip systems activated within each individual cell block also acts to increase the dynamic recovery rate. It is evident from the results of this work that the formation of a cellular dislocation substructure requires an initially well-annealed microstructure. In order to maintain a minimum number of slip systems, the number of obstacles to dislocation glide must be kept to a minimum. If numerous enough, these obstacles would create complex strain fields which would require Taylor's five slip systems in order to maintain strain compatibility. The near elimination of obstacles is accomplished in pure single crystals as well as well-annealed polycrystals.

It is not surprising that the introduction of subgrains hinders the formation of a cellular dislocation substructure (Figures 27 through 31). This cellular dislocation structure, described by Kuhlmann-Wilsdorf as a low energy dislocation structure[72,80,82,91], must give way to one in which maintaining strain compatibility between subgrains becomes a significant factor. Kocks has noted a similar hindrance of a cellular dislocation structure near grain boundaries due to grain boundary stresses.[100] A model to be presented below indicates that approximately half of the dislocations generated in the recovered microstructure is absorbed by the subgrain boundaries. This appears to be a reasonable value. The large fraction of dislocations that accumulate at the subgrain boundaries produces a greater degree of out-of-plane rotation as observed in the slip relief study (Figure 32). The need to maintain strain compatibility between subgrains requires that all of Taylor's five slip systems be activated. This increase in the number of slip systems over the number necessary for cell formation increases the difficulty of dynamic recovery and results in a work hardening curve of flatter profile. This concept is shown schematically in Figure 53.

By far the most surprising result is the relative consistency in the value of the slope associated with the latter or fully plastic regime. Tables III, VII, and VIII show that the slope measured for the recovered, reannealed, and unrecrystallized microstructures vary between 3 and 4. This consistency spans both KSL and LBL specimens as well as both 0° and 90° specimens for the unrecrystallized microstructure. The latter result suggests that the orientation of the subgrains does not affect the slope of the work hardening curve in the large strain regime. Strong evidence for this is also supplied by a comparison of the recovered and reannealed samples (Figure 47). However, the various fully plastic regimes do not completely overlap for the spectrum of subgrain-bearing microstructures tested in this study. Despite the consistency in slope, the fully plastic regime exhibits a shift along the stress axis. One source of this shift is the purity level. The work hardening curves associated with the LBL specimens (< 99.96% purity) are shifted to lower stresses relative to KSL specimens (< 99.94% purity) (Tables III, VII, and VIII). Another possible source is the subgrain size. However, this study reveals no such connection between the stress shift and subgrain size. LBL2 unrecrystallized specimens exhibit considerable shifts along the stress axis despite the absence of any modification to the subgrain structure.

The lack of correlation between the subgrain size and the position of the work hardening curve relative to the stress axis suggests that the work hardening curve is not influenced by the stress level at which deformation is taking place. In other words, the microstructure responds to an applied strain regardless of the stress level required for that strain to be accommodated. This response differs depending on the particular microstructure. In the case of the recrystallized grain structure, a cellular dislocation substructure is observed. The introduction of a subgrain structure, however, hinders this cellular formation and deformation is now forced to be accommodated by a different mechanism. This alternative mechanism results in a dislocation substructure which is less well-defined than that observed for the recrystallized structure (Figures 18 through

21), which in turn, results in a different work hardening slope (Figure 14). Therefore, the subgrain structure only determines the path which the deformation must follow. It does not, however, influence the rate at which that deformation path is followed. The absence of an orientation effect in those microstructures containing subgrains further suggest that this alternative deformation path is not sensitive to the orientation distribution of the subgrains.

This reasoning does not necessarily rule out the influence of the subgrain structure on the stress level at which this deformation occurs. The specific characteristics of the subgrains may still change what has been termed by Kocks, Argon, and Ashby, as the "deformation resistance".[24] By definition, this deformation resistance is a macroscopic measure that describes the change in free energy of a material as it is being deformed. It is conceivable that this quantity is dependent on the specific characteristics of the subgrain structure.

Early Regime

The existence of an early deformation regime can be seen in all microstructures tested in this study. Stress-strain data shows that this early regime extends the first 2% of true strain for the recrystallized microstructure to as much as the first 7% of true strain for the reannealed microstructure. Table III shows that for the three annealed microstructures, recrystallized, partially recrystallized, and recovered microstructures, the value of K_2 in the early regime remains relatively constant, ranging in value between 11 and 12. This consistency despite drastically different microstructures suggests that this early regime is an unavoidable geometric or hysterisis effect. This type of early transition can be observed in tests in which a specimen is deformed in tension after which, the load is released. Upon reloading, the yield stress is often found to be lower than the flow stress prior to the initial unloading.

In contrast to the consistency detailed above, the KSL unrecrystallized microstructure exhibits a much greater slope ($K_2 = 14.5$) in the early regime. The results documented for the KSL unrecrystallized microstructure in Figures 14, 33, and 35 through 39, indicate that this higher K_2 value is a consequence of the residual dislocation substructure left by the previous straining. It is somewhat surprising that this pre-existent dislocation substructure has such a dramatic influence on the work hardening behavior. For the majority of specimens tested in this work, the initial dislocation substructure is obtained from cold rolling. Tensile tests are then conducted in the direction parallel to this rolling. This sequence of deformation paths yields an α of 0.87, where α is the dot product of the successive strain tensors as defined by Schmitt, Aernoudt, and Baudelet.[164] Since an α value of unity represents a continuous deformation path, the relatively high value of 0.87 indicates a relatively small change in strain path for the unrecrystallized specimens. Despite this small change in strain path, however, a 25% increase in the early regime slope is measured for the unrecrystallized microstructure relative to the annealed microstructures (Table III).

Relative to the 0° orientation, unrecrystallized specimens tested in both the 45° and 90° orientations exhibit a greater slope. This is expected given the more drastic change in strain path (α = 0.70 and 0.0 respectively). This increase in the early regime slope with a change in orientation suggests an orientation effect on the dynamic recovery rate, K_2. A similar effect has been observed in copper by Schmitt and coworkers.[193] Exposing copper sheets under sequential tensile stresses, they showed that reloading in a new direction causes the activation of previously inactive slip systems. The interaction of the mobile dislocation associated with the new slip systems with the pre-existent dislocation network promotes the dissolution of the previous dislocation arrangement thus producing an increase in the dynamic recovery rate during the work hardening transient.

Another source for the difference in the early regime slopes is the difference in texture. Table VI shows that the 90° orientation exhibits a greater yield strength than the 0° orientation. Comparison of the yield strengths reveals a 9% increase between the 0° and 90° orientation. From Equation (39), this increase can be assumed to be the same between Taylor factors for the two orientations. Table VII, however, shows that the value of K_2 exhibits an increase between the 0° and 90° orientations of well over 25%. Consequently, if texture does play a role in the early deformation regime, it is not the dominating factor.

The lack of a strong bi-linear work hardening curve for the LBL unrecrystallized specimens tested at 45° suggests that the pre-existent dislocation network has a substantial influence on the deformation behavior well into the fully plastic regime. Table VI reveals that a change in slope between the early and latter regimes does exist for the 45° orientation. However, this change in slope is much less than that measured for the other two orientations. In their work on copper sheets under sequential tensile stresses, Schmitt and coworkers showed that the number of new slip systems activated upon reloading reached a maximum when the new loading direction was 45° from the initial loading direction.[193] Inversely, this states that the dislocation network created during the rolling process are unfavorably oriented for further deformation at 45°. It is likely that this unfavorable orientation prevents a rapid dissolution of the pre-existent dislocation substructure.

Implications to Work Hardening Models

The results obtained in this study indicate a constitutive law describing the plastic deformation of aluminum requires more than one structural variable. This is in contrast to the work hardening models of both Kocks and Mecking as well as Kuhlmann-Wilsdorf.[62,64,71,80] In addition, the different slopes in the work hardening rate versus stress obtained for the recrystallized and recovered microstructures indicate that at least one additional structural variable is not isolated to early strains but significantly affects the overall deformation process. In this section, an attempt is made to resolve these additional variables through modifications of the existing work hardening models.

Kocks-Mecking Model

The Kocks-Mecking model was first developed from experiments on well-annealed pure metals.[62,64] In its basic form, the model indicates that the slope of the work hardening curve within the fully plastic regime is a constant, dependent only on the external variables of temperature and strain rate. The evidence acquired in this study, however, indicates that this conclusion is not general to all microstructures. As discussed previously, the reason for this change in slope is intimately related to the manner by which the dislocation substructure evolves during the deformation process. The work hardening curves obtained for the recrystallized and recovered microstructures provide the best example of this change in the deformation process. The parameters associated with Equation (20), Θ_o and K_2, are significantly different between the recrystallized and recovered structures.

A modified work hardening model based on the Kocks-Mecking model, can be constructed to account for the difference in the deformation process. The model considers only the recrystallized and recovered microstructures as these represent the cleanest microstructures, being nearly absent of any structures within the interior of the grains and subgrains respectively. The modification proposed considers the existence of subgrains. Following the concept of Ashby, the dislocation density is separated into those which are statistical and those which are geometrically necessary.[96] Equation (17), which describes the dislocation storage rate, then becomes,

$$\frac{d\rho}{d\gamma} = k_1\sqrt{\rho_s} - k_2\rho_s + k_3\sqrt{\rho_g} - k_4\rho_g\,, \tag{46}$$

where the subscripts, s and g, represent the statistical and geometric dislocations respectively. The storage rate of the geometric dislocations can be assumed to be reliant only on some characteristic dimension associated with the subgrains, for example, the subgrain size. Following Equation (12), the third term on the right hand side therefore becomes,

$$k_3\sqrt{\rho_g} = k_3\frac{\kappa}{\lambda_g}, \tag{47}$$

where λ_g is this characteristic dimension. The last term on the right hand side represents the dynamic recovery rate of the geometric dislocations. In this model, the geometric dislocations that accumulate at the subgrain boundaries are assumed to be incorporated into the subgrain boundaries and therefore do not undergo a mutual annihilation with one another. The last term on the right hand side can therefore be eliminated. The resulting dislocation storage rate then becomes,

$$\frac{d\rho}{d\gamma} = k_1\sqrt{\rho_s} - k_2\rho_s + k_3\frac{\kappa}{\lambda_g}. \tag{48}$$

Note that this is different from the modified Kocks-Mecking model proposed by Estrin and Mecking in Equation (34). Whereas the dislocation storage rate derived by Estrin and Mecking remains a constant, Equation (48) assumes two sources for the dislocation storage rate. Consequently, the interior of the subgrains is allowed to develop as first

assumed by Kocks. The subgrain structure simply adds additional sinks for the mobile dislocations.

Combining Equations (48) with the derivative of Equation (6) results in a modified work hardening equation,

$$\theta = \frac{d\tau}{d\gamma} = \frac{d\tau}{d\rho}\frac{d\rho}{d\gamma} = \frac{\alpha G b}{2\sqrt{\rho}}\left(k_1\sqrt{\rho_s} - k_2\rho_s + k_3\frac{\kappa}{\lambda_g}\right)$$

$$= \frac{\alpha G b k_1}{2}\sqrt{\frac{\rho_s}{\rho}} - \frac{\alpha G b k_2}{2}\sqrt{\frac{\rho_s^2}{\rho}} + \frac{\alpha G b k_3}{2}\frac{\kappa}{\lambda_g}\sqrt{\frac{1}{\rho}} \qquad (49)$$

Letting f_s represent the fraction of statistical dislocations, ρ_s/ρ, Equation (49) reduces to,

$$\theta = \theta_o\sqrt{f_s} - K_2 f_s \tau + \frac{\kappa}{\lambda_g}\frac{\zeta}{\tau}, \qquad (50)$$

where θ_o and K_2 are defined in Equations (18) and (19) and ζ is equal to the constant $(\alpha G b)^2 k_3/2$.

When the microstructure is well-annealed, as in the recrystallized microstructure, the fraction f_s is assumed to be near unity. In addition, the large grain sizes typical of a well-annealed microstructure result in a large λ_g value. The last term therefore reduces to zero and subsequently, Equation (50) reduces to Equation (19), the original Kocks-Mecking equation. The results obtained for the recrystallized KSL specimen (Table III), provides values of 1720 MPa and 8.55 for the initial work hardening rate Θ_o and K_2 respectively. For the recovered specimen λ_g is comparable to the subgrain size and hence is not an insignificant quantity. However, as a first approximation, this last term on the right hand side can still be approximated to be near zero when the stress is high as it is within the latter or fully plastic regime. Additionally, if the last term were significant, the work hardening curve should exhibit a hyperbolic shape, which the results do not bear out. Applying the values obtained from the recrystallized microstructure to that obtained from the recovered microstructure in the fully plastic regime results in a value of approximately 0.41 for f_s. Figure 54 shows the good fit obtained. The value of 0.41 obtained for f_s appears to be a reasonable number. Results of a slip relief study conducted on the partially recrystallized microstructure indicates considerable out-of-plane rotation of the subgrain structure (Figure 32). This out-of-plane rotation is a result of the greater density of geometric dislocations needed to maintain strain compatibility across the subgrain boundaries.

By definition, this decrease in the slope of the work hardening curve between the recrystallized and recovered microstructures implies that the dynamic recovery rate is reduced. TEM analysis shows that this reduction in the dynamic recovery rate occurs when the cellular dislocation substructure is hindered. The above model asserts that this decrease in the dynamic recovery rate is a result of the decrease in the density of dislocations present within the interior of the subgrains. It is assumed that the dislocations that are "geometrically necessary" and gather at the subgrain boundaries do

not recover but rather are incorporated into the subgrain structure. Consequently, the subgrain boundary exhibits no variation in strength. This may explain the absence of an orientation effect for the subgrain-bearing microstructures. In addition to predicting the slope of the work hardening curve, the model may provide some predictability to the shift of the work hardening curve along the stress axis. The last term in Equation (50) indicates that a shift to higher work hardening rates would occur with a decrease in the subgrain size. This agrees with the results obtained for recrystallized microstructures of different grain sizes from this study (Figure 13), as well as from the work of others[108,137-145]. However, a similar relation between the shift of the work hardening curve and the subgrain size remains unproved.

It should be noted that the above model is a first-attempt modification of the Kocks-Mecking model and serves only as an example. A number of different modifications can be proposed which are not discussed in this study. However, the fact that the observed trend in the work hardening behavior can be duplicated through such a simple modification suggests that Kocks' original concept is fundamentally sound.

Kuhlmann-Wilsdorf Model

The Kuhlmann-Wilsdorf model was originally developed for those materials in which the flow stress is dominated by the mutual elastic glide interactions between dislocations.[71,72,80,82,91] When this is true, dislocations will tend to assemble into configurations that allow neighboring dislocations to mutually screen their respective resolved shear stresses to levels below the material's own friction stress. Bassim and Kuhlmann-Wilsdorf have shown that such dislocation structures have low strain energies.[83-87] Dislocation structures that fit this description are dislocation cell structures and Taylor lattices. It is apparent from the results of this study, that the formation of such low-energy dislocation structures requires an initially well-annealed or recrystallized microstructure. Figures 18 through 21 reveal the well-defined cellular dislocation substructure that evolves in the recrystallized microstructure upon deformation.

When the microstructure is not in a fully recrystallized state, the formation of a low-energy dislocation structure is inhibited. Instead, a more random dislocation distribution is observed. The deformed structures obtained from the recovered and unrecrystallized specimens provide examples of this in Figures 27 through 31. In the terminology of Kuhlmann-Wilsdorf, these dislocation arrangements may be described as medium-energy or high-energy dislocation structures. This departure from low-energy dislocation structures in the recovered and unrecrystallized microstructures is due the introduction of other structural features, namely subgrain boundaries and pre-existent dislocation substructures, which produce other internal stresses that mask the elastic glide interactions between individual dislocations. An example of these additional internal stresses can be seen as strain contrasts emanating from the subgrain boundaries upon deformation in the recovered microstructure (Figure 37).

It is apparent from the discussion above, that the Mesh-Length theory does not span the more complex structures, in particular those grain or subgrain morphologies

which inhibit the formation of dislocation cells. Attempts to modify the Kuhlmann-Wilsdorf model involve understanding how the parameters β and g change in the presence of subgrain boundaries. Recall that β represents the fraction of mobile dislocations that are stored in the dislocation network.[71] Kuhlmann-Wilsdorf notes that β decreases from unity to near zero for those microstructures which develop a low-energy dislocation structure.[91] For subgrain-bearing microstructures, however, a substantial fraction of the mobile dislocations are geometrically necessary and are incorporated into the subgrain boundaries rather than stored in the dislocation network. Therefore β must now initially be less than unity. This fraction can be represented by βf_S, where f_S is the fraction of dislocations that are statistical in nature as developed in the previous section for the modified Kocks-Mecking model. The parameter βf_S therefore describes the fraction of mobile dislocations that are not "geometrically necessary". Equation (33) then becomes

$$\theta = \frac{2\alpha G}{m}\frac{\beta f_s}{g}. \tag{51}$$

The fraction β/g decreases monotonically with stress. The addition of the fraction f_S causes the decrease of β/g to be more gradual. This agrees with the observed trends in this study.

It is important to note that both the Kuhlmann-Wilsdorf and Kocks-Mecking model are developed from the basic characteristics of single crystals. Whereas the Mesh-Length theory is derived from the formation of cellular dislocation structures common to single crystals[71,72,80,82,91], the Kocks-Mecking model is derived from single crystals tested in a multiple slip orientation[62,64,69,100]. The consequence of this is that both models implicitly require the formation of low-energy dislocation structures. This fact is demonstrated by the breakdown of both models when the formation of such low-energy dislocation structures is inhibited. Therefore, the requirement of both models for a well-annealed structure is not simply to provide an initial structure that is relatively similar to that of a single crystal, but more importantly to ensure that the deformation path is similar to that observed in single crystals. It is difficult to ascertain the degree of annealing is necessary, or more appropriately, what minimum grain or subgrain size is sufficient for this latter requirement. The subgrain measured in this study are found to be approximately 2 μm in size. In addition, Hansen has noted that more than one cell block is necessary for strain compatibility to be fulfilled.[79] Hence it appears reasonable that a minimum grain or subgrain size lies near 10 to 20 μm.

Early Regime

The results of this work indicate that the early deviation in the work hardening behavior at low strains is a consequence of a pre-existent dislocation substructure. Neither the Kocks-Mecking model nor the Mesh-Length theory of Kuhlmann-Wilsdorf, at least in their basic forms, addresses this deviation. Rauch has proposed a model for mild steel in which the pre-existent dislocation structure undergoes an "un-storing" process.[195] The dislocation rate therefore becomes

$$\frac{d\rho}{d\gamma} = k_1\sqrt{\rho_r} - k_2\rho_r - k_3\sqrt{\rho_p}, \qquad (52)$$

where the subscripts, r and p, represent the dislocation density due to the reloading and pre-straining process respectively, and both k_1 and k_3 are indirect functions of strain. Upon reloading, the latter term decreases while the first term increases as the pre-existent dislocation network dissolves. Assuming that these functions are exponential in form, Rauch obtains a work hardening law that exhibits a hyperbolic-like drop during the early deformation regime. Although different in their assumptions, the modified Kocks-Mecking model proposed by Estrin and Mecking exhibits a similar result.[95]

The strong linearity of the early deformation regime contradicts the hyperbolic nature of the two proposed models above. Instead, the strong bi-linear character of the work hardening curves obtained in this work suggest that the two deformation regimes are independent and additive. Figure 6b shows the result of a two-parameter model in which both structure parameters evolve according to the Kocks-Mecking model. The resulting bi-linear work hardening plot is similar to those observed in this work. A work hardening model based on this concept has the form

$$\Theta = \frac{d\sigma}{d\varepsilon} = \Theta_{o1} + \Theta_{o2} - (K_{21} + K_{22})\,\sigma, \qquad (53)$$

where the second subscript represents the first and second structural parameters. The validity of this model, however, remains unproved.

Implications to Mechanical Properties

One of the more crucial issues raised in this study is the influence of the work hardening behavior on the subsequent mechanical properties. The important result obtained concerning this issue is the improved elongation obtained in the recovered microstructure in comparison to the other microstructures. The implication of this result is that improved ductility can be obtained through the elimination of high early work hardening rates and a decreased degradation in the work hardening rate with stress. This conclusion can also be obtained through a simple integration of the work hardening rate. The result of this operation leads to

$$\Delta\varepsilon = \int_{\sigma_y}^{\sigma} \frac{1}{\Theta}\, d\sigma. \qquad (54)$$

Since the work hardening rate is in the denominator, increased elongation is obtained when the initial work hardening rate is low but maintained to high stresses. Figure 14 shows that the recovered grain structure exhibits the best work hardening behavior based on this criterion. Table II reveals that the reduction of the early deformation regime associated with the unrecrystallized microstructure results in a 31% and 21% improvement in the uniform and total elongations respectively.

The ability to change the work hardening behavior through modifications of the microstructure is a key point in the development of structural materials. In particular, the results obtained in this study indicates the ability to significantly alter the mechanical behavior and subsequent properties without changing the internal chemistry. This result is particularly relevant to aluminum alloys which are typically precipitation hardened.

The microstructure of a precipitation hardened alloy can be separated into two levels: the *intra-* and *inter-* granular structure. The former includes the nature, size, and distribution of the various precipitates whereas the intergranular or polygranular structure is concerned with the distribution and orientation of grains and subgrains. The grain size, grain shape, as well as crystallographic texture all fall under this latter category. The intragranular structure is typically determined by the final heat treatment: quench rate, aging temperature, and aging time. The mechanical strength of a precipitation hardened alloy is typically contingent on the precipitate phases present and their volume fractions. Consequently, the ability of the precipitates to improve the alloy's properties is directly dependent on the aging treatment. To maintain optimum mechanical properties, the variables associated with the aging treatment are necessarily fixed. Any further improvement in the mechanical properties must therefore involve changes in the thermo-mechanical processing of the alloy *prior* to aging. Changes of this sort involve modifications of such variables as the rolling temperature, rolling speed, and percent reduction per pass. Previous work has documented the effect of these variables on the polygranular structure and subsequent mechanical behavior.[30-32,46,47,49]

FURTHER COMMENTS

A number of issues have come to the forefront as a consequence of this study. Most of these issues are themselves topics, which in the future, may demand extensive research. Some of the more outstanding issues are discussed below.

Influence of Subgrains on the Work Hardening Behavior

It is evident from the results of this study that the existence of subgrains plays a major role in determining the work hardening behavior in aluminum. The existence of a subgrains disrupts the formation of a more energetically favorable cellular dislocation substructure, thereby reducing the dynamic recovery rate. As a consequence, a more stable work hardening is achieved over a greater range of stress, resulting in superior strength and ductility. A model is proposed to explain this reduction in the dynamic recovery rate (Equations (46) through (50)).

Despite the success of the above model in explaining the change in the slope of the work hardening curve, it remains unclear what controls the shifting of the work hardening curve along the stress axis (Figures 42, 47, and 51). The most obvious feature that can be hypothesized as the cause for this shifting is the subgrain size. Similar to the idea first proposed by Hall[106] and Petch[107], the subgrain boundaries obstruct the transmission of slip from subgrain to subgrain. A smaller subgrain size increases the resistance of the subgrain boundary to dislocation pile-ups and hence, increases the stress required to instigate deformation. This latter stress can be viewed as a "background" or "friction" stress. Assuming that the evolution of the dislocation network is only a function of the stress above this "background" stress, the decrease in subgrain size would produce a shift of the work hardening curve to higher stresses.

Despite the apparent feasibility of the above notion, the majority of results from this work are in contradiction. Figure 47 provides the best example of this contradiction. Although the subgrain size of the reannealed microstructure was measured to be 1.9 μm, smaller than the 2.2 μm measured for the recovered microstructure, the fully plastic regime exhibits a shift to lower stresses, opposite of what is predicted by Hall[106] and Petch[107].

The shift of the work hardening curve also appears to be not related to texture. The reannealed microstructure retains the texture of the recrystallized microstructure which is more random and hence has a higher Taylor factor associated with it. According to Equation (39), this greater Taylor factor will result in an increase in the flow stress, which again is not observed for the reannealed microstructure. Further evidence against a texture effect is found in the LBL specimens. Whereas LBL1 unrecrystallized specimens tested in both 0° and 90° exhibit nearly overlapping latter deformation regimes, LBL2 unrecrystallized specimens tested in the same two orientations exhibit a relative shift of approximately 50 MPa (Figure 42). Furthermore, this shift of 50 MPa is in the opposite direction of what is predicted by texture; the fully plastic regime of the LBL2

unrecrystallized specimens tested in the 90° orientation exhibits a shift to lower stresses relative to similar specimens tested at 0° despite a greater yield stress.

The various contradictions alluded to above indicate that neither subgrain size nor subgrain orientation influences the position of the work hardening curve relative to the stress. The only other structural feature that can potentially influence the position of the work hardening curve is the subgrain boundary itself. A possible line of reasoning is that the subgrain boundaries of greater misorientations are more resistant to the transmission of slip and therefore increase the "background" stress of the material. Assuming this to be true, the structural feature of importance is the average subgrain boundary misorientation or the distribution of subgrain boundary misorientations. It would appear from this conjecture, that a microstructure consisting of a very small grain size should exhibit the highest stress level. A detailed study of this hypothesis is left for future research.

Influence of Solutes on the Work Hardening Behavior

The majority of earlier research on the subject of work hardening has concentrated on the deformation behavior in single crystals or well-annealed polycrystals. The efforts of Kuhlmann-Wilsdorf[71,72,80,81,82], Kocks[62,69,70,100], Hansen[75,79], and many others, have provided a secure basis for understanding work hardening at this level. However, most materials used today contain microstructures that are drastically more complex than those found in single crystals and well-annealed polycrystals. In order to understand the deformation behavior of these more complex microstructures, our current basis of understanding must be expanded to include the numerous other structural features that can be defined.

In general, these other structural features and their influence on the work hardening behavior can be separated into different areas: (i) the influence of the grain/subgrain morphology, (ii) the influence of solutes, and (iii) the influence of second phases. Most efforts including the current study are directed at the first area. It is apparent from the results obtained in this work that the primary influence of the grain/subgrain morphology is on the evolution of the dislocation density upon deformation. Earlier results obtained by Ashby[96], Li[147], and Thompson[148], although more indirect, confirm this conclusion.

In comparison, little is known about the influence of solutes and second phases on the marcoscopic work hardening behavior. The majority of work in the second area has concentrated on the influence of solutes on the instantaneous flow strength.[15-23] Only recently, has work commenced on understanding the influence of solutes on the evolution of the deformed microstructure. Hughes has conducted a detailed study of the microstructural evolution in an aluminum alloy containing 5% magnesium in solid solution.[57] In the well-annealed condition, the microstructure upon deformation is similar in appearance as that observed in well-annealed pure aluminum; grains are subdivided into misoriented regions in which deformation occurs on fewer slip systems

than specified by Taylor[97] for strain accommodation.[56,76,79] However, because of the increase in the friction stress resulting from the magnesium solutes, the individual regions do not further subdivide into dislocation cells but rather evolve into differently oriented Taylor lattices.[57] These Taylor lattices consist of uniform arrays of edge dislocations that are stabilized by secondary slip. Although the dislocations in a Taylor lattice are not clustered to minimize their energy as in cell walls, their organization into arrays of alternating sign still lowers their energy below that of a random distribution.[8,72,82]

A preliminary set of tensile tests was performed on aluminum alloys containing 2.5% and 5.0% magnesium in the recrystallized condition. Figure 55 shows the work hardening plots of the two alloys along with the pure aluminum recrystallized and recovered microstructures studied in this work. Note that the addition of magnesium in solution accomplishes the same reduction in the dynamic recovery rate as does the introduction of subgrains in pure aluminum. Table XIII shows that the value of K_2 approaches the value obtained for the recovered microstructure with increasing magnesium content. It is interesting to note that the recrystallized microstructures containing magnesium exhibit nearly the same Θ_0 value which suggests that the parameter Θ_0 is associated with the grain and subgrain morphology and not a strong function of the constituents within the grain or subgrain interior. Equally interesting is the increasing steepness of the work hardening curve with increasing stress exhibited by the 5.0% magnesium sample. The negative $d\Theta/d\sigma$ value is not predicted in any model known to this author. Table XIV shows that the addition of magnesium increases both the strength and elongation of the recrystallized structure. Note that the yield strength of the recovered microstructure is greater than that of the binary alloys. However, because of the dramatic increase in the work hardening rate, the magnesium-bearing microstructures exhibit dramatically higher ultimate strengths. In particular, the 5.0% magnesium specimen exhibits nearly twice the ultimate strength of the pure aluminum recovered microstructure. the yield strength of the recovered microstructure is greater than that of the binary alloys. It is likely that a combination of both subgrains and solutes will further improve the work hardening behavior. A detailed study of this hypothesis is left for future research.

Influence of Precipitates on the Work Hardening Behavior

The influence of second phases on the work hardening behavior stands as the least understood of the three areas defined above. Although much critical work has been conducted on the influence of precipitates and dispersoids on the mobility of dislocations, any macroscopic work hardening model containing these interactions continues to be elusive. The development of such a model becomes more difficult when the various potential characteristics of a precipitate are considered, namely the size, shape, volume fraction, as well as the type of boundary, coherent, semi-coherent, and non-coherent.

Precipitates typically increase the resistance to dislocation motion of the matrix. This increase in deformation resistance leads to a work hardening curve that is both greater in work hardening rate and stress level. The increase in the strength level that

accompanies the introduction of precipitates makes such precipitate-bearing aluminum alloys viable candidates for structural applications. However, the increase in the work hardening rate is often associated with intense strain localization at the precipitates which can lead to very poor ductility.

In general, precipitation hardened alloys do not exhibit a bi-linear work hardening curve as observed in this study. This is because any influence from a pre-existent dislocation structure is overshadowed by the high stress level required for dislocation motion through the precipitate-bearing matrix. However, there is evidence that precipitates influence the very-early work hardening behavior. Unlike the sharp drops from the elastic modulus observed in this study (Figure 14), work by Tseng has shown a slightly more gradual drop in the very-early work hardening curve for an aluminum-copper-lithium alloy.[32] Although this very-early regime covers only the first 0.5 to 1 percent strain, initial calculations indicate that it may have a large bearing on the mechanical properties. Equation (54) shows that any deviation from a sharp drop will result in a loss in elongation. Figure 56 shows a schematic illustrating this. A theoretical calculation by Tseng using data obtained from an aluminum-copper-lithium alloy, shows that the shaded area shown in Figure 56 can account for nearly a 25% loss in strain.[32] It is proposed that this gradual drop is a result of heterogeneous yielding. Strain is initially localized near the precipitates, causing some regions to yield before others. As the dislocation density increases, yielding spreads to adjacent regions until the strain localizations are overshadowed by forest dislocations. A detailed study of this hypothesis is left for future research.

SUMMARY AND CONCLUSIONS

The work hardening behavior of aluminum is found to be bi-linear in character. The two linear regimes can be separated into the early deformation regime and the latter or fully plastic deformation regime. The earlier deformation regime, which can extend up to approximately 10% strain, exhibits a relatively rapid drop in the work hardening rate with increasing true stress. In contrast, the latter deformation regime that immediately follows, exhibits a more gradual drop. A TEM investigation reveals that the existence of an early deformation regime is concurrent with the existence of a dislocation substructure formed during a previous deformation process. The extent and slope of this early deformation regime are dependent on the strength of the pre-existent dislocation substructure as well as the orientation of the pre-existent dislocation substructure relative to the new strain path. Low-temperature annealing treatments cause the dissolution of the pre-existent dislocation substructure, resulting in the reduction of this early deformation regime.

In comparison, the latter regime is dominated by the initial grain and/or subgrain morphology. Recrystallized or well-annealed microstructures exhibit a more rapid drop in the work hardening rate with increasing true stress than microstructures which remain partially recrystallized or unrecrystallized. TEM analysis reveals that the fully recrystallized structure develops a low-energy cellular dislocation substructure upon deformation. The existence of subgrains, however, hinders the formation of this cellular dislocation substructure. Instead, a more random arrangement of dislocation is observed. It is believed that this impediment to the formation of the low-energy dislocation cell network increases the difficulty of dynamic recovery processes and thus results in a more shallow drop in the work hardening rate. Preliminary work on aluminum-magnesium solid solutions indicates that this reduction in the dynamic recovery rate can also be accomplished through the addition of solutes. Whereas the orientation of the pre-existent dislocation substructure influences the slope of the early deformation regime, the orientation of the subgrain structure does not influence the slope of the work hardening curve within the latter regime. This latter result suggests that the work hardening behavior is strain-controlled.

The variations in the work hardening behavior is found to significantly influence the subsequent mechanical properties. The more shallow latter regime slope associated with the recovered microstructure in comparison with the recrystallized microstructure leads to improvements in both strength and ductility. Similarly, the reduction of the early deformation regime associated with the unrecrystallized microstructure results in a 30% and 20% increase in the uniform and total elongation respectively in the recovered microstructure.

In contrast to the work hardening models that utilize a single structure parameter, the dislocation density, the bi-linear character of the work hardening curve for aluminum demands that at least two structural features play significant roles. The success of the models proposed in this study suggest that the additional structural features are

essentially various divisions of the dislocation density: statistical dislocations which accommodate for the overall deformation process, geometrically necessary dislocations which accommodate the strain compatibility at grain and subgrain boundaries, and those dislocations created during a previous straining.

REFERENCES

1 E. Orowan: *Z. Physik*, vol. 89, 1934, pp. 605-613.

2 E. Orowan: *Z. Physik*, vol. 89, 1934, pp. 614-633.

3 E. Orowan: *Z. Physik*, vol. 89, 1934, pp. 634-659.

4 E. Orowan: *Z. Physik*, vol. 97, 1935, pp. 573-595.

5 E. Orowan: *Z. Physik*, vol. 98, 1936, pp. 382-387.

6 E. Orowan: *Proc. Phys. Soc.*, vol. 52, 1940, pp. 8-22.

7 M. Polanyi: *Z. Physik*, vol. 89, 1934, pp. 660-664.

8 G.I. Taylor: *Proc. Roy. Soc. London A*, vol. 145, 1934, pp. 362-387.

9 G.I. Taylor: *Proc. Roy. Soc. London A*, vol. 145, 1934, pp. 388-404.

10 R.E. Peierls: *Proc. Phys. Soc.*, vol. 52, 1940, pp. 34-37.

11 F.R.N. Nabarro: *Proc. Phys. Soc.*, vol. 59, 1947, pp. 256-272.

12 F.R.N. Nabarro: *Adv. Phys.*, vol. 1, 1952, pp. 269-394.

13 F.C. Frank: *Phil. Mag.*, vol. 42, 1951, p. 809-819.

14 *Dislocations and Mechanical Properties of Crystals*, J.C. Fisher, W.G. Johnston, R. Thomson, T. Vreeland, Jr., eds., John Wiley and Sons, Inc., New York, 1957.

15 *Dislocations and Properties of Real Materials*, The Institute of Metals, London, 1985.

16 *Symposium on Fiftieth Anniversary of the Introduction of Dislocations, Metall. Trans. A*, vol. 16, 1985, pp. 2080-2240.

17 A.H. Cottrell: *Dislocations and Plastic Flow in Crystals*, Clarendon Press, Oxford, 1953.

18 W.T. Read: *Dislocations in Crystals*, McGraw-Hill, New York, 1953.

19 J. Friedel: *Dislocations*, Pergamon Press, Oxford, 1964.

20 J. Weertman and J.P. Weertman: *Elementary Dislocation Theory*, The Macmillan Company, New York, 1964.

21 D. Hull: *Introduction to Dislocations*, Pergamon Press, Oxford, 1965.

22 F.R.N. Nabarro: *Theory of Crystal Dislocations*, Clarendon Press, Oxford, 1967.

23 J.P. Hirth and J. Lothe: *Theory of Dislocations*, McGraw-Hill, New York, 1968.

24 U.F. Kocks, A.S. Argon, M.F. Ashby: *Thermodynamics and Kinetics of Slip, Progress in Materials Science*, vol. 19, B. Chalmers, J.W. Christian, T.B. Massalski, eds., Pergamon Press, Oxford, 1975.

25 R. Hill: *The Mathematical Theory of Plasticity*, Oxford, 1950.

26 W. Prager and P.G. Hodge, Jr.: *Theory of Perfectly Plastic Solids*, John Wiley and Sons, New York, 1951.

27 W. Johnson and P.B. Mellor: *Engineering Plasticity*, Van Nostrand Reinhold, London, 1973.

28 *Proceedings of the International Conference on Low Energy Dislocation Structures*, M.N. Bassim, W.A. Jesser, D. Kuhlmann-Wilsdorf, H.G.F. Wilsdorf, eds., *Mater. Sci. and Eng.*, vol. 81, 1986.

29 *Proceedings of the 2nd International Conference on Low-Energy Dislocation Structures*, M.N. Bassim, W.A. Jesser, D. Kuhlmann-Wilsdorf, and G.J. Shiflet, eds., *Mater. Sci. and Eng. A*, vol. A113, 1989.

30 D. Chu and J.W. Morris, Jr.: *Adv. Cryo. Eng. A*, vol. 40, 1993, pp. 1355-1362.

31 D. Chu, C. Tseng, and J.W. Morris, Jr.: *Adv. Cryo. Eng. A*, vol. 38, 1991, pp. 37-44.

32 C. Tseng: *Master's Thesis*, University of California, Berkeley, 1993.

33 J.M. Barsom and S.T. Rolfe: *Eng. Frac. Mech.*, vol. 2, 1971, pp. 341-357.

34 J.M. Barsom and J.V. Pellegrino: *Eng. Frac. Mech.*, vol. 5, 1973, pp. 209-221.

35 E.R. Parker: *Brittle Behavior of Engineering Structures*, John Wiley & Sons, New York, 1957, pp. 253-302.

36 P.F. Thomason: *Int. J. Fract. Mech.*, vol. 7, 1971, pp. 409-419.

37 R.O. Ritchie, W.L. Server, and R.A. Wullaert: *Metall. Trans. A*, vol. 10, 1979, pp. 1557-1570.

38 R.O. Ritchie and A.W. Thompson: *Metall. Trans. A*, vol. 16, 1985, pp. 233-248.

39 K.S. Chan: *Metall. Trans. A*, vol. 20, 1989, pp. 155-164.

40 J.D. Embury and E. Nes: *Z. Metallkde*, vol. 64, 1973, pp. 805-812.

41 D.J. Lloyd, H. Sang, J.D. Embury, P. Wycliffe, and G. Leroy: *Mater. Sci. and Eng.*, vol. 36, 1978, pp. 35-46.

42 D.J. Lloyd and D. Kenny: *Metall. Trans. A*, vol. 13, 1982, pp. 1445-1452.

43 J. Glazer, S.L. Verzasconi, E.N.C. Dalder, W. Yu, R.A. Emigh, R.O. Ritchie, and J.W. Morris, Jr.: *Adv. Cryo. Eng.*, vol. 32, 1986, pp. 397-404.

44 J. Glazer, S.L. Verzasconi, R.R. Sawtell, and J.W. Morris Jr.: *Metall. Trans. A*, vol. 18, 1987, pp. 1695-1701.

45 J. Glazer: *PhD Thesis*, University of California, Berkeley, 1989.

46 D. Chu: *Master's Thesis,* University of California, Berkeley, 1990.

47 D. Chu and J.W. Morris, Jr.: *Metall. Trans. A*, vol. 22, 1991, pp. 1789-1799.

48 R.W.K. Honeycombe: *The Plastic Deformation of Metals*, 2nd ed., Edward Arnold, London, 1984, p. 457.

49 D. Chu and J.W. Morris, Jr.: in *Light-Weight Alloys for Aerospace Applications II*, E.W. Lee and N.J. Kim, eds., TMS-AIME, Warrendale, 1991, pp. 45-63.

50 Y. Kurihara: *J. of Metals*, vol. 45, no. 11, 1993, pp. 32-33.

51 Y. Kurihara: *J. of Metals*, vol. 46, no. 2, 1993, pp. 33-35.

52 Y. Kurihara: *J. of Metals*, vol. 46, no. 5, 1993, pp. 12-13.

53 A.K. Sachdev: *Metall. Trans. A*, vol. 21, 1990, pp. 165-175.

54 P.E. Armstrong, J.E. Hockett, and O.D. Sherby: *J. Mech. Phys. Solids*, vol. 30, 1982, pp. 37-58.

55 A. Korbel, J.D. Embury, M. Hatherly, P.L. Martin, and H.W. Erbsloh: *Acta Metall.*, vol. 34, 1986, pp. 1999-2009.

56 B. Bay, N. Hansen, D.A. Hughes, and D. Kuhlmann-Wilsdorf: *Acta Metall.*, vol. 40, 1992, pp. 205-219.

57 D.A. Hughes: *Acta Metall.*, vol. 41, 1993, pp. 1421-1430.

58 R. Pearce: *Sheet Metal Forming*, Hilger Publishing, Bristol, 1991, p. 87.

59 M. Zehetbauer and V. Seumer: *Acta Metall.*, vol. 41, 1993, pp. 577-588.

60 M. Zehetbauer: *Acta Metall.*, vol. 41, 1993, pp. 589-599.

61 E. Voce: *J. Inst. Metals*, vol. 74, 1948, pp. 537-562.

62 U.F. Kocks: *J. of Eng. Mat. and Tech., Trans. of the ASME*, 1976, pp. 76-85.

63 J.E. Hockett and O.D. Sherby: *J. Mech. Phys. Solids*, vol. 23, 1975, pp. 87-98.

64 H. Mecking: in *Work Hardening in Tension and Fatigue*, A.W. Thompson, ed., TMS-AIME, New York, 1975, pp. 67-88.

65 H.M. Otte and J.H. Hren: *Exper. Mech.*, vol. 6, 1966, pp. 177-193.

66 M.R. Staker and D.L. Holt: *Acta Metall.*, vol. 20, 1972, pp. 569-579.

67 H. Mecking and U.F. Kocks: *Acta Metall.*, vol. 29, 1981, pp. 1865-1875.

68 K. Lucke and H. Mecking: in *Inhomogeneity of Plastic Deformation*, ASM, Metals Park, 1972, pp. 223-250.

69 U.F. Kocks: *Acta Metall.*, vol. 6, 1958, pp. 85-94.

70 U.F. Kocks: in *Dislocations and Properties of Real Materials*, The Institute of Metals, London, 1985, pp. 125-143.

71 D. Kuhlmann-Wilsdorf: in *Work Hardening*, J.P Hirth and J. Weertman, eds., Gordon and Breach, New York, 1968, pp. 97-139.

72 D. Kuhlmann-Wilsdorf: *Mater. Sci. and Eng. A*, vol. 113, 1989, pp. 1-41.

73 J.W. Steeds: *Proc. Roy. Soc. A*, vol. 292, 1966, pp. 343-373.

74 P.B. Hirsch and T.E. Mitchell: in *Work Hardening*, J.P. Hirth and H. Weertman, eds., Gordon and Breach, New York, 1968, pp. 65-95.

75 N. Hansen and D. Kuhlmann-Wilsdorf: *Mater. Sci. and Eng.*, vol. 81, 1986, pp. 141-161.

76 B. Bay, N. Hansen, D. Kuhlmann-Wilsdorf: *Mater. Sci. and Eng. A*, vol. 113, 1989, pp. 385-397.

77 D.A. Hughes and W.D. Nix: *Mater. Sci. and Eng. A*, vol. 122, 1989, pp. 153-172.

78 D.A. Hughes and N. Hansen: *Mater. Sci. Technol.*, vol. 7, 1991, pp. 544-553.

79 N. Hansen: in *Modeling the Deformation of Crystalline Solids*, T.C. Lowe, A.D. Rollett, P.S. Follansbee, and G.S. Daehn, eds., TMS-AIME, Warrendale, 1991, pp. 37-49.

80 D. Kuhlmann-Wilsdorf: *Trans. AIME*, vol. 224, 1962, pp. 1047-1061.

81 D. Kuhlmann-Wilsdorf and J.H. van der Merwe: *Mater. Sci. and Eng.*, vol. 55, 1982, pp. 79-83.

82 D. Kuhlmann-Wilsdorf: *Mater. Sci. and Eng.*, vol. 86, 1987, pp. 53-66.

83 M.N. Bassim and D. Kuhlmann-Wilsdorf: *Phys. Status Solidi A*, vol. 15, 1973, pp. 725-734.

84 M.N. Bassim and D. Kuhlmann-Wilsdorf: *Phys. Status Solidi A*, vol. 16, 1973, pp. 241-251.

85 M.N. Bassim and D. Kuhlmann-Wilsdorf: *Phys. Status Solidi A*, vol. 17, 1973, pp. 281-292.

86 M.N. Bassim and D. Kuhlmann-Wilsdorf: *Phys. Status Solidi A*, vol. 17, 1973, pp. 379-393.

87 M.N. Bassim and D. Kuhlmann-Wilsdorf: *Phys. Status Solidi A*, vol. 19, 1973, pp. 335-346.

88 P. Jackson and D. Kuhlmann-Wilsdorf: *Scripta Metall.*, vol. 16, 1982, pp. 105-107.

89 F.C. Frank and W.T. Read: *Phys. Rev.*, vol. 74, 1950, pp. 722-723.

90 F.R.N. Nabarro, Z.S. Basinski, and D.B. Holt: *Advan. Phys.*, vol. 13, 1964, pp. 193-323.

91 D. Kuhlmann-Wilsdorf: in *Modeling the Deformation of Crystalline Solids*, T.C. Lowe, A.D. Rollett, P.S. Follansbee, and G.S. Daehn, eds., TMS-AIME, 1991, pp. 105-124.

92 A. Seeger, J. Diehl, S. Mader, and H. Rebstock: *Phil. Mag.*, vol. 2, 1957, pp. 323-350.

93 A. Seeger: in *Dislocations and Mechanical Properties of Crystals*, J.C. Fisher, W.G. Johnston, R. Thomson, T. Vreeland, Jr., eds., John Wiley and Sons, Inc., New York, 1957.

94 H. Mecking, B. Nicklas, N. Zarubova, and U.F. Kocks: *Acta Metall.*, vol. 34, 1986, pp. 527-535.

95 Y. Estrin and H. Mecking: *Acta. Metall.*, vol. 32, 1984, pp. 57-70.

96 M.F. Ashby: *Phil. Mag.*, vol. 21, 1970, p. 399-424.

97 G.I. Taylor: *J. Inst. Metals,* vol. 62, 1938, pp. 307-324.

98 J.F.W. Bishop and R. Hill: *Phil. Mag.*, vol. 42, 1951, pp. 414-427.

99 J.F.W. Bishop and R. Hill: *Phil. Mag.*, vol. 42, 1951, pp. 1298-1307.

100 U.F. Kocks: *Metall. Trans.*, vol. 1, 1970, pp. 1121-1143.

101 C.S. Barrett and L.H. Levenson: *Trans. AIME*, vol. 137, 1940, pp. 112-126.

102 W. Boas and M.E. Hargreaves: *Proc. Roy. Soc. A*, vol. 193, 1948, pp. 89-97.

103 J.C.M. Li and Y.T. Chou: *Metall. Trans.*, vol. 1, 1970, pp. 1145-1176

104 A.W. Thompson: in *Work Hardening in Tension and Fatigue*, A.W. Thompson, ed., TMS-AIME, 1977, pp. 89-126.

105 A. Lasalmonie and J.L. Strudel: *J. Mater. Sci.*, vol. 21, 1986, pp. 1837-1852.

106 E.O. Hall: *Proc. Phys. Soc. B*, vol. 64, 1951, pp. 747-753.

107 N.J. Petch: *J. Iron Steel Inst.*, vol. 173, 1953, pp. 25-32.

108 N.J. Petch: *Phil. Mag.*, vol. 1, 1956, pp. 186-190.

109 J. Heslop and N.J. Petch: *Phil. Mag.*, vol. 1, 1956, pp. 866-873.

110 J. Heslop and N.J. Petch: *Phil. Mag.*, vol. 2, 1957, pp. 649-658.

111 A. Cracknell and N.J. Petch: *Acta Metall.*, vol. 3, 1955, pp. 186-189.

112 N.J. Petch: *Phil. Mag.*, vol. 3, 1958, pp. 1089-1097.

113 J. Heslop and N.J. Petch: *Phil. Mag.*, vol. 3, 1958, pp. 1128-1136.

114 I. Codd and N.J. Petch: *Phil. Mag.*, vol. 5, 1960, pp. 30-42.

115 R. Armstrong, I.Codd, R.M. Douthwaite, and N.J. Petch: *Phil. Mag.*, vol. 7, 1962, pp. 45-58.

116 R.P. Carreker, Jr., and W.R. Hibbard, Jr.: *Acta Metall.*, vol. 1, 1953, pp. 655-663.

117 R.P. Carreker, Jr.: *Trans. AIME*, vol. 209, 1957, pp. 112-115.

118 R.P. Carreker, Jr. and W.R. Hibbard, Jr.: *Trans. AIME*, vol. 209, 1957, pp. 1157-1163.

119 Y. Nakada and A.S. Keh: *Metall. Trans.*, vol. 2, 1971, pp. 441-447.

120 A.W. Thompson: *Acta Metall.*, vol. 23, 1975, pp. 1337-1342.

121 W.D. Klopp, W.R. Witzke, and P.L. Raffo: *Trans. AIME*, vol. 233, 1965, pp. 1860-1866.

122 M.A. Adams, A.C. Roberts, and R.E. Smallman: *Acta Metall.*, vol. 8, 1960, pp. 328-337.

123 M.J. Marcinkowski and H.A. Lipsitt: *Acta Metall.*, vol. 10, 1962, pp. 95-111.

124 D. Hull: *Acta Metall.*, vol. 9, 1961, pp. 191-204.

125 M.J. Marcinkowski and R.M. Fisher: *Trans. AIME*, vol. 233, 1965, pp. 293-298.

126 J. Harding: *Acta Metall.*, vol. 17, 1969, pp. 949-958.

127 N.J. Petch and E. Wright: *Proc. Roy. Soc. A*, vol. 370, 1980, pp. 17-27.

128 N.J. Petch and E. Wright: *Proc. Roy. Soc. A*, vol. 370, 1980, pp. 29-39.

129 C.J. Ball: *J. Iron Steel Inst.*, vol. 191, 1959, pp. 232-236.

130 D.H. Warrington: *J. Iron Steel Inst.*, vol. 201, 1963, pp. 610-613.

131 E.S. Meieran and D.A. Thomas: *Trans. AIME*, vol. 233, 1965, pp. 937-943.

132 J.D. Baird: *J. Iron Steel Inst.*, vol. 204, 1966, pp. 44-45.

133 M.J. Roberts and W. Jolley: *Metall. Trans.*, vol. 1, 1970, pp. 1389-1398.

134 R.J. McElroy and Z.C. Szkopiak: *Inter. Metall. Rev.*, vol. 17, 1972, pp. 175-202.

135 L. Anand and J. Gurland: *Metall. Trans. A*, vol. 7, 1976, pp. 191-197.

136 H. Conrad and G. Shoek: *Acta Metall.*, vol. 8, 1960, pp. 791-796.

137 H. Conrad, S. Feuerstein, and L. Rice: *Mater. Sci. and Eng.*, vol. 2, 1967, pp. 157-168.

138 N. Hansen: *Acta Metall.*, vol. 25, 1977, pp. 863-869.

139 J.T. Al-Haidary, N.J. Petch, E.R. De Los Rios: *Phil. Mag. A*, vol. 47, 1983, pp. 869-890.

140 J.T. Al-Haidary, N.J. Petch, E.R. De Los Rios: *Phil. Mag. A*, vol. 47, 1983, pp. 891-902.

141 N. Hansen and B. Ralph: *Acta Metall.*, vol. 30, 1982, pp. 411-417.

142 H.H. Tjerkstra: *Acta Metall.*, vol. 9, 1961, pp. 259-263.

143 Y. Bergström and H. Hallèn: *Met. Sci.*, vol. 17, 1983, pp. 341-347.

144 S. Sangal, K.J. Kurzydlowski, and K. Tangri: *Acta Metall.*, vol. 39, 1991, pp. 1281-1288.

145 G.W. Greenwood and A.G. Quarell: *J. Inst. Met.*, vol. 82, 1953-1954, pp. 551-560.

146 A.W. Thompson and M.I. Baskes: *Phil. Mag.*, vol. 28, 1973, pp. 301-308.

147 J.C.M. Li: *Trans. AIME*, vol. 227, 1963, pp. 239-247.

148 A.W. Thompson, M.I. Baskes, and W.F. Flanagan: *Acta. Metall.*, vol. 21, 1973, pp. 1017-1028.

149 H. Margolin and M.S. Stanescu: *Acta Metall.*, vol. 23, 1975, pp. 1411-1418.

150 J.D. Embury, A.S. Keh, and R.M. Fisher: *Trans. AIME*, vol. 236, 1966, pp. 1252-1260.

151 H. Fujita and T. Tabata: *Acta Metall.*, vol. 21, 1973, pp. 355-365.

152 C.M. Young and O.D. Sherby: *J. Iron Steel Inst.*, vol. 211, 1973, pp. 640-647.

153 N. Hansen: *Metall. Trans. A*, vol. 16, 1985, pp. 2167-2190.

154 A.W. Thompson: *Acta Metall.*, vol. 25, 1977, pp. 83-86.

155 K.J. Kurzydlowski: *Scripta Metall. Mater.*, vol. 24, 1990, pp. 879-883.

156 J.J. Bucki and K.J. Kurzydlowski: *Mater. Charac.*, vol. 29, 1992, pp. 375-380.

157 K.J. Kurzydlowski and J.J. Bucki: *Acta Metall. Mater.*, vol. 41, 1993, pp. 3141-3146.

158 F.N. Rhines and B.P. Patterson: *Metall. Trans. A*, vol. 13, 1982, pp. 985-993.

159 J.J. Bucki and K.J. Kurzydlowski: *Mater. Charac.*, vol. 29, 1992, pp. 365-374.

160 K. Okazaki and H. Conrad: *Metall. Trans.*, vol. 3, 1972, pp. 2411-2421.

161 H. Conrad, M. Swintowski, and S.L. Mannan: *Metall. Trans. A*, vol. 16, 1985, pp. 703-708.

162 *Forming Limit Diagrams: Concepts, Methods and Applications*, R.H. Wagoner, K.S. Chan, and S.P. Keeler, eds., TMS-AIME, Warrendale, 1989.

163 R.H. Wagoner and J.V. Laukonis: *Metall. Trans. A*, vol. 14, 1983, pp. 1487-1495.

164 J.H. Schmitt, E. Aernoudt, and B. Baudelet: *Mater. Sci. and Eng.*, vol. 75, 1985, pp. 13-20.

165 J.L. Raphanel and J.H. Schmitt: *Inter. J. of Plasticity*, vol. 2, 1986, pp. 371-378.

166 J.L. Raphanel, E. Rauch, E.L. Shen, and J.H. Schmitt: *Scripta Metall.*, vol. 21, 1987, pp. 1087-1090.

167 A. Korbel and P. Martin: *Acta Metall.*, vol. 36, 1988, pp. 2575-2586.

168 J.J. Gracio: *Mater. Sci. and Eng. A*, vol. 174, 1994, pp. 111-117.

169 A.B. Doucet and R.H. Wagoner: *Metall. Trans. A*, vol. 18, 1987, pp. 2129-2134.

170 A.B. Doucet and R.H. Wagoner: *Metall. Trans. A*, vol. 20, 1989, pp. 1483-1493.

171 A.B. Doucet and S. Natarajan: *Metall. Trans. A*, vol. 22, 1991, pp. 393-401.

172 D.J. Lloyd and H. Sang: *Metall. Trans. A*, vol. 10, 1979, pp. 1767-1772.

173 J.V. Laukonis: *Metall. Trans. A*, vol. 12, 1981, pp. 467-472.

174 R.H. Wagoner and J.V. Laukonis: *Metall. Trans. A*, vol. 14, 1983, pp. 1487-1495.

175 A. Korbel and P. Martin: *Acta Metall.*, vol. 34, 1986, pp. 1905-1909.

176 A. Korbel and P. Martin: *Acta Metall.*, vol. 36, 1988, pp. 2575-2586.

177 E.F. Rauch and C. G'Sell: *Mater. Sci. and Eng. A*, vol. 111, 1989, pp. 71-80.

178 E.F. Rauch and J.H. Schmitt: *Mater. Sci. and Eng. A*, vol. 113, 1989, pp. 441-448.

179 P.L. Charpentier and H.R. Piehler: *Metall. Trans. A*, vol. 15, 1984, pp. 1699-1710.

180 N. Christodoulou, O.T. Woo, and S.R. MacEwen: *Acta Metall.*, vol. 34, 1986, pp. 1553-1562.

181 Y. Strauven and E. Aernoudt: *Acta Metall.*, vol. 35, 1987, pp. 1029-1036.

182 J.L. Raphanel, E.F. Rauch, E.L. Shen, and J.H. Schmitt: *Scripta Metall.*, vol. 21, 1987, pp. 1087-1090.

183 A. Korbel and P. Martin: *Acta Metall.*, vol. 36, 1988, pp. 2575-2586.

184 E.F. Rauch and C. G'Sell: *Mater. Sci. and Eng. A*, vol. 111, 1989, pp. 71-80.

185 A.S. Keh: Phil. Mag., vol. 12, 1965, pp. 9-30.

186 T. Hasegawa and T. Yakou: *Scripta Metall.*, vol. 8, 1974, pp. 951-954.

187 T. Hasegawa, T. Yakou, and S. Karashima: *Mater. Sci. and Eng.*, vol. 20, 1975, pp. 267-276.

188 U.F. Kocks, T. Hasegawa, R.O. Scattergood: *Scripta Metall.*, vol. 14, 1980, pp. 449-454.

189 T. Hasegawa and T. Yakou: *Scripta Metall.*, vol. 14, 1980, pp. 1083-1087.

190 B.V.N. Rao and J.V. Laukonis: *Mater. Sci. and Eng.*, vol. 60, 1983, pp. 125-135.

191 J.V. Fernandes and J.H. Schmitt: *Phil. Mag. A*, vol. 48, 1983, pp. 841-870.

192 T. Hasegawa, T. Yakou, and U.F. Kocks: *Mater. Sci. and Eng.*, vol. 81, 1986, pp. 189-199.

193 J.H. Schmitt, J.V. Fernandes, J.J. Gracio and M.F. Vieira: *Mater. Sci. and Eng. A*, vol. 147, 1991, pp. 143-157.

194 J.V. Fernandes, J.J. Gracio, J.H. Schmitt, and E.F. Rauch: *Scripta Metall. Mater.*, vol. 28, 1993, pp. 1335-1340.

195 E.F. Rauch: *Solid State Phenon.*, vol. 23-24, 1992, pp. 317-334.

196 S.A. Vincent: *Master's Thesis*, University of California, Berkeley, 1987.

197 P.E. Johnson, J.H. Schmitt, S.A. Vincent, and J.W. Morris, Jr.: *Scripta Metall.*, vol. 24, 1990, pp. 1447-1452.

198 P.E. Johnson: *PhD Thesis*, University of California, Berkeley, 1991.

199 H. Mughrabi: *Acta Metall.*, vol. 31, 1983, pp. 1367-1379.

200 *ASTM Standards*, vol. 3, no. 1, Designation E112-88.

201 T. Hasegawa and U.F. Kocks: *Acta Metall.*, vol. 27, 1979, pp. 1705-1716.

202 P.S. Bate: *Metall. Trans. A*, vol. 24, 1993, pp. 2679-2689.

203 P.S. Bate: *Metall. Trans. A*, vol. 24, 1993, pp. 2691-2699.

204 G.Y. Chin: in *Work Hardening in Tension and Fatigue*, A.W. Thompson, ed., TMS-AIME, 1977, pp. 45-66.

205: D. Yao, D. Chu, and J.W. Morris, Jr.: in *Light-Weight Alloys for Aerospace Applications II*, E.W. Lee and N.J. Kim, eds., TMS-AIME, Warrendale, 1991, pp. 99-105.

206 N.J. Kim and E.W. Lee: *Aluminum-Lithium V*, T.H. Sanders, Jr. and E.A. Starke, Jr., eds., Materials and Component Engineering Publications, Ltd., Birmingham, 1989, pp. 809-816.

207 N.J. Kim and E.W. Lee: *Acta Metall.*, vol. 41, 1993, pp. 941-948.

208 J.C.M. Li: *Acta. Metall.*, vol. 8, 1960, pp. 563-574.

Microstructure	Annealing Temperature °C
Unrecrystallized (URX)	---
Recovered (REC)	225
Partially Recrystallized (PRX)	290
Recrystallized (110 μm) (REX)	365
Recrystallized (185 μm)	410

Table I: Temperatures used for annealing treatments. All specimens were held at specified temperature for 3 hours followed by a furnace cool.

Microstructure	Yield Strength MPa (ksi)	Ultimate Strength MPa (ksi)	Uniform Elongation %*	Total Elongation %*†
Unrecrystallized (URX)	142 (20.5)	196 (28.4)	26.4	46
Recovered (REC)	113 (16.4)	185 (26.8)	34.8	56
Partially Recrystallized (PRX)	65 (9.4)	171 (24.8)	33.9	47
Recrystallized (110 μm) (REX)	13 (1.9)	139 (20.2)	31.7	47
Recrystallized (185 μm)	12 (1.7)	129 (18.7)	32.0	48

* *Values obtained from initial gauge length of 25 mm (1.00 in.).*

† *Estimated values based on measurements of gauge length after failure. Accuracy of measurements is ±2%.*

Table II: Engineering tensile properties of KSL specimens (99.94% aluminum) in various annealing conditions.

	Early Deformation Regime			Latter Deformation Regime		
Microstructure	Θ_o (MPa)*	$\sigma_s = \frac{\Theta_o}{K_2}$ (MPa)*†	K_2*	Θ_o (MPa)*	$\sigma_s = \frac{\Theta_o}{K_2}$ (MPa)*†	K_2*
Unrecrystallized	3215	222	14.5	1110	317	3.50
Recovered	2310	208	11.1	1120	320	3.50
Partially Recrystallized	2195	188	11.7	1520	265	5.73
Recrystallized (110 μm)	1875	155	12.1	1720	201	8.55

* *Scatter in data is approximately ±5%.*

† *Stress at zero work hardening rate.*

Table III: Work hardening parameters for KSL specimens according to the Kocks-Mecking model (Equation (20)).

Microstructure	Initial Work Hardening Rate θ_o/G (±0.005)	$\frac{\theta_o/G}{0.06} = \frac{M^2}{3.06^2}$	Taylor Factor M
Kocks' results	0.06	1.00	3.06
Recrystallized (REX)	0.065	1.08	3.18
Partially Recrystallized (PRX)	0.055	0.92	2.93
Recovered & Unrecrystallized (REC & URX)	0.041	0.68	2.53

Table IV: Calculated Taylor factors for the microstructures tested in this work assuming only texture effects.

Microstructure & Orientation*	Yield Strength MPa (ksi)	Ultimate Strength MPa (ksi)	Uniform Elongation %†	Total Elongation %†‡
Recrystallized 0°	7.1 (1.0)	128 (18.6)	43.8	58
Recrystallized 45°	7.5 (1.1)	136 (19.8)	41.2	57
Unrecrystallized 0°	104 (15.1)	150 (21.8)	29.9	43
Unrecrystallized 90°	113 (16.4)	151 (21.9)	25.5	38

* *Orientations given in degrees away from rolling direction.*

† *Values obtained from initial gauge length of 25 mm (1.00 in.).*

‡ *Estimated values based on measurements of gauge length after failure. Accuracy of measurements is ±2%.*

Table V: Engineering tensile properties of LBL1 specimens (99.96% aluminum) in various annealing conditions and orientations.

Microstructure & Orientation*	Yield Strength MPa (ksi)	Ultimate Strength MPa (ksi)	Uniform Elongation %†	Total Elongation %†‡
Unrecrystallized 0°	116 (16.8)	166 (24.0)	29.8	47
Unrecrystallized 45°	114 (16.6)	144 (20.9)	13.6	32
Unrecrystallized 90°	127 (18.4)	147 (21.3)	19.6	37

* *Orientations given in degrees away from rolling direction.*

† *Values obtained from initial gauge length of 25 mm (1.00 in.).*

‡ *Estimated values based on measurements of gauge length after failure. Accuracy of measurements is ±2%.*

Table VI: Engineering tensile properties of LBL2 specimens (99.96% aluminum) in various orientations.

	Early Deformation Regime			Latter Deformation Regime		
Batch & Orientation	Θ_o (MPa)*	$\sigma_s = \frac{\Theta_o}{K_2}$ (MPa)*†	K_2*	Θ_o (MPa)*	$\sigma_s = \frac{\Theta_o}{K_2}$ (MPa)*†	K_2*
LBL1 - 0°	1890	178	10.6	745	261	2.85
LBL1 - 90°	2640	169	15.6	820	243	3.38
LBL2 - 0°	2355	185	12.7	835	286	2.92
LBL2 - 45°	2210	163	13.6	-	-	-
LBL2 - 90°	2735	167	16.4	865	215	4.03

* *Scatter in data is approximately ±5%.*

† *Stress at zero work hardening rate.*

Table VII: Work hardening parameters for LBL specimens according to the Kocks-Mecking model (Equation (20)).

	Early Deformation Regime			Latter Deformation Regime		
Microstructure	Θ_o (MPa)*	$\sigma_s = \frac{\Theta_o}{K_2}$ (MPa)*†	K_2*	Θ_o (MPa)*	$\sigma_s = \frac{\Theta_o}{K_2}$ (MPa)*†	K_2*
Recovered (REC)	2310	208	11.1	1120	320	3.50
Recrystallized (REX)	1875	155	12.1	1720	201	8.55
Reannealed (REN)	5125	128	39.9	915	232	3.95

* *Scatter in data is approximately ±5%.*

† *Stress at zero work hardening rate.*

Table VIII: Work hardening parameters for LBL specimens according to the Kocks-Mecking model (Equation (20)). Reannealing of the recrystallized microstructure causes K_2 of the latter regime to decrease to a value approaching the value obtained for the recovered microstructure.

Microstructure	Yield Strength MPa (ksi)	Ultimate Strength MPa (ksi)	Uniform Elongation %*	Total Elongation %*†
Recrystallized	13 (1.9)	139 (20.2)	31.7	47
Pre-Compressed Recrystallized	39 (5.6)	139 (20.1)	33.8	52

* *Values obtained from initial gauge length of 25 mm (1.00 in.).*

† *Estimated values based on measurements of gauge length after failure. Accuracy of measurements is ±2%.*

Table IX: Engineering tensile properties of KSL specimens (99.94% aluminum) in various annealing conditions.

	Early Deformation Regime			Latter Deformation Regime		
Microstructure	Θ_0 (MPa)*	$\sigma_s = \frac{\Theta_0}{K_2}$ (MPa)*†	K_2*	Θ_0 (MPa)*	$\sigma_s = \frac{\Theta_0}{K_2}$ (MPa)*†	K_2*
Recrystallized	1875	155	12.1	1720	201	8.55
Pre-Compressed Recrystallized	2220	117	19.0	1565	192	8.16

* *Scatter in data is approximately ±5%.*

† *Stress at zero work hardening rate.*

Table X: Work hardening parameters for recrystallized and pre-compressed recrystallized microstructures according to the Kocks-Mecking model (Equation (20)). Pre-compression produces an early regime with a higher slope. The slope of the latter regime remains unchanged.

Microstructure	Yield Strength MPa (ksi)	Ultimate Strength MPa (ksi)	Uniform Elongation %*	Total Elongation %*†
Recovered	113 (16.4)	185 (26.8)	34.8	56
Pre-Compressed Recovered	115 (16.7)	186 (27.0)	35.8	50

* *Values obtained from initial gauge length of 25 mm (1.00 in.).*

† *Estimated values based on measurements of gauge length after failure. Accuracy of measurements is ±2%.*

Table XI: Engineering tensile properties of KSL specimens (99.94% aluminum) in various annealing conditions.

	Early Deformation Regime			Latter Deformation Regime		
Microstructure	Θ_o (MPa)*	$\sigma_s = \frac{\Theta_o}{K_2}$ (MPa)*†	K_2*	Θ_o (MPa)*	$\sigma_s = \frac{\Theta_o}{K_2}$ (MPa)*†	K_2*
Recovered	2310	208	11.1	1120	320	3.50
Pre-Compressed Recovered	2085	217	9.61	1040	334	3.11

* *Scatter in data is approximately ±5%.*

† *Stress at zero work hardening rate.*

Table XII: Work hardening parameters for recrystallized and pre-compressed recrystallized microstructures according to the Kocks-Mecking model (Equation (20)). Pre-compression produces an early regime with a higher slope. The slope of the latter regime remains unchanged.

Microstructure	Θ_0 (MPa)*	$\sigma_s = \frac{\Theta_0}{K_2}$ (MPa)*†	K_2*
Recrystallized (REX)	1720	201	8.55
Recrystallized (Al-2.5Mg) (115 μm)	2430	466	5.21
Recrystallized (Al-5.0Mg) (150 μm)‡	2440~3240	853~604	2.86~5.36
Recovered (REC)	1120	320	3.50

* *Scatter in data is approximately ±5%.*

† *Stress at zero work hardening rate.*

‡ *Second values obtained from approximation at high stresses.*

Table XIII: Work hardening parameters for aluminum-magnesium specimens and pure aluminum specimens in the recrystallized and recovered condition according to the Kocks-Mecking model (Equation (20)). Dimensions in left column indicate grain sizes. Addition of magnesium causes K_2 to decrease to a value approaching the value obtained for the pure aluminum recovered microstructure.

Microstructure	Yield Strength MPa (ksi)	Ultimate Strength MPa (ksi)	Uniform Elongation %*	Total Elongation %*†
Recrystallized (REX) (110 μm)	13 (1.9)	139 (20.2)	31.7	47
Recrystallized (Al-2.5Mg) (115 μm)	62 (9.0)	279 (40.4)	34.3	50
Recrystallized (Al-5.0Mg) (150 μm)	91 (13.3)	363 (52.6)	38.3	49
Recovered (REC)	113 (16.4)	185 (26.8)	34.8	56

* *Values obtained from initial gauge length of 25 mm (1.00 in.).*

† *Estimated values based on measurements of gauge length after failure. Accuracy of measurements is ±2%.*

Table XIV: Engineering tensile properties of aluminum-magnesium specimens and pure aluminum specimens in the recrystallized and recovered condition. Dimensions in left column indicate grain sizes. Addition of magnesium produces an increase in both strength and elongation. Note that the pure aluminum recovered microstructure exhibits the greatest yield strength. However, the higher work hardening rate achieved with the addition of magnesium produces greater ultimate strengths in the magnesium-bearing specimens.

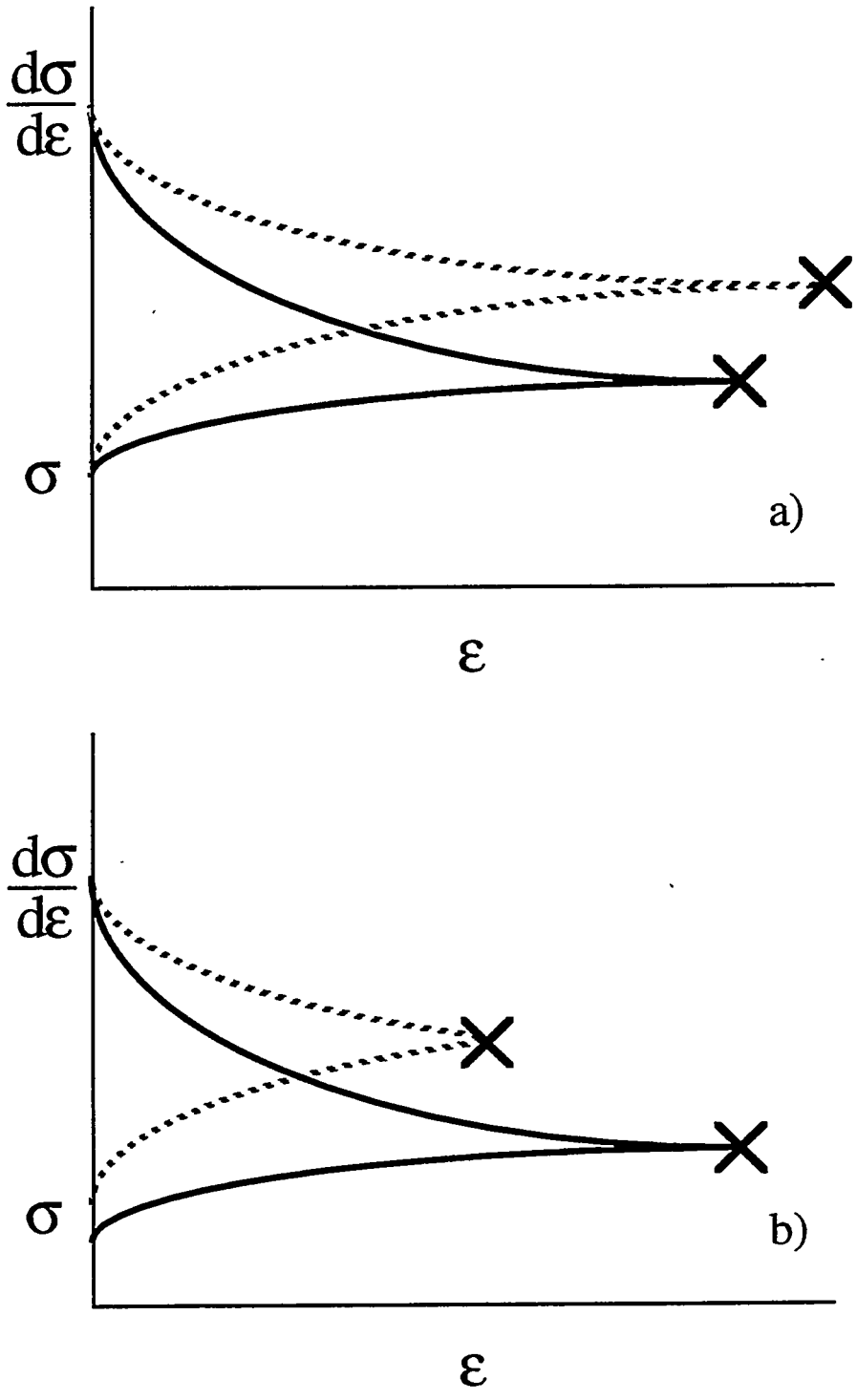

Figure 1: Schematic depicting the dependency of the strain to failure on the flow strength and work hardening rate: a) Dashed lines exhibit increase in the strain to failure resulting from an increase in the work hardening rate; b) Increase in yield strength may counteract this improvement in work hardening, resulting in a decrease in the strain to failure.

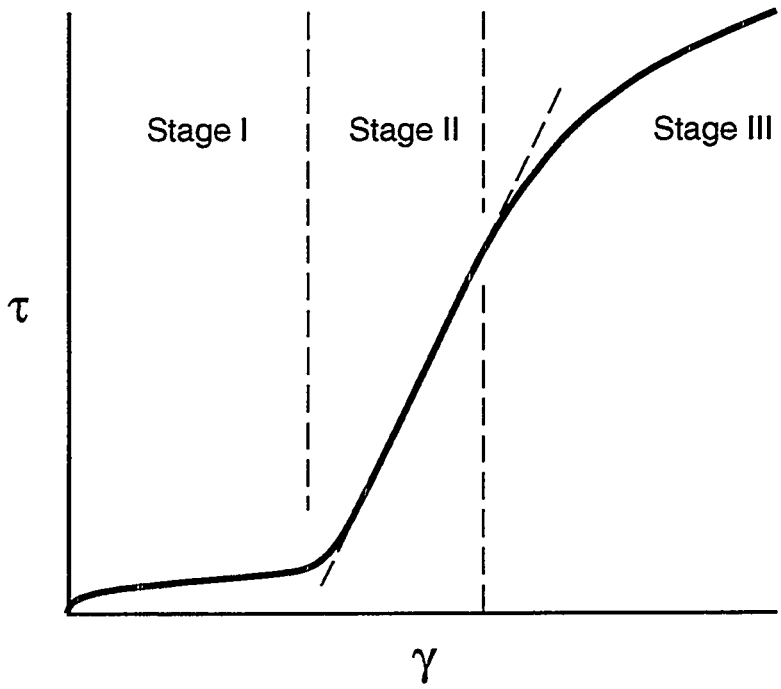

Figure 2: Schematic plot of the stress-strain curve for a single crystal oriented for single slip illustrating the three stages of work hardening.

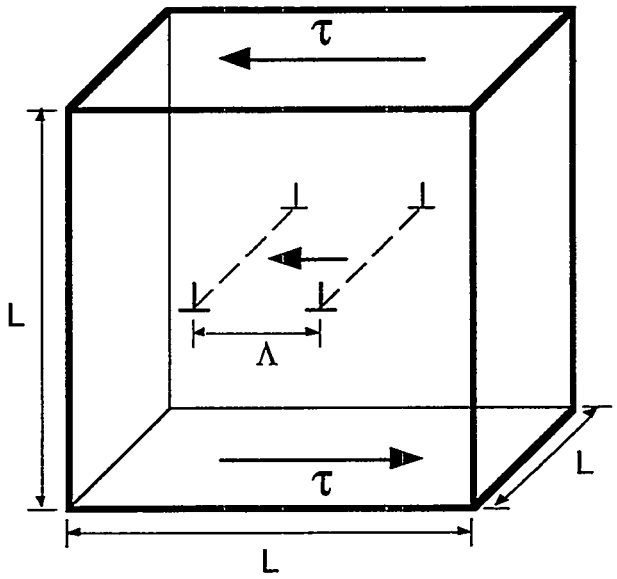

Figure 3: Schematic illustrating the derivation of the dislocation storage rate in Equation (7). The edge dislocation moves a distance Λ through the cube under the applied shear stress τ.

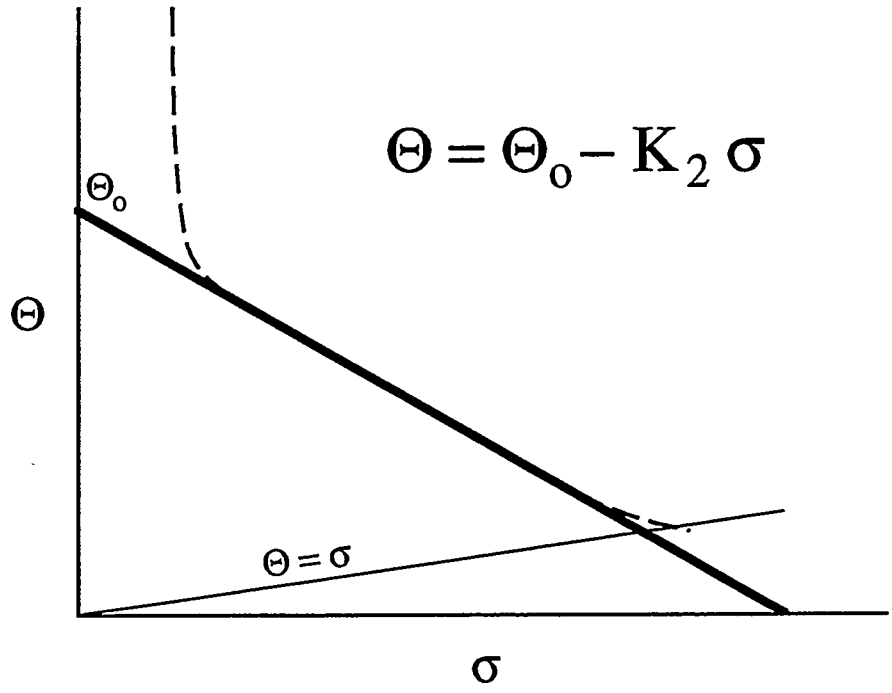

Figure 4: Schematic illustrating the Kocks-Mecking model. Typical work hardening curve obtained from tensile tests is shown by the dashed line.

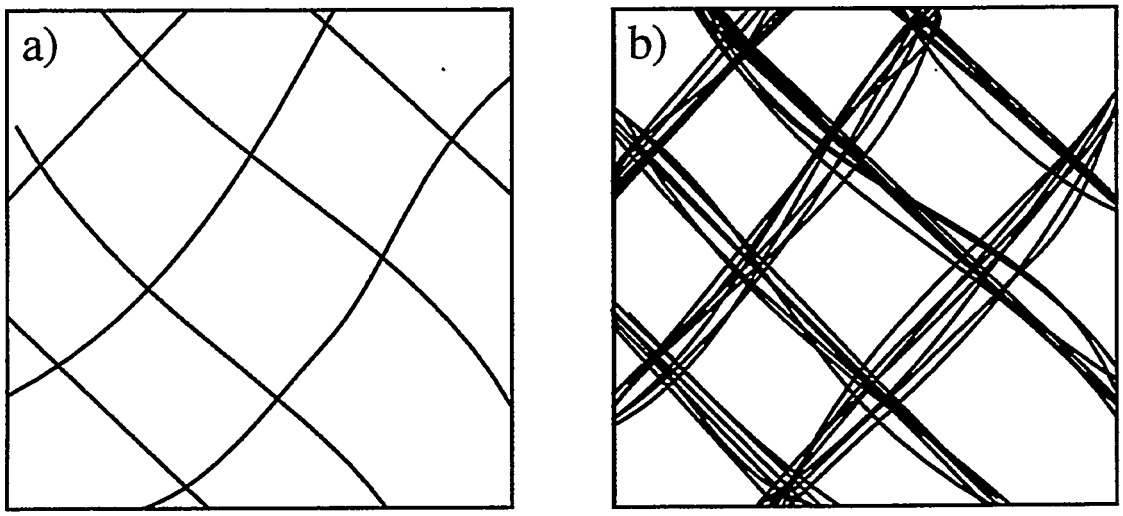

Figure 5: Schematic demonstrating the similarity between the physical description given by the Kocks-Mecking model in a) and the Mesh-Length theory in b). Note that the heterogeneity of the dislocations in the Mesh-Length theory results in a homogeneity in the dislocation tangles.

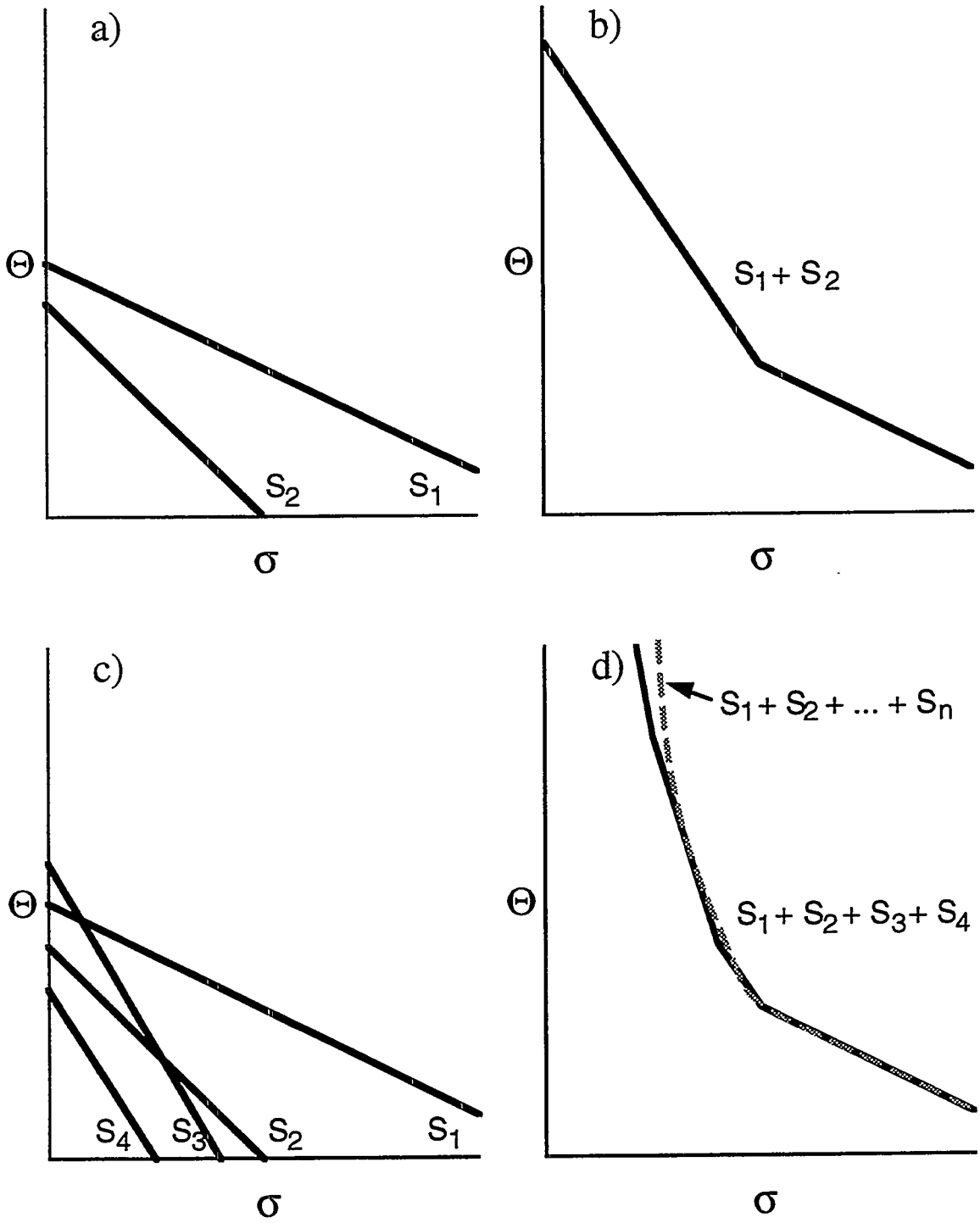

Figure 6: Schematic illustrating a multiple structure parameter model based on the foundation of the Kocks-Mecking model. Figure a) shows the two work hardening curves associated with two different structure parameters. Figure b) shows the bi-linear plot resulting from the addition of the two curves in Figure a). Figures c) and d) show the extension of Figures a) and b) to an n-parameter model as highlighted by the dashed and shaded line in Figure d).

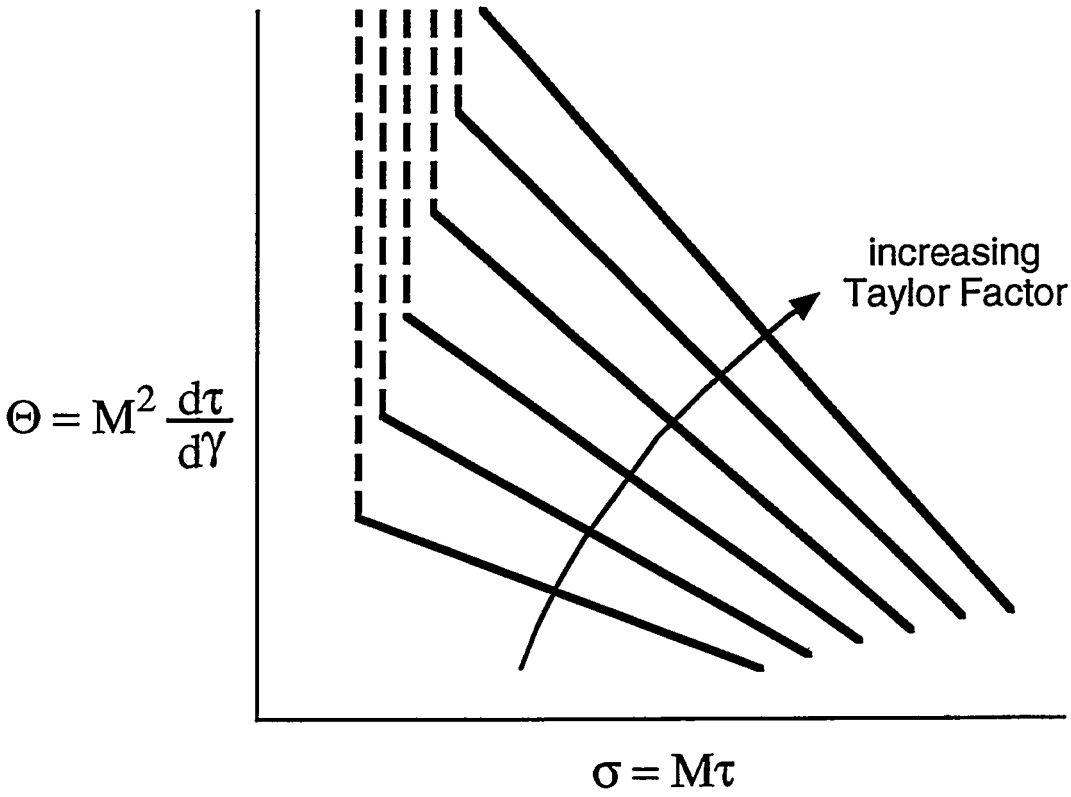

Figure 7: Schematic illustrating the theoretical influence of texture on the work hardening behavior.

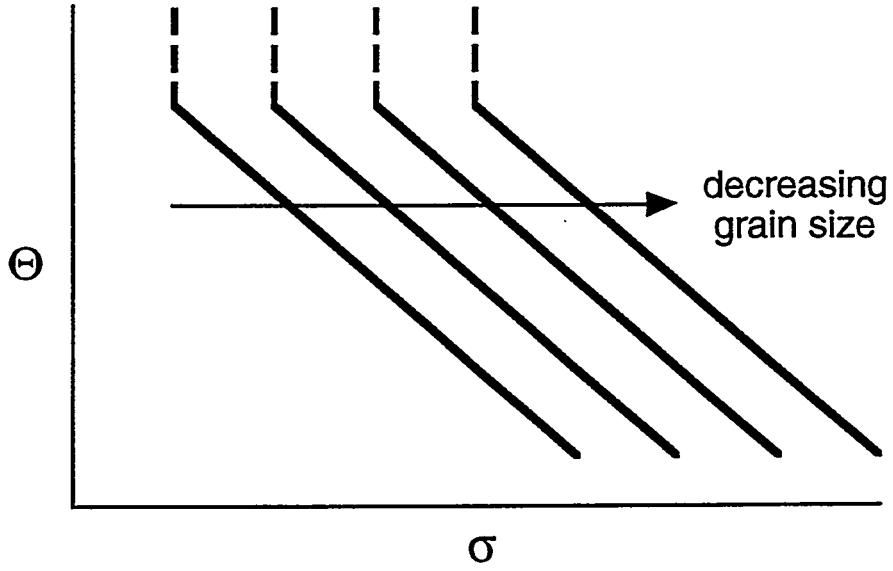

Figure 8: Schematic illustrating the influence of grain size on the work hardening behavior assuming no change in the evolution of the dislocation substructure after yielding.

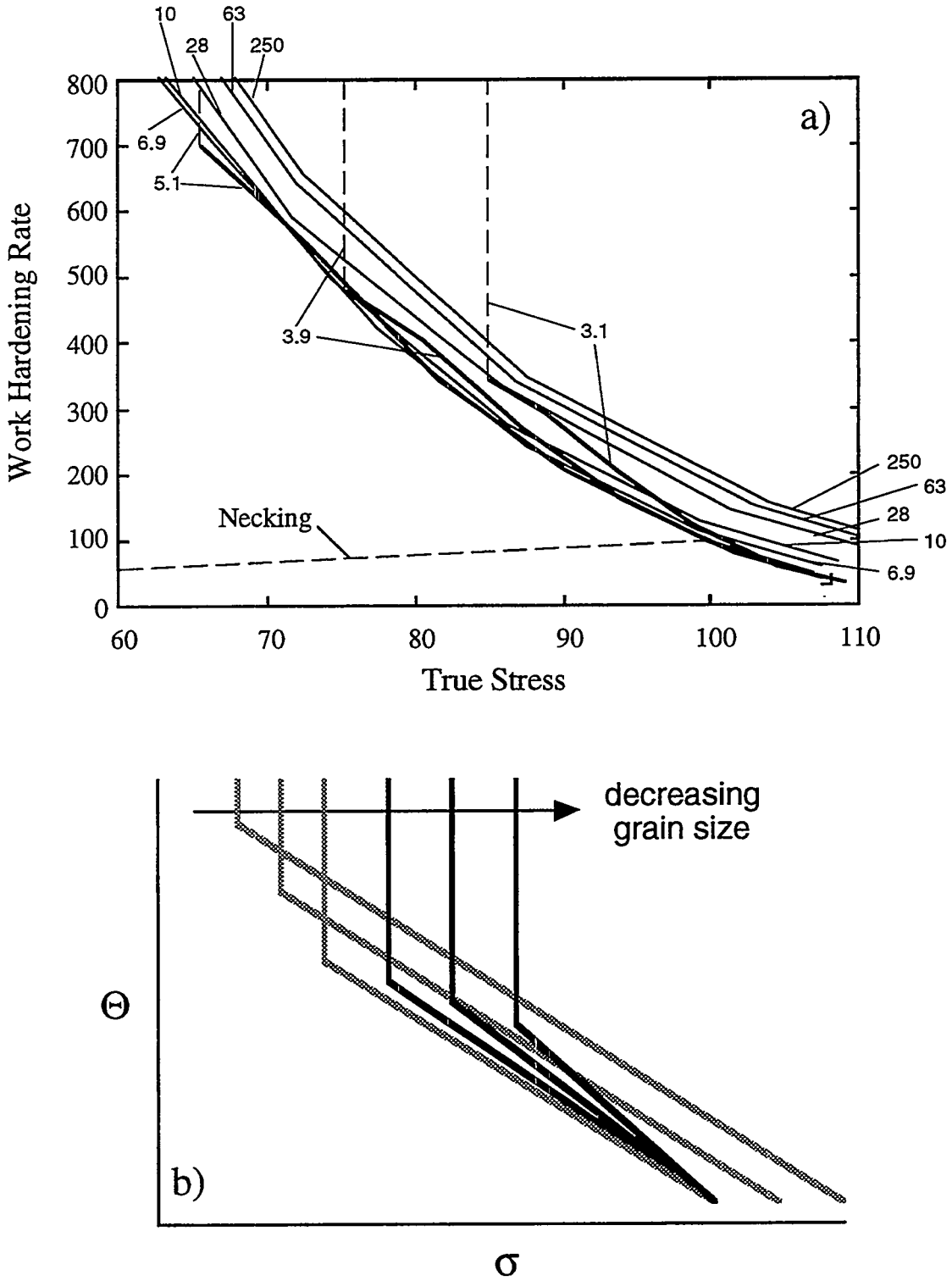

Figure 9: a) Work hardening rate versus true stress plots for aluminum extrapolated from computer generated stress versus grain size (in μm) curves in reference 148, figure 6a. Curves for smaller grain sizes are in bold to emphasize increase in work hardening slope. b) Schematic of extrapolated work hardening versus true stress plot highlighting the trend shown in a).

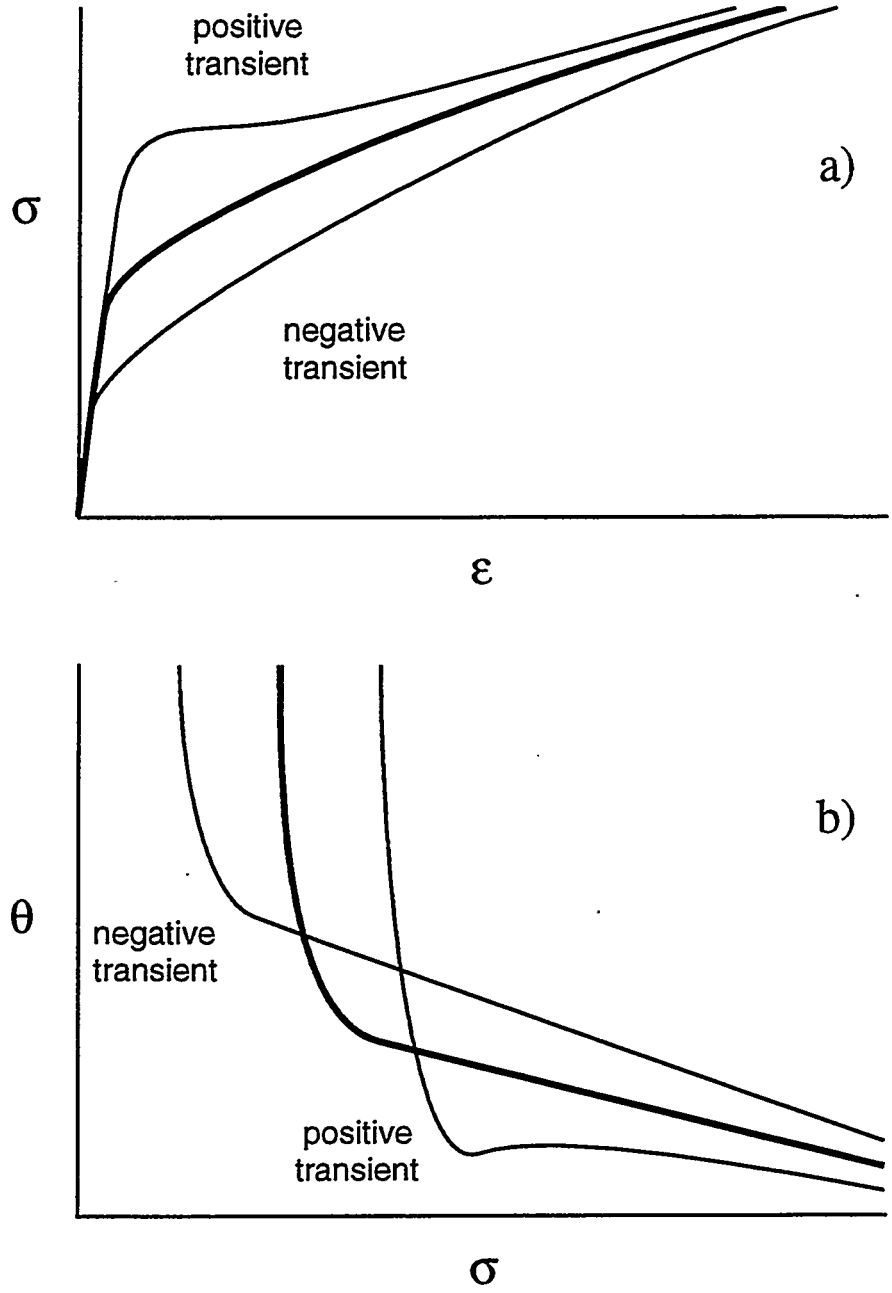

Figure 10: Schematic showing the stress-strain curves a), and corresponding work hardening curves b) for both positive and negative transients. In both a) and b), the bold line represents the curve of the second loading condition without prestraining.

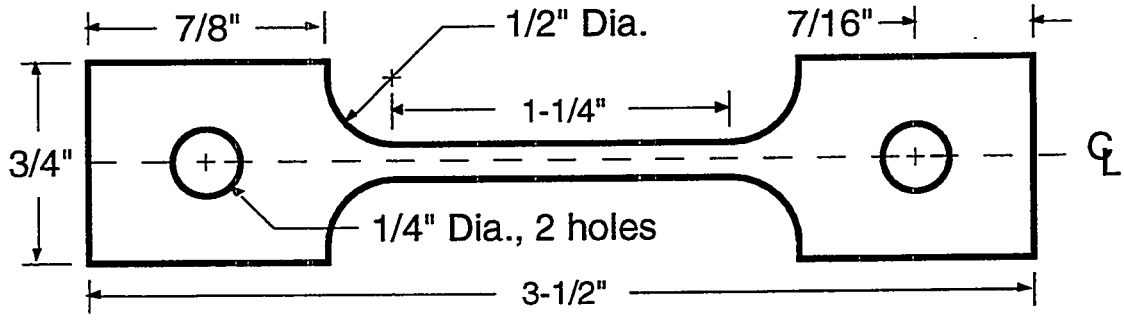

Figure 11: Schematic illustration showing the dimensions of tensile specimens. All dimensions are in inches.

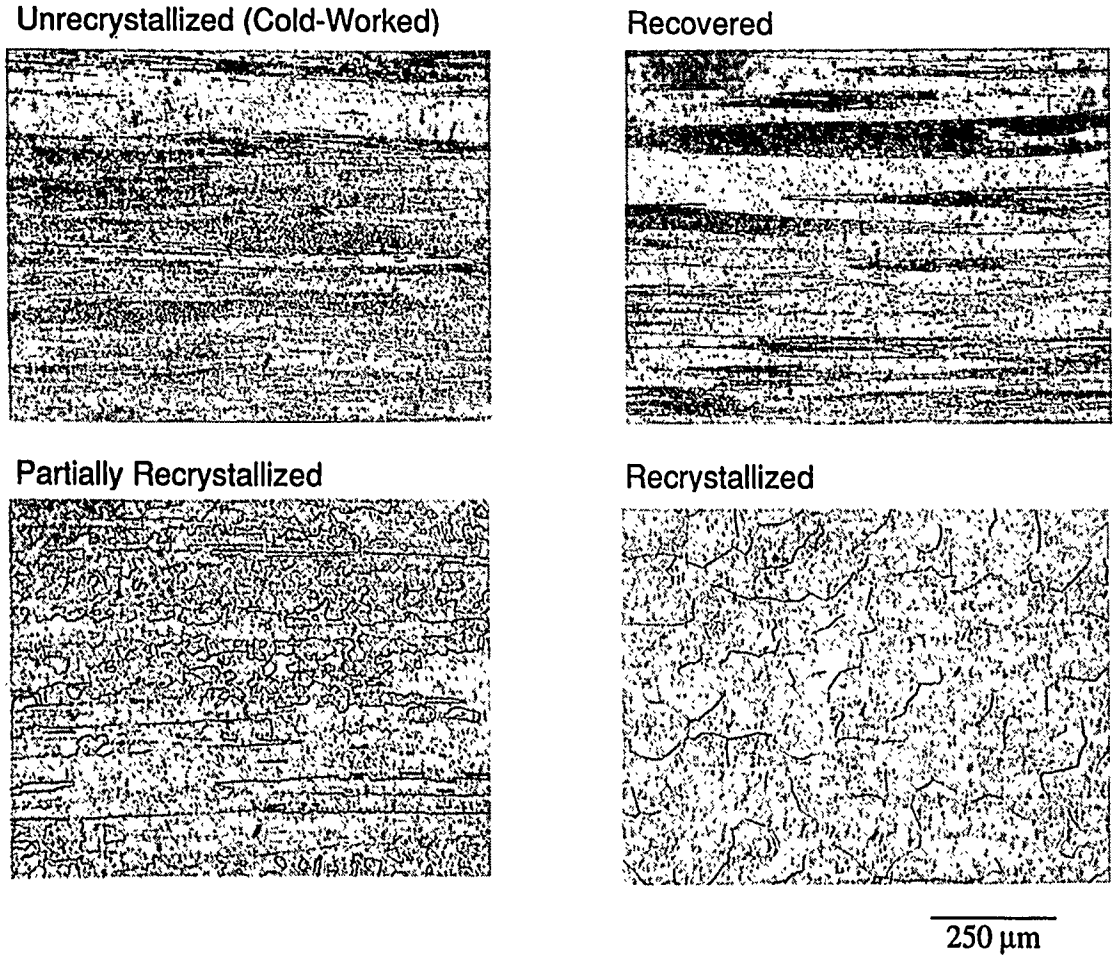

Figure 12: Optical micrographs of the four microstructures tested in this study. (XBB 9310-6739)

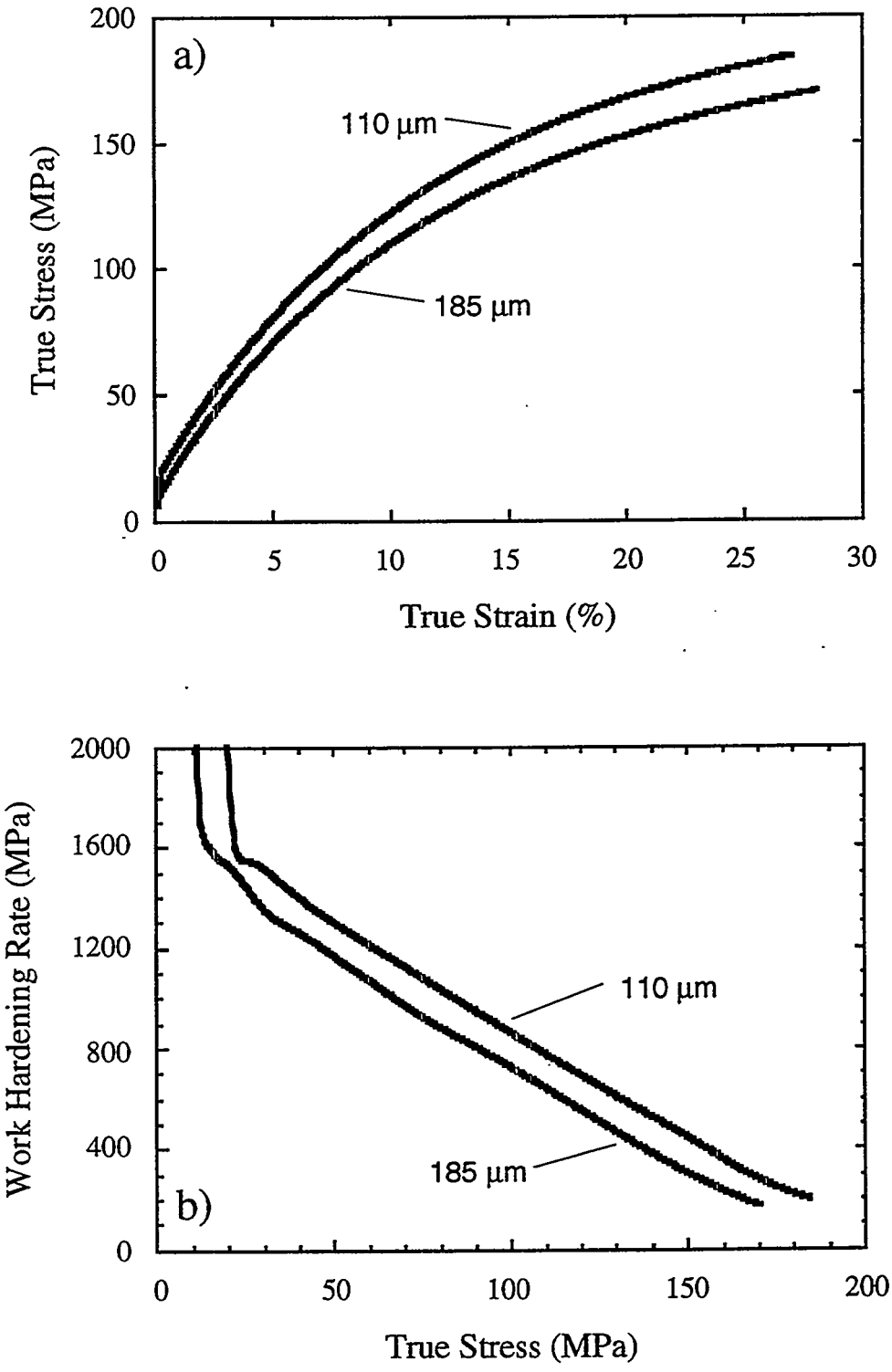

Figure 13: Stress-strain curves and work hardening curves for the two recrystallized specimens. Slight increase in flow stress difference with increasing strain in a) indicates increasing Hall-Petch slope with strain. This increase, however, does not significantly affect the slope of the work hardening curve. Compare b) with Figures 8 and 9.

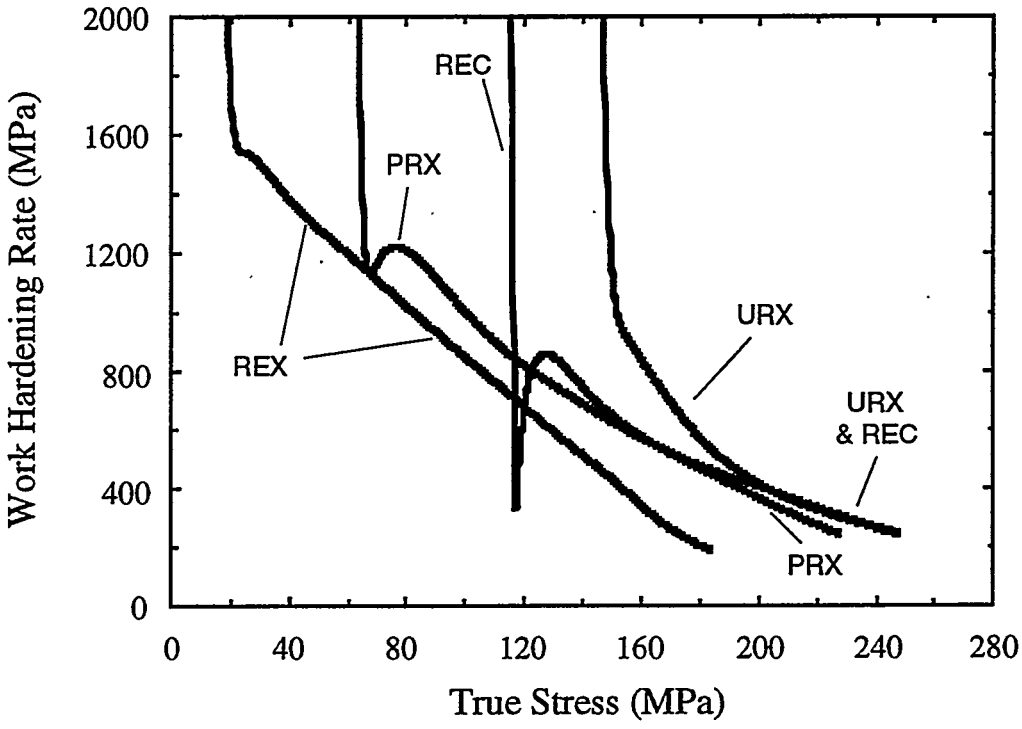

Figure 14: Plot of the work hardening rate versus true stress for the four microstructures: unrecrystallized (URX), recovered (REC), partially recrystallized (PRX), and recrystallized (REX). Both the unrecrystallized and recovered microstructures exhibit the same work hardening behavior after approximately 200 MPa.

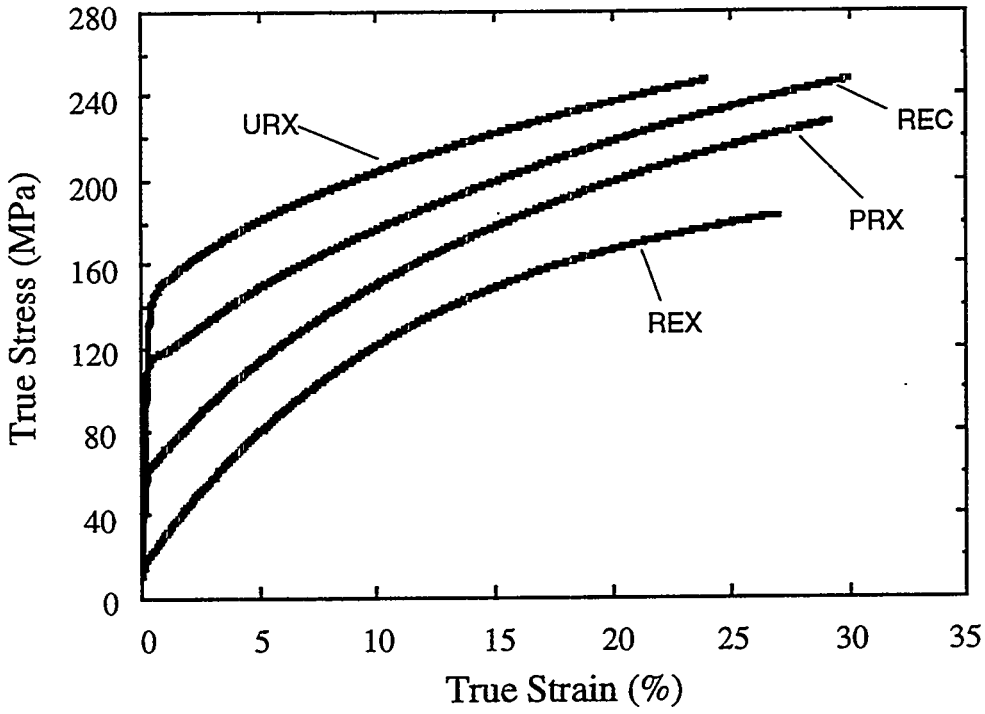

Figure 15: Stress-strain curves for the four microstructures: unrecrystallized (URX), recovered (REC), partially recrystallized (PRX), and recrystallized (REX). Both unrecrystallized and recovered specimens achieve the strength level, approximately 250 MPa, despite the large difference in elongation. The partially recrystallized microstructure appears to parallel the recrystallized microstructure at low strains and the recovered microstructure at high strains.

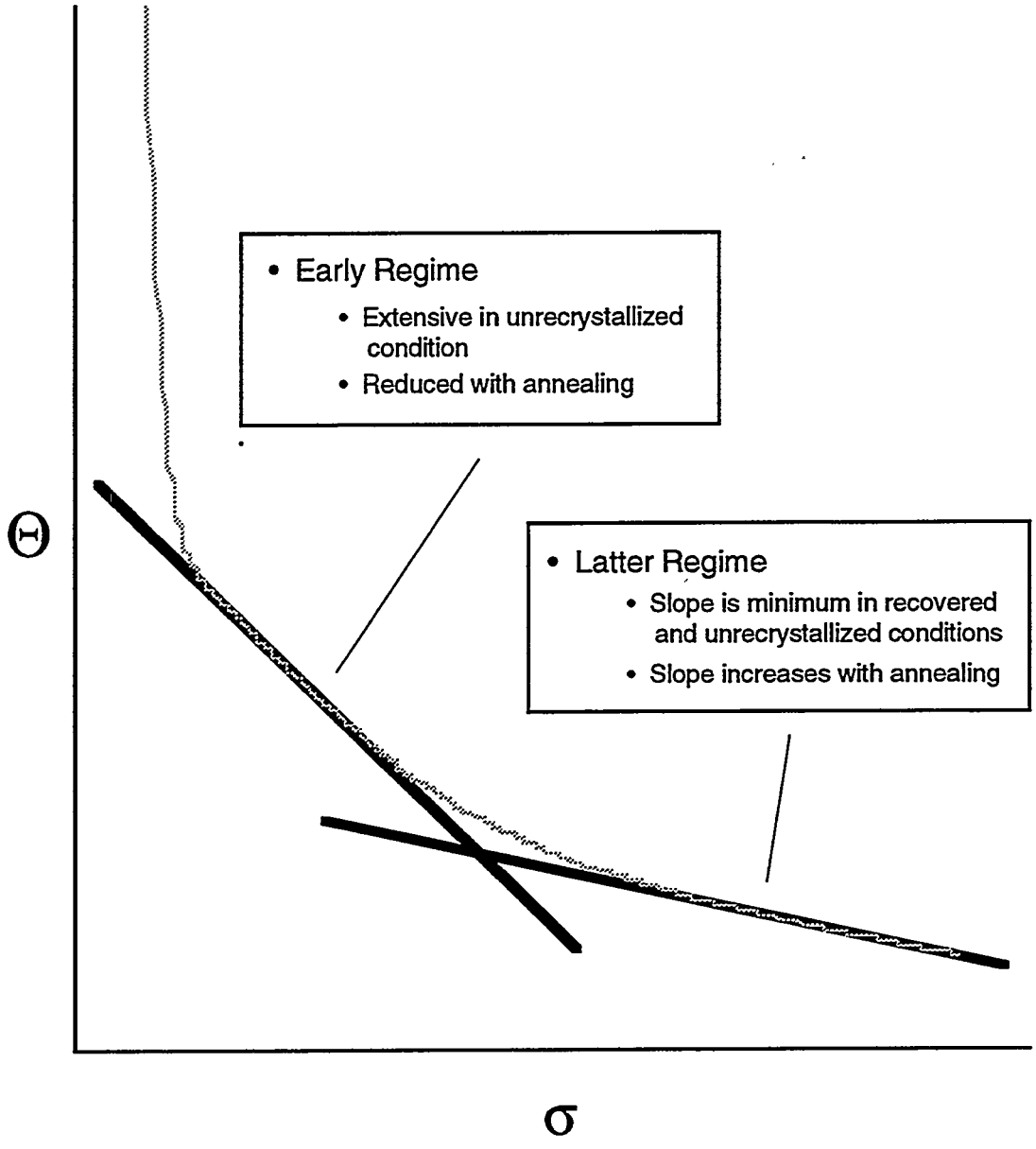

Figure 16: Schematic illustrating the results from the work hardening analysis on the four microstructures shown in Figure 14. The work hardening curve for the unrecrystallized microstructure is shown by the shaded line.

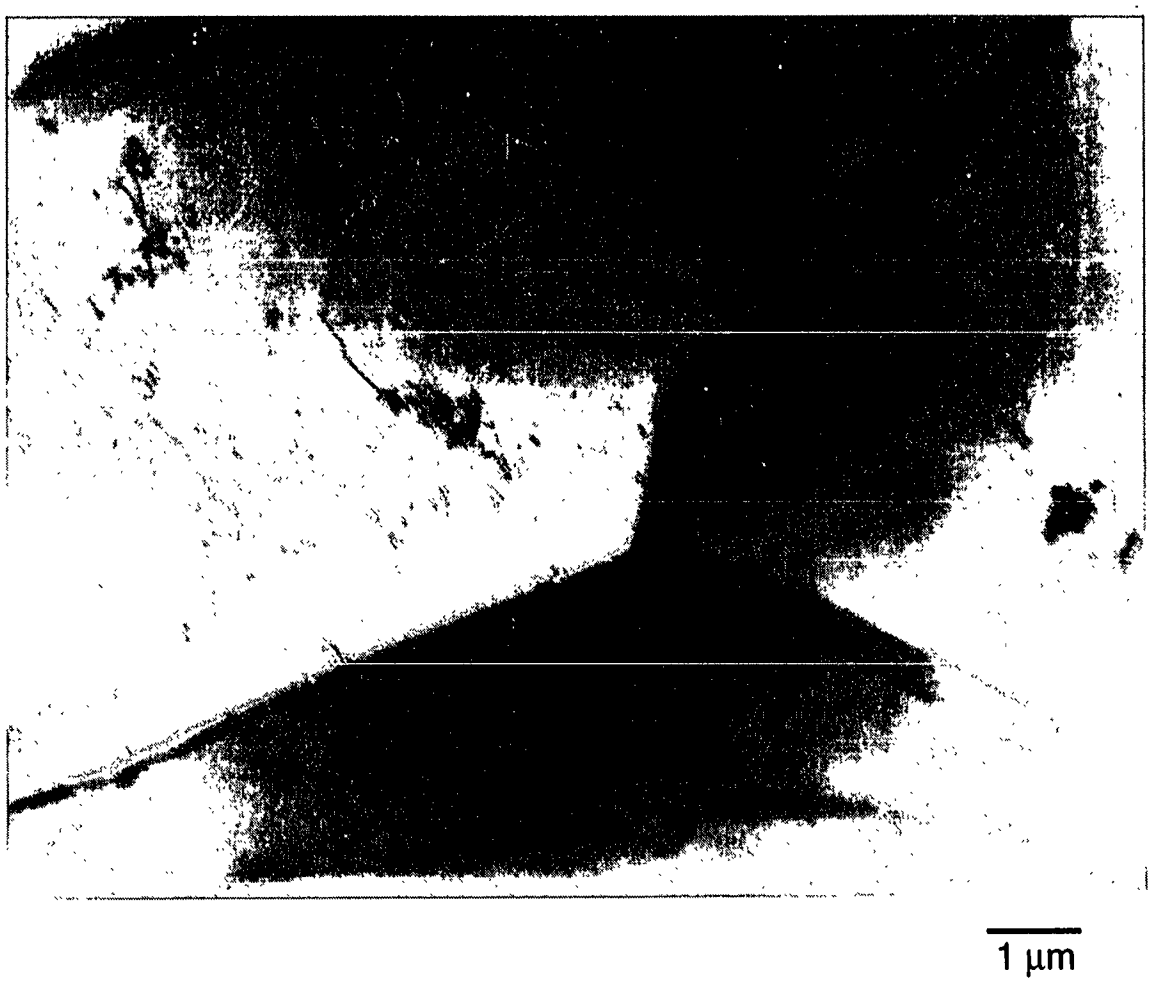

Figure 17: TEM micrograph highlighting a triple point grain boundary of the recrystallized microstructure prior to deformation. Except for the few artifacts left from the electropolishing and sample preparation, the microstructure is relatively absent of any internal structure. Zone axis is near [0$\bar{1}$1]. (XBB 9408-5013)

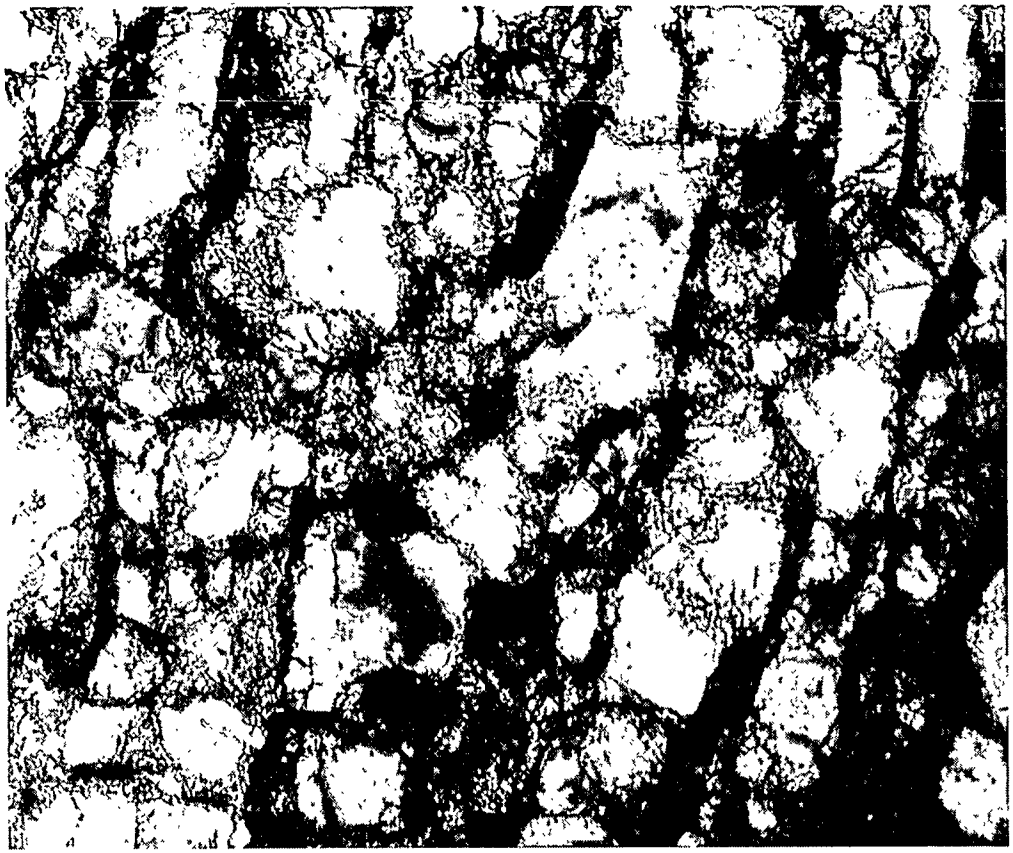

Figure 18: TEM micrograph of the recrystallized microstructure after deformation to a true stress of 178 MPa (25.8 ksi), approximately 26.8% true strain. Note the strong formation of a cellular dislocation structure. Zone axis is $[0\bar{1}1]$. (XBB 9408-5000)

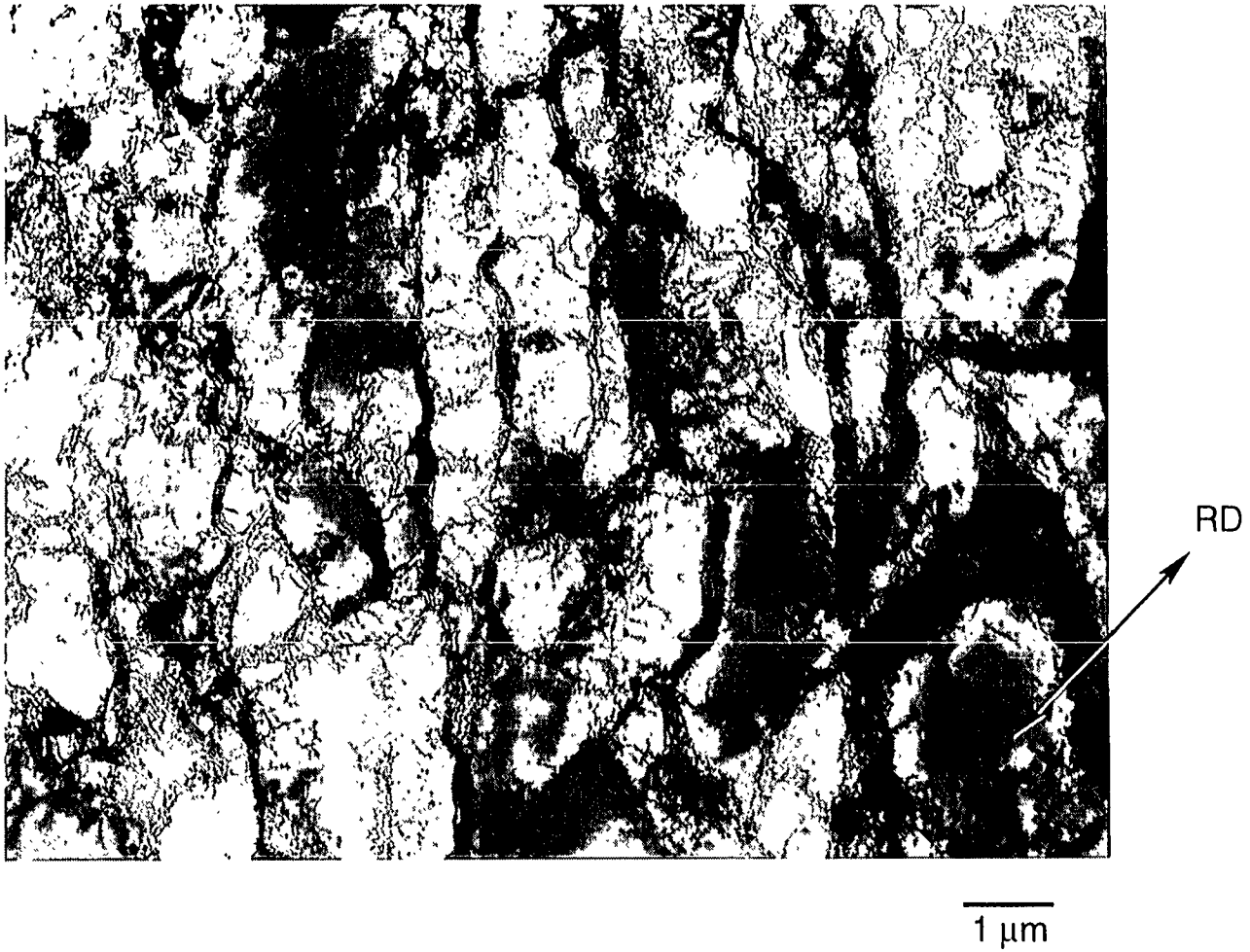

Figure 19: TEM micrograph of the recrystallized microstructure after deformation to a true stress of 178 MPa (25.8 ksi), approximately 26.8% true strain. Note that the cell structure is elongated approximately 45° from the loading direction which is parallel to the initial rolling direction. Zone axis is near [0$\bar{1}$1]. (XBB 9408-5001)

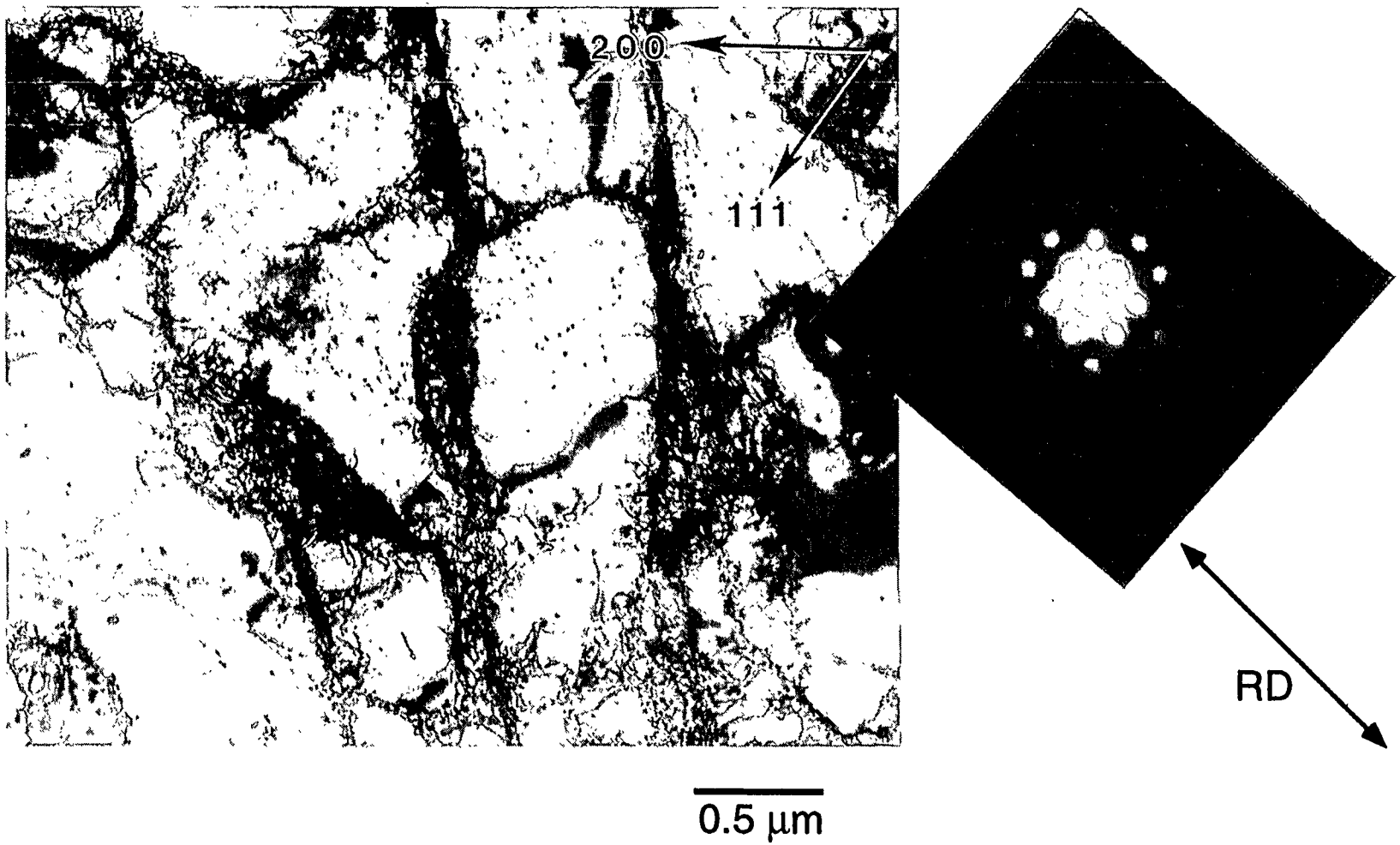

Figure 20: TEM micrograph of the recrystallized microstructure after deformation to a true stress of 168 MPa (24.4 ksi), approximately 22.3% true strain. Micrograph shows that the dislocation cell walls lie parallel to the (111) and (200) planes. Zone axis is [0$\bar{1}$1]. (XBD 9408-5006)

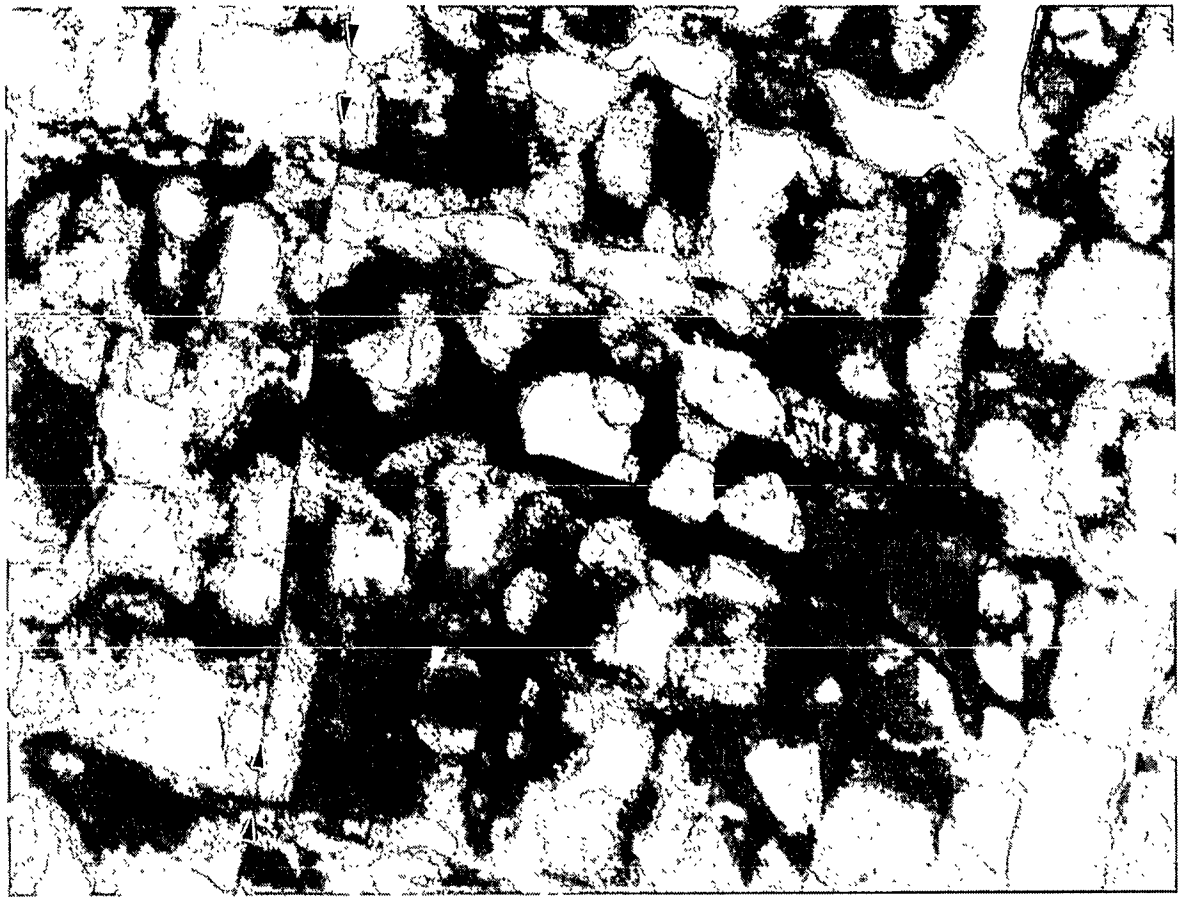

Figure 21: TEM micrograph of the recrystallized microstructure after deformation to a true stress of 178 MPa (25.8 ksi), approximately 26.8% true strain. Micrograph shows an extreme case in which the cellular structure is relatively symmetrical in configuration. Note the sharpness of the grain boundary (marked by arrows) suggesting the lack of grain boundary influence on the deformation process and evolution of the dislocation cell structure. Zone axis is [011]. (XBD 9408-5002)

Figure 22: TEM micrograph of the recovered microstructure prior to deformation. Note the well developed subgrain morphology in contrast to the recrystallized microstructure in Figure 17. Zone axis is near [011]. (XBB 9408-4997)

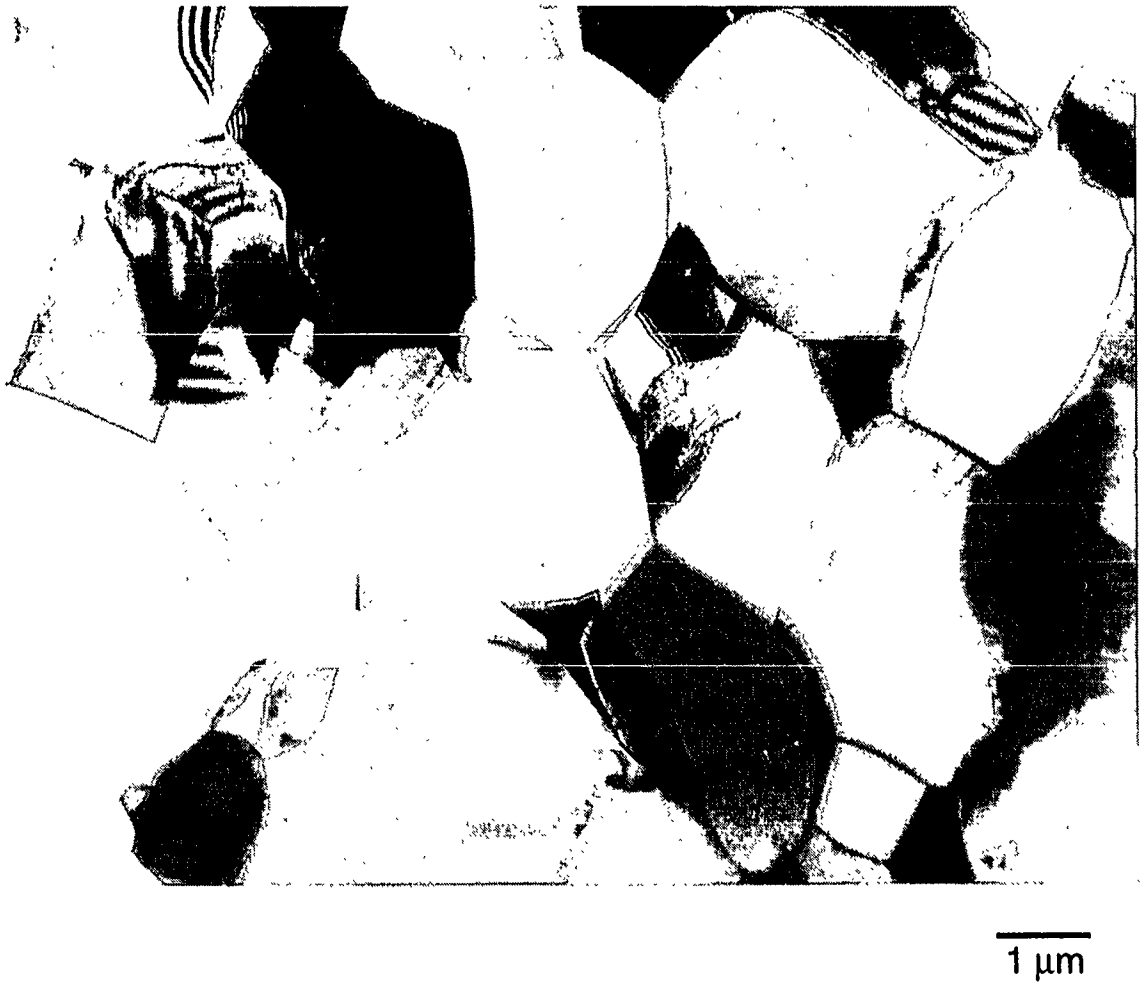

Figure 23: TEM micrograph of the recovered microstructure prior to deformation. Note the well developed subgrain morphology in contrast to the recrystallized microstructure in Figure 17. Zone axis is near [011]. (XBB 9408-4996)

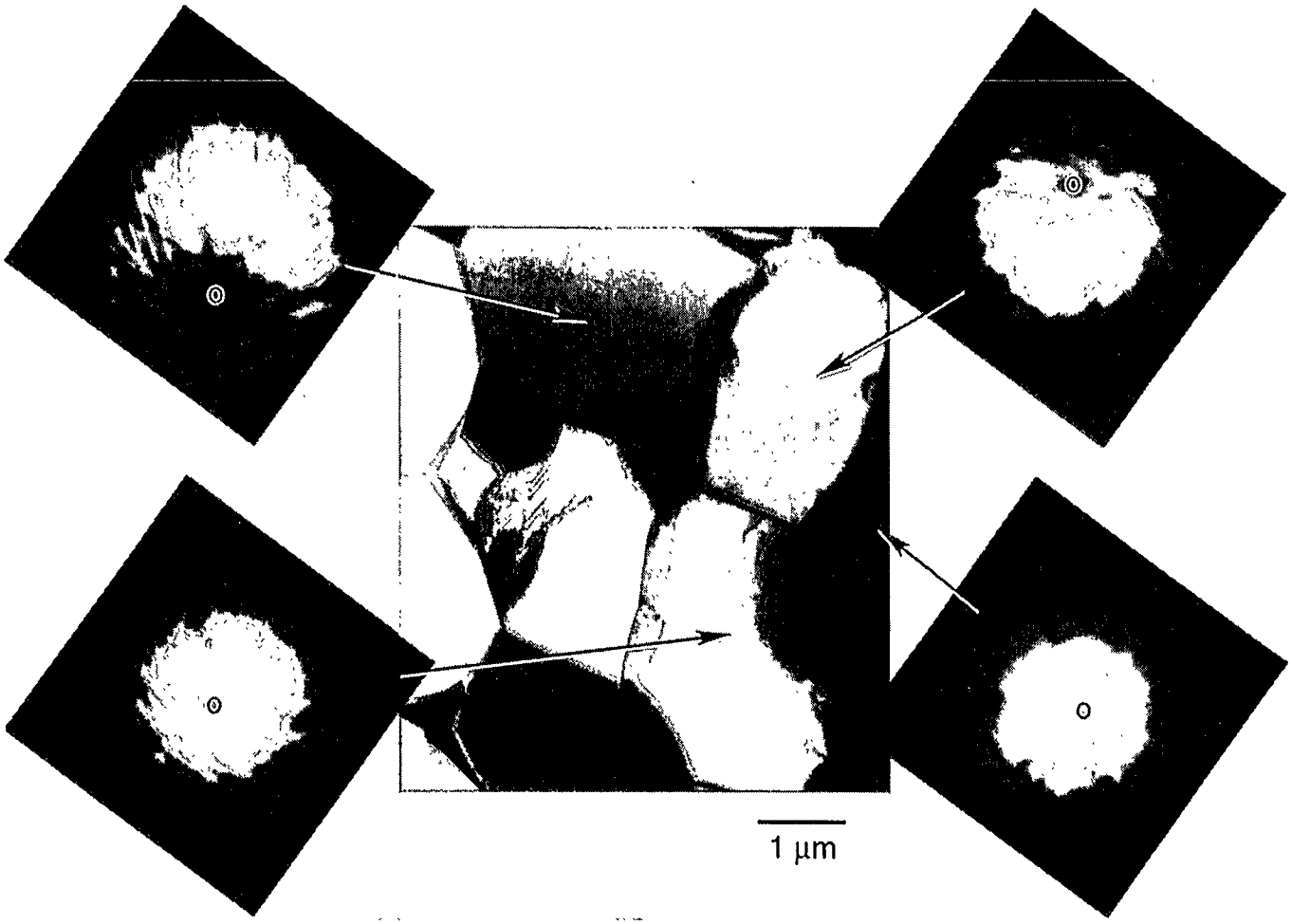

Figure 24: TEM micrograph of the recovered microstructure prior to deformation. Diffraction patterns show that the subgrain boundaries are low angle misorientations. The center of the [0$\bar{1}$1] zone axis is labelled by an O. Zone axis is near [0$\bar{1}$1]. (XBB 9408-5014)

Figure 25: TEM micrograph of the recovered microstructure prior to deformation. Note the existence of some dislocation substructure within the subgrain interior. Zone axis is near [0$\bar{1}$1]. (XBB 9408-4999)

Figure 26: TEM micrograph of the recovered microstructure prior to deformation. Note the existence of some dislocation substructure within the subgrain interior. Zone axis is near [0$\bar{1}$1]. (XBB 9408-4998)

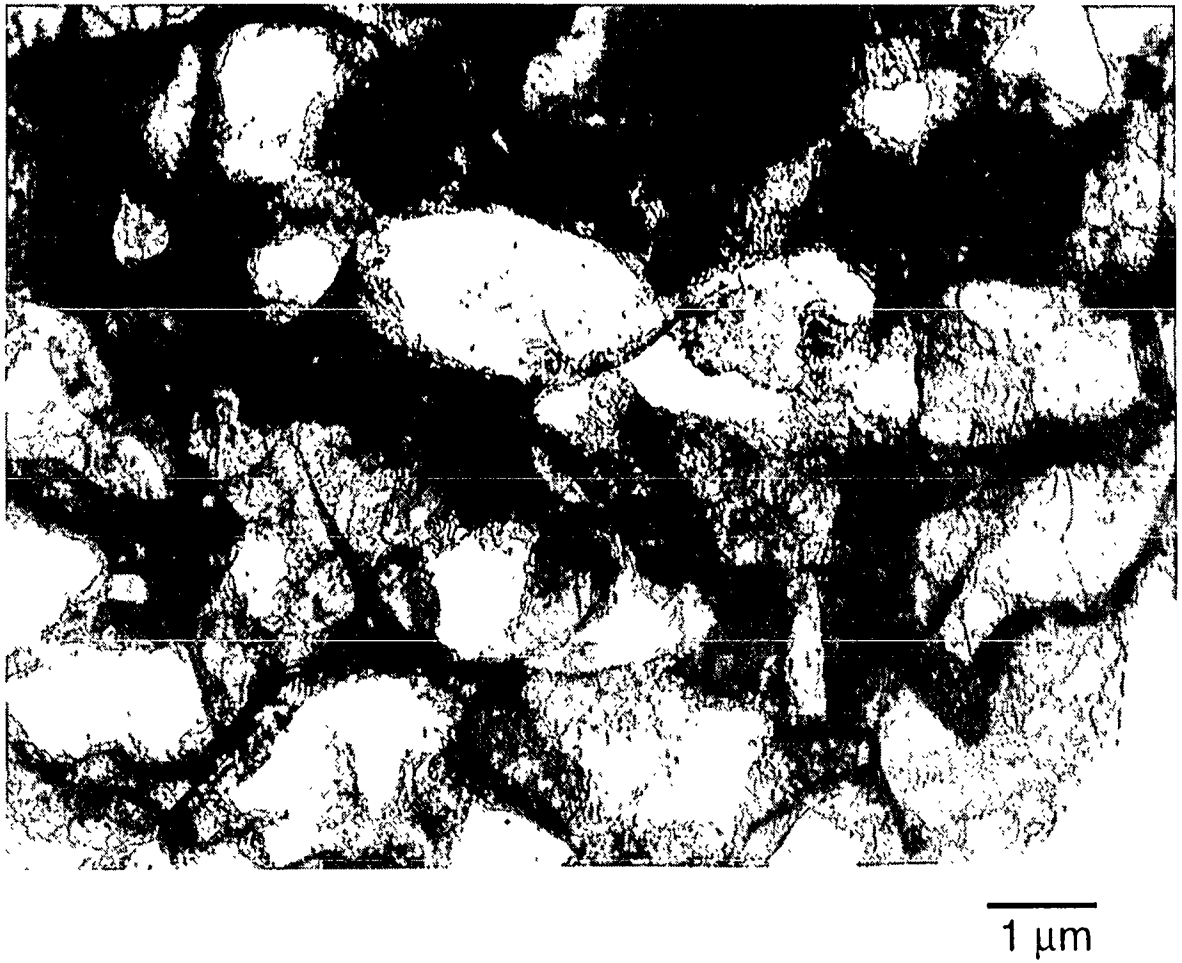

Figure 27: TEM micrograph of the recovered microstructure after deformation to a true stress of 226 MPa (32.8 ksi), approximately 21.8% true strain. Note the more random dislocation arrangement compared to the recrystallized microstructure upon straining in Figures 18 through 21. The majority of dislocations appear to accumulate at the subgrain boundaries. Some regions (upper left) exhibit a more homogeneous dislocation arrangement. Zone axis is [0$\bar{1}$1]. (XBB 9408-4994)

Figure 28: TEM micrograph of the recovered microstructure after deformation to a true stress of 226 MPa (32.8 ksi), approximately 21.8% true strain. Note the strong accumulation of dislocations at the subgrain boundaries. Zone axis is [0$\bar{1}$1]. (XBB 9408-4993)

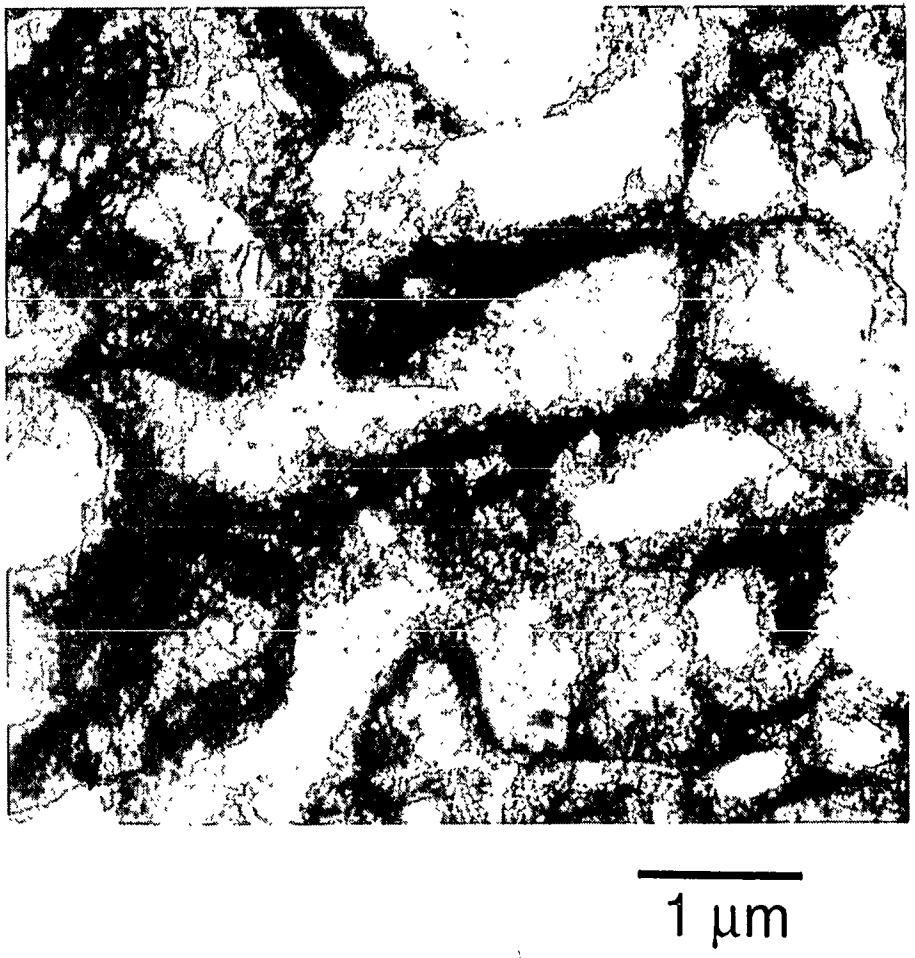

Figure 29: TEM micrograph of the recovered microstructure after deformation to a true stress of 226 MPa (32.8 ksi), approximately 21.8% true strain. The accumulation of dislocations is not as strong in this region as compared to Figure 28. However, the tendency for the dislocations to accumulate at the subgrain boundaries still exists. Zone axis is [0$\bar{1}$1]. (XBB 9408-4995)

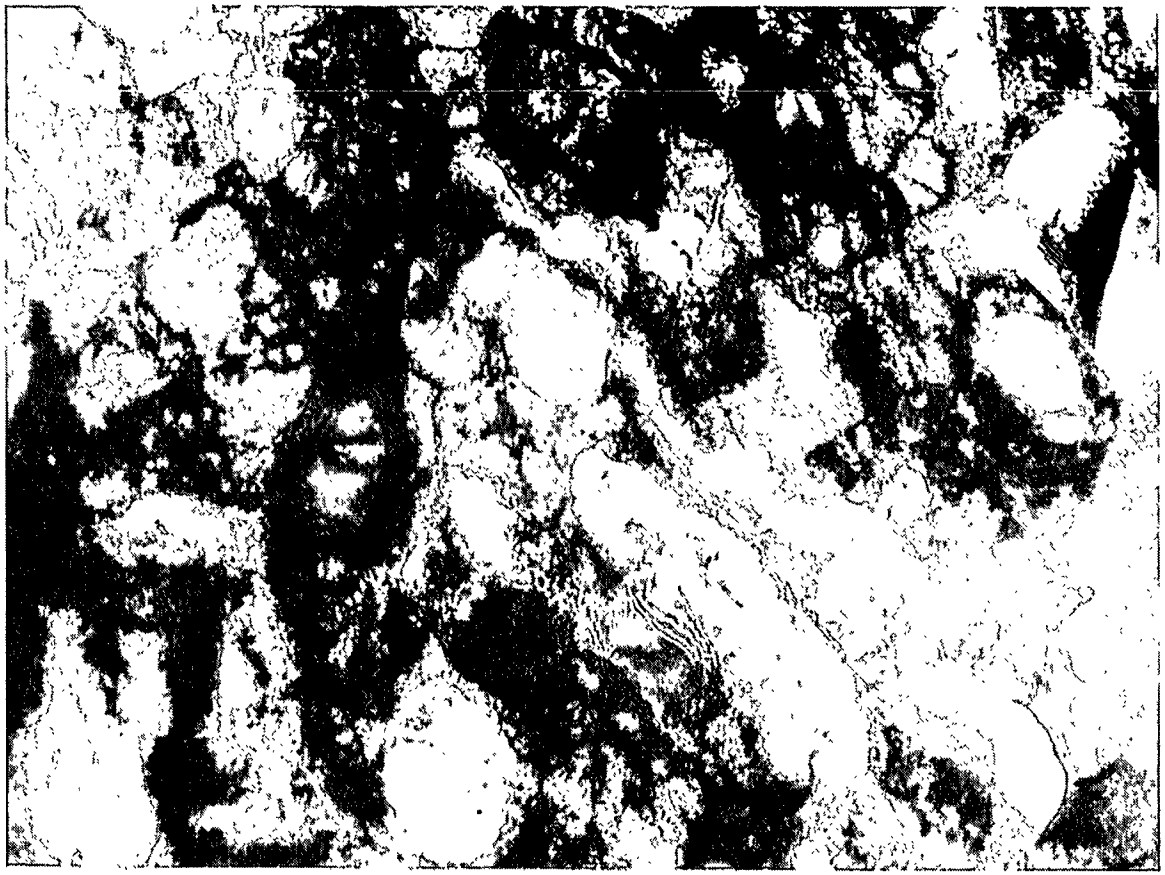

Figure 30: TEM micrograph of the unrecrystallized microstructure after deformation to a true stress of 226 MPa (32.8 ksi), approximately 14.1% true strain. Similar to the recovered microstructure, the dislocations tend to accumulate at the subgrain boundaries. Some regions (upper left) exhibit a more homogeneous dislocation arrangement. Zone axis is [011]. (XBB 9408-4990)

Figure 31: TEM micrograph of the unrecrystallized microstructure after deformation to a true stress of 226 MPa (32.8 ksi), approximately 14.1% true strain. Similar to the recovered microstructure, the dislocations tend to accumulate at the subgrain boundaries. Some regions (right hand side) exhibit a more homogeneous dislocation arrangement. Zone axis is [0$\bar{1}$1]. (XBB 9408-4988)

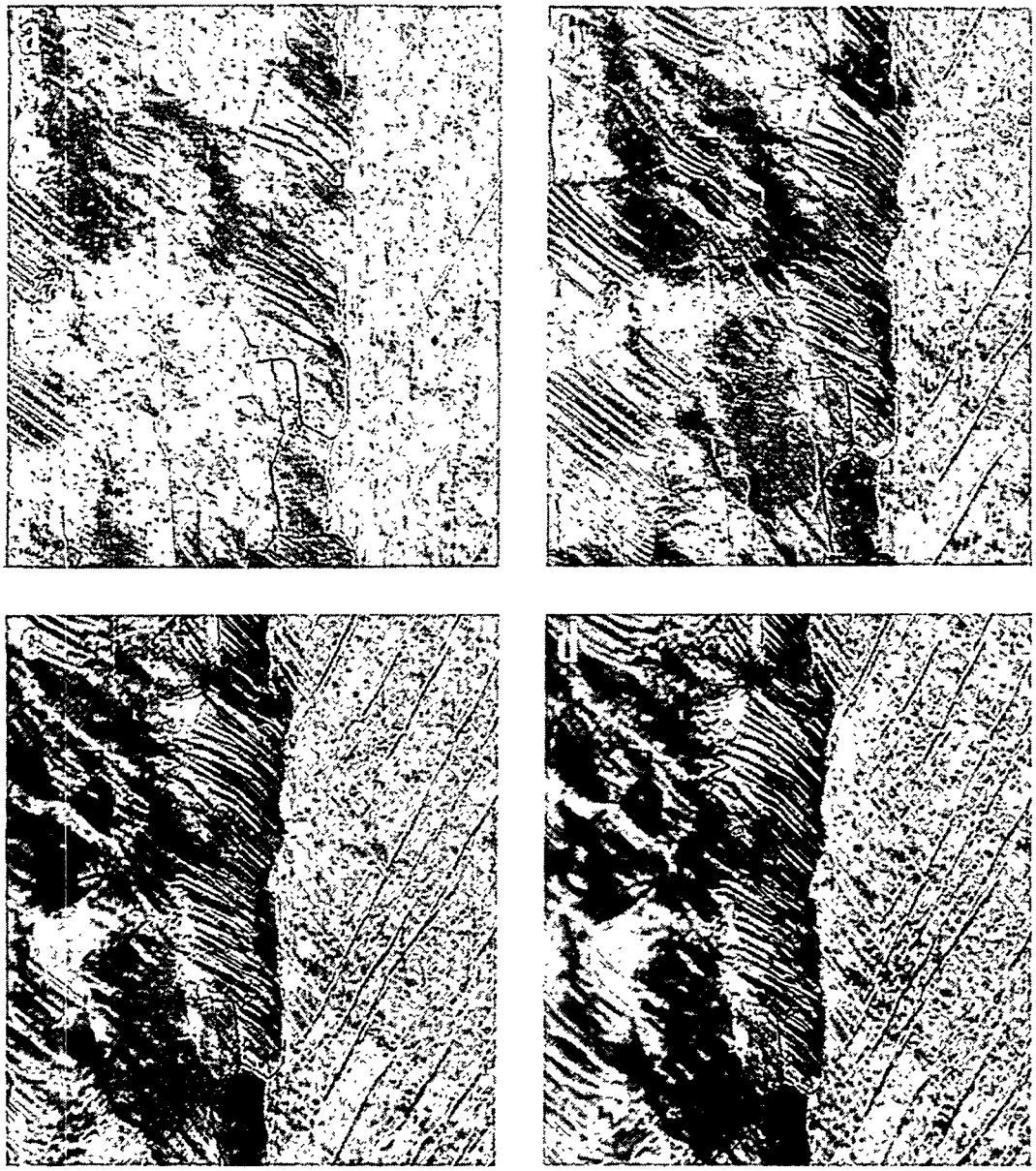

Figure 32: Optical micrograph of the partially recrystallized structure showing the evolution of deformation after a) 2% strain, b) 5% strain, c) 10% strain, and d) 15% strain. The recovered region is on the left side of each micrograph. Note that the recovered region exhibits greater out-of-plane rotation than the recrystallized region. (XBB 9306-3999)

Figure 33: TEM micrograph of the unrecrystallized microstructure prior to deformation. Note the existence of both narrow (A) and wide (B) dislocation bands across the subgrain interior. Zone axis is near [0$\bar{1}$1]. (XBD 9408-5103)

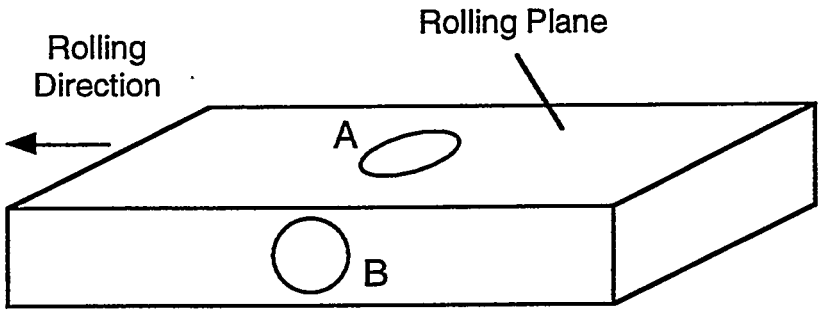

Figure 34: Schematic illustrating the difference between TEM specimen orientations between this study (A) and references 56, 75, 76, and 79 (B).

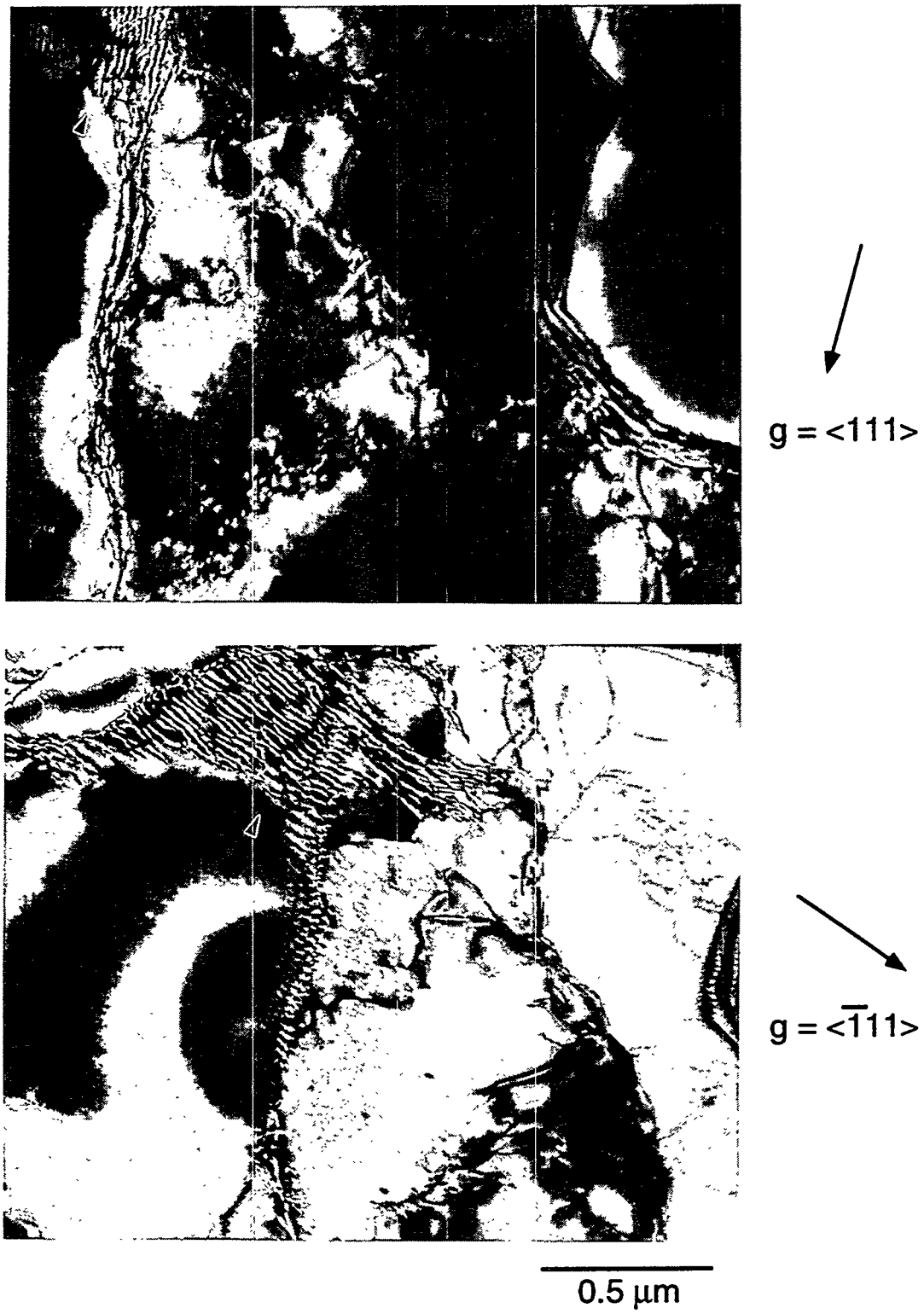

Figure 35: TEM micrographs of the unrecrystallized microstructure prior to deformation. Diffraction analysis of the wide dislocation band, indicated by the arrow, reveals the existence of at least two slip systems. The upper micrograph is offset to the left. Zone axis is near [0$\bar{1}$1]. (XBD 9408-5104)

Figure 36: TEM micrograph of the unrecrystallized microstructure after deformation to a true stress of 178 MPa (25.8 ksi), approximately 4.1% true strain. Much of the internal dislocation structure has dissolved (compare to Figures 30 and 31). Zone axis is [0$\bar{1}$1]. (XBB 9408-5101)

Figure 37: TEM micrograph of the recovered microstructure after deformation to a true stress of 178 MPa (25.8 ksi), approximately 10.1% true strain. Note the high degree of strain contrast indicating the high deformation activity at the subgrain boundaries. Dislocations generated from the subgrain boundaries can be seen at the arrows. Zone axis is [0$\bar{1}$1]. (XBD 9408-4989)

Figure 38: TEM micrograph of the recovered microstructure after deformation to a true stress of 178 MPa (25.8 ksi), approximately 10.1% true strain. The early stages of a dislocation network can be seen (upper right). Dislocations generated from the subgrain boundaries can be seen at the arrow. Zone axis is [0$\bar{1}$1]. (XBD 9408-4991)

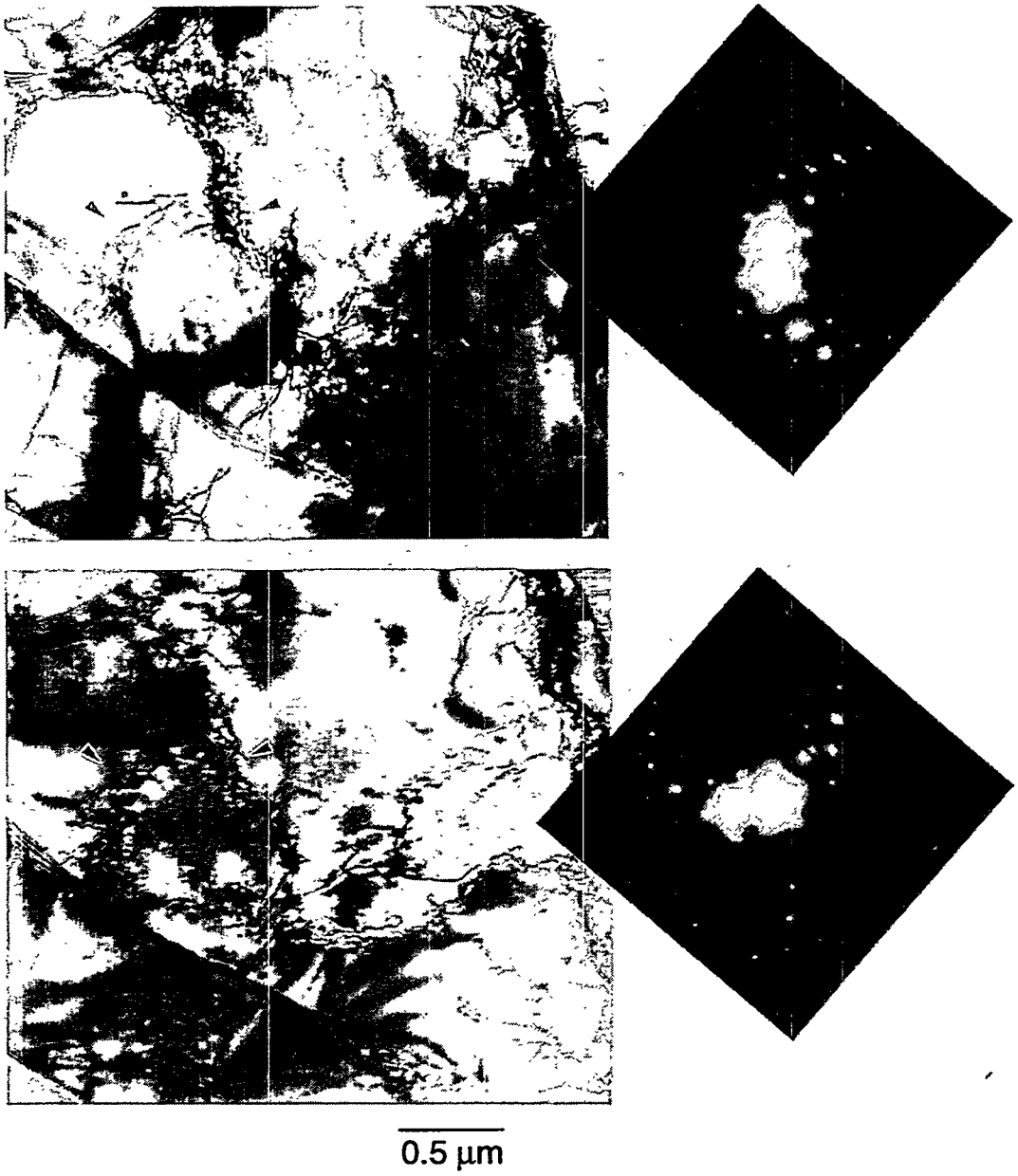

Figure 39: TEM micrograph of the recovered microstructure after deformation to a true stress of 178 MPa (25.8 ksi), approximately 10.1% true strain. Diffraction analysis indicates that the dislocation network, indicated by the arrows, consists of dislocations generated from the subgrain boundary. Zone axis is [0$\bar{1}$1]. (XBD 9408-5099)

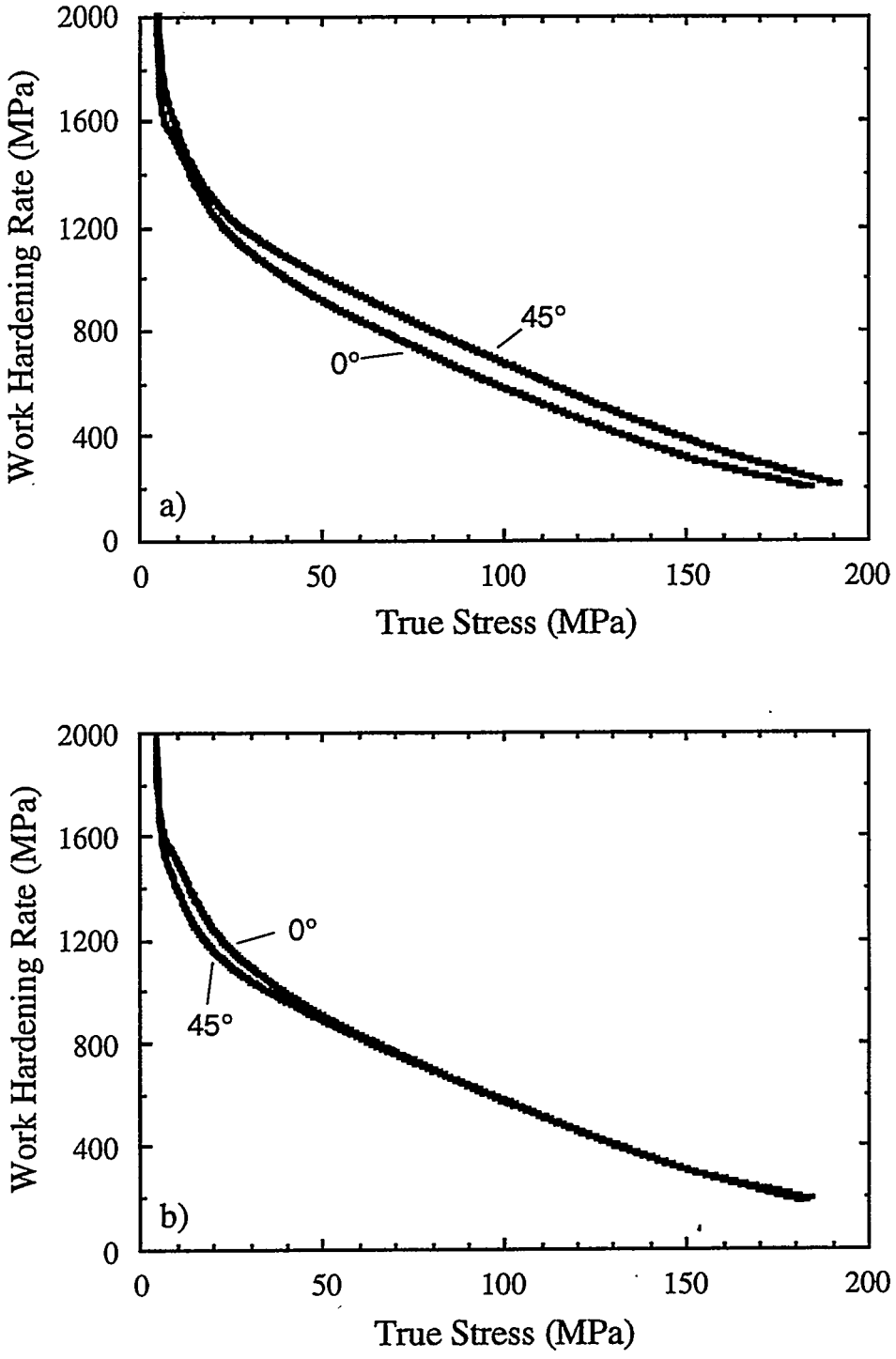

Figure 40: Plots of the work hardening rate versus true stress for LBL1 specimens in the recrystallized condition. Two curves represent specimens tested at different orientations relative to the rolling direction a) as tested and b) after recalculating the 45° plot ($\theta/1.05^2$ versus $\sigma/1.05$).

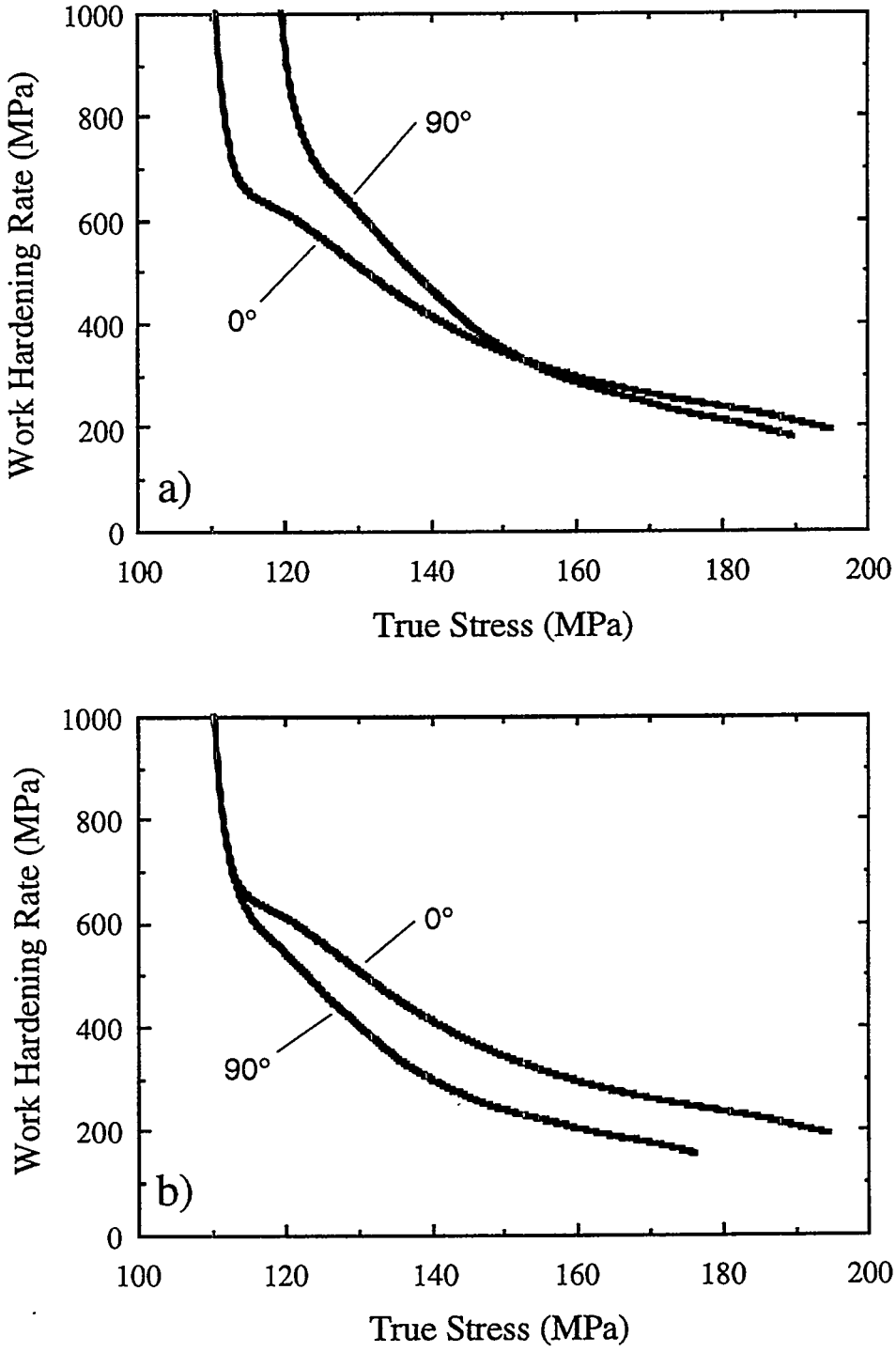

Figure 41: Plots of the work hardening rate versus true stress for LBL1 specimens in the unrecrystallized condition. Two curves represent specimens tested at different orientations relative to the rolling direction a) as tested and b) after recalculating the 90° plot ($\theta/1.08^2$ versus $\sigma/1.08$).

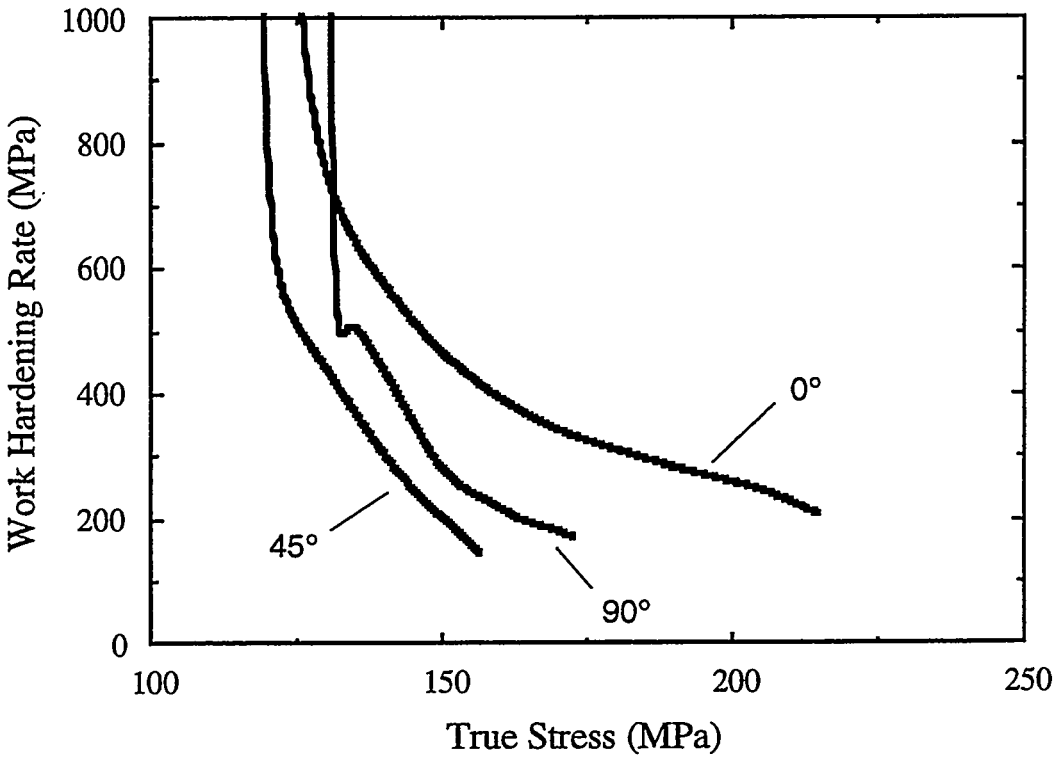

Figure 42: Plots of the work hardening rate versus true stress for LBL2 specimens in the unrecrystallized condition. Note the near parallel slope of the latter regimes of the 0° and 90° orientations.

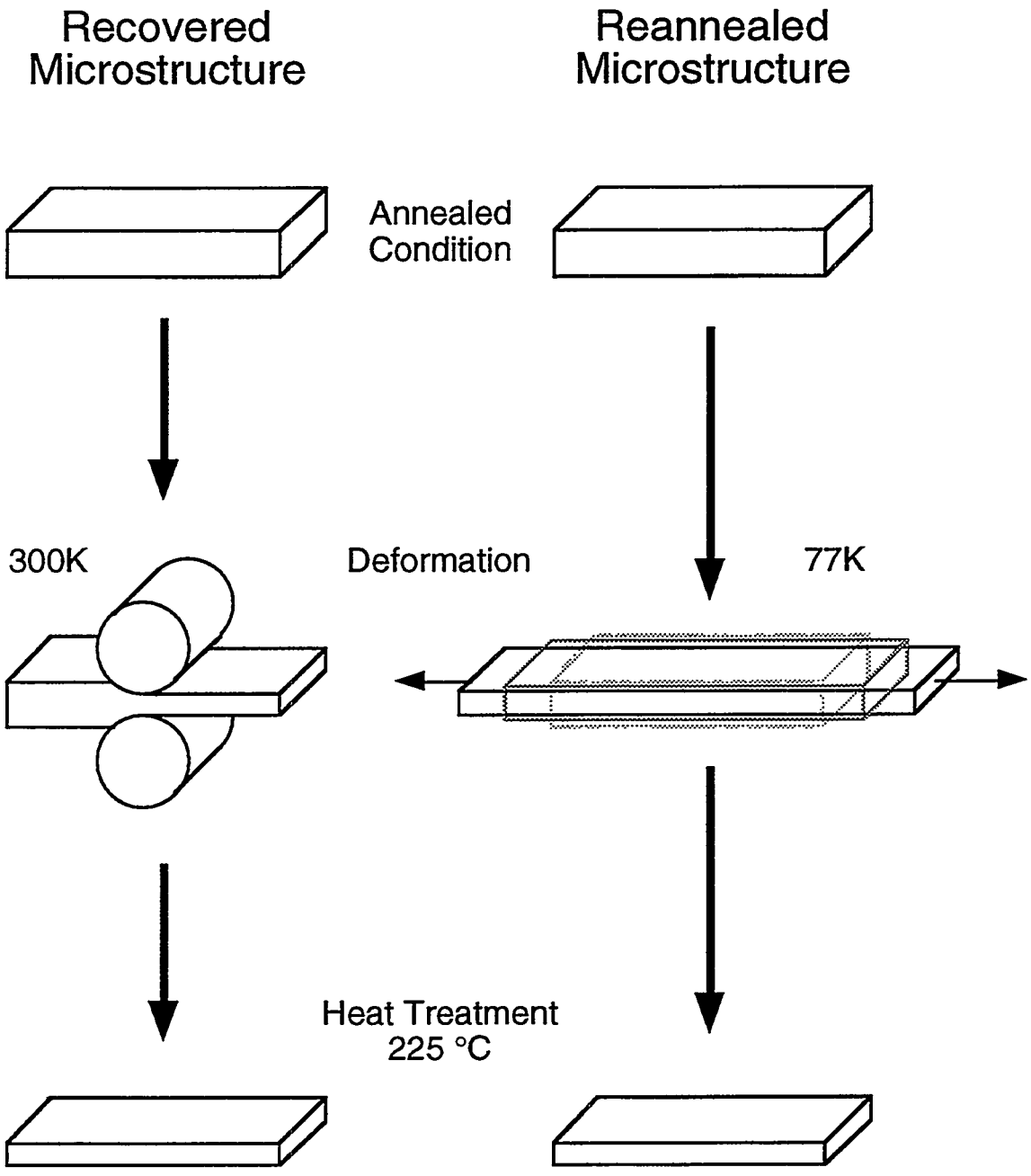

Figure 43: Schematic illustrating the difference between the recovered and reannealed microstructures. Both microstructures contain subgrains. However, the manner by which these subgrains are achieved differ.

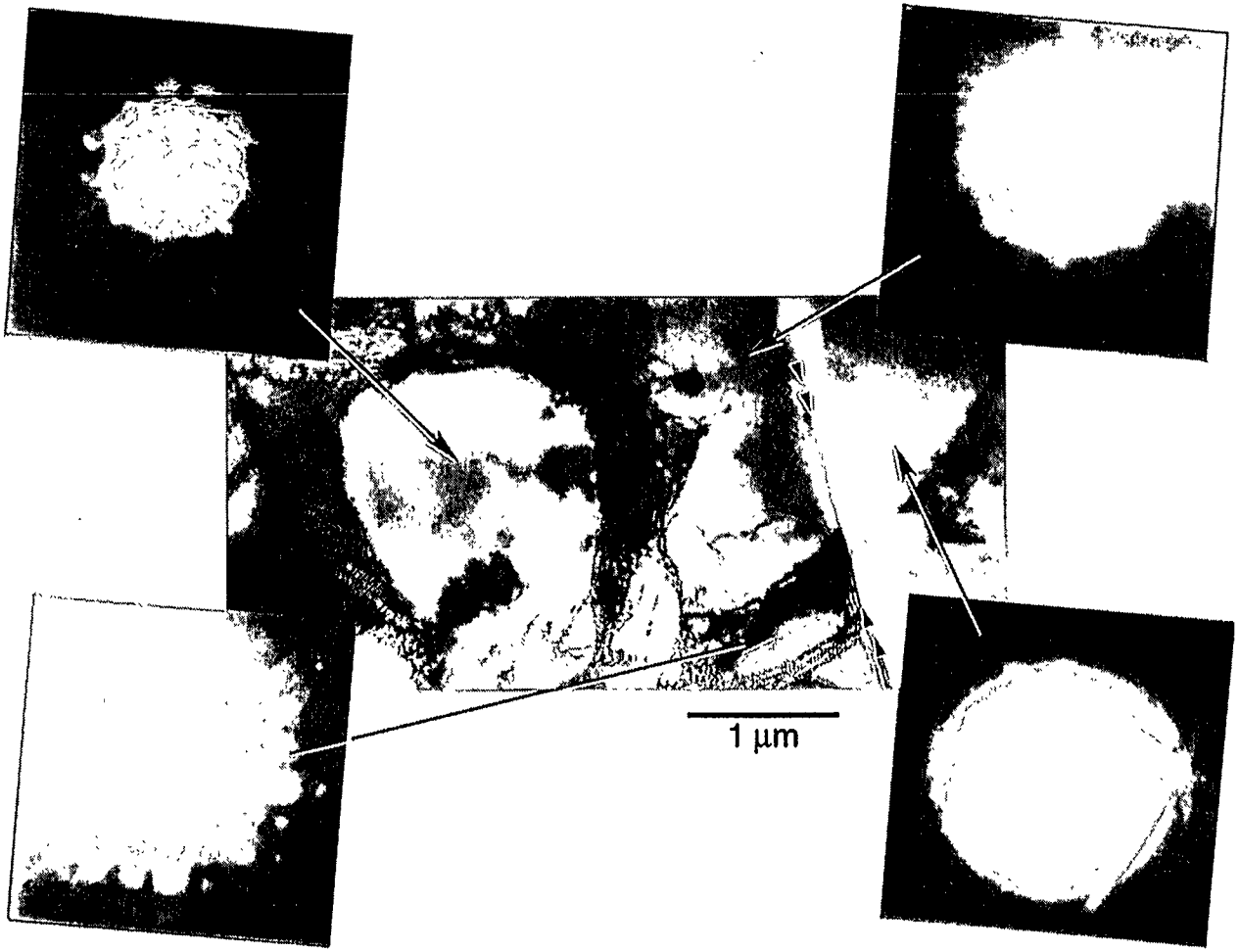

Figure 44: TEM micrograph of the reannealed microstructure prior to deformation. Note that the subgrains on the left are close in orientation with each other but exhibit a large misorientation across the grain boundary marked by arrows. Zone axis is near [001]. (XBD 9408-5010)

Figure 45: TEM micrograph of the reannealed microstructure prior to deformation. Most of the disocation cell structure has coalesced into subgrain boundaries. Lack of sharpness at the boundaries indicates an incomplete recovery process. Compare to Figures 18 through 21. Zone axis is near [001]. (XBB 9408-5009)

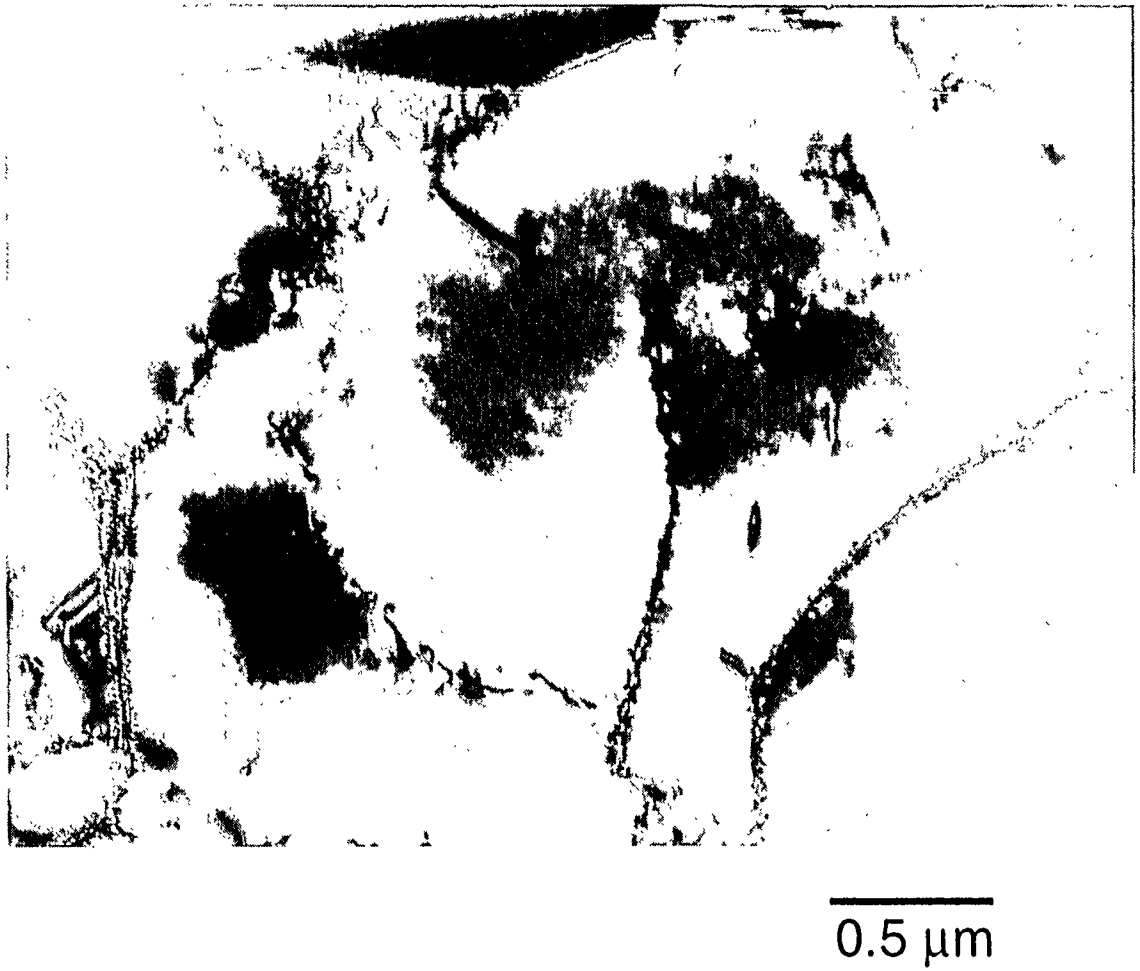

Figure 46: TEM micrograph of the reannealed microstructure prior to deformation. Most of the disocation cell structure has coalesced into subgrain boundaries. Lack of sharpness at the boundaries indicates an incomplete recovery process. Compare to Figures 18 through 21. Zone axis is near [001]. (XBB 9408-5008)

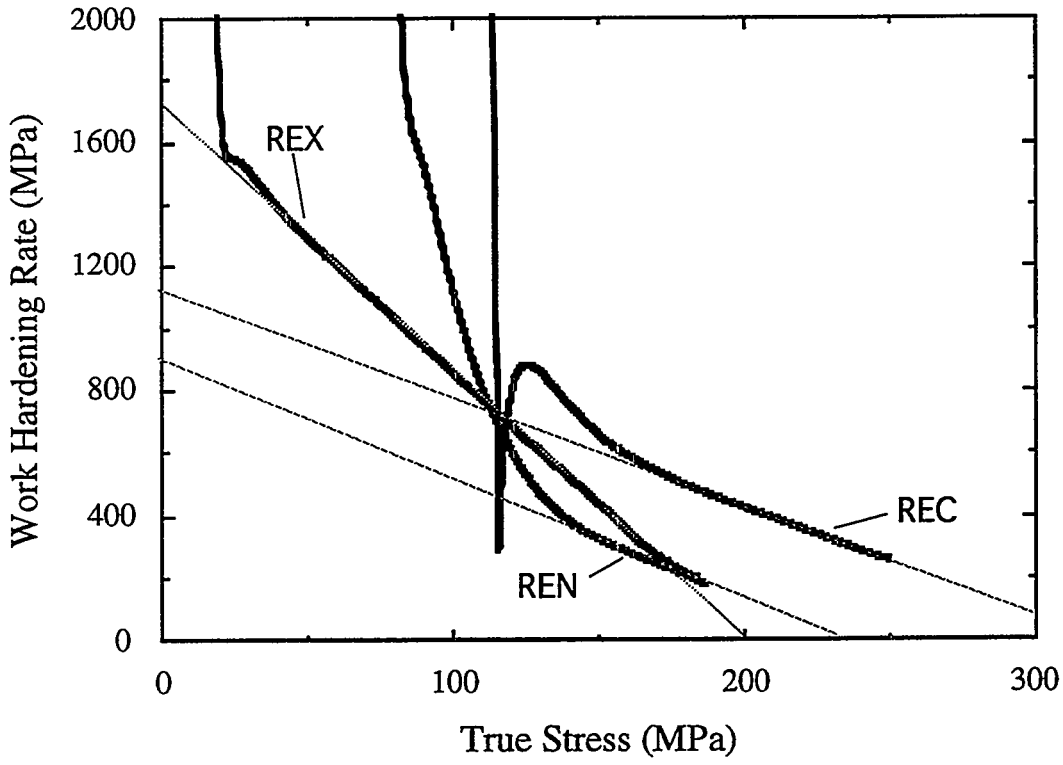

Figure 47: Plot of the work hardening rate versus true stress for the recovered (REC), recrystallized (REX), and reannealed (REN) microstructures. Slopes of the latter regime for the three microstructures are highlighted by the dashed lines. Note that the latter regime of the reannealed microstructure follows nearly parallel to the recovered microstructure.

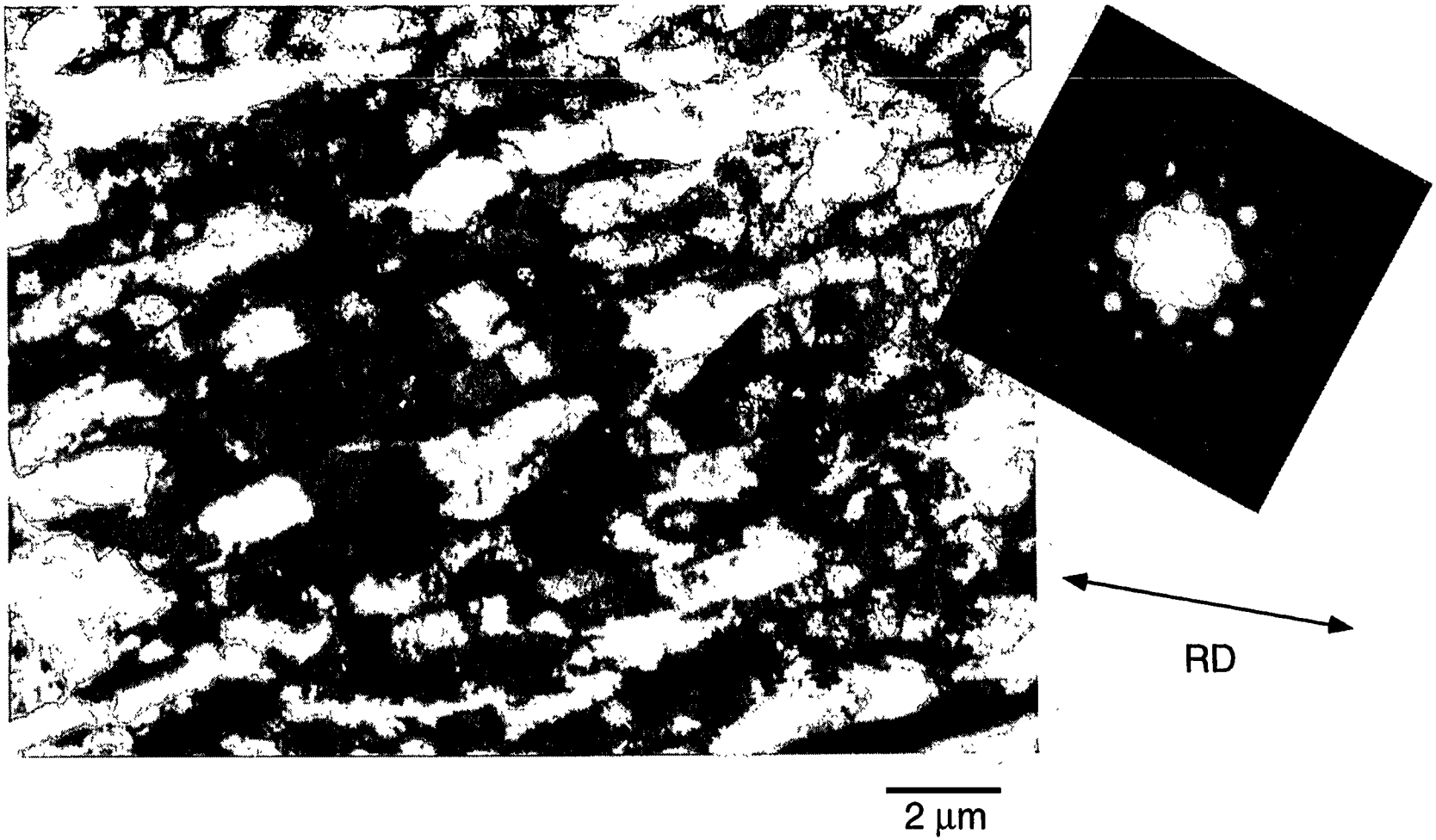

Figure 48: TEM micrograph of the reannealed microstructure after deformation to a true stress of 189 MPa (27.4 ksi), approximately 25.1% true strain. Note the absence of a cellular dislocation structure. Dislocations accumulate at the subgrain boundaries similar to the recovered and unrecrystallized microstructure after deformation. Compare to Figures 27 through 31. Zone axis is [001]. (XBB 9408-5005)

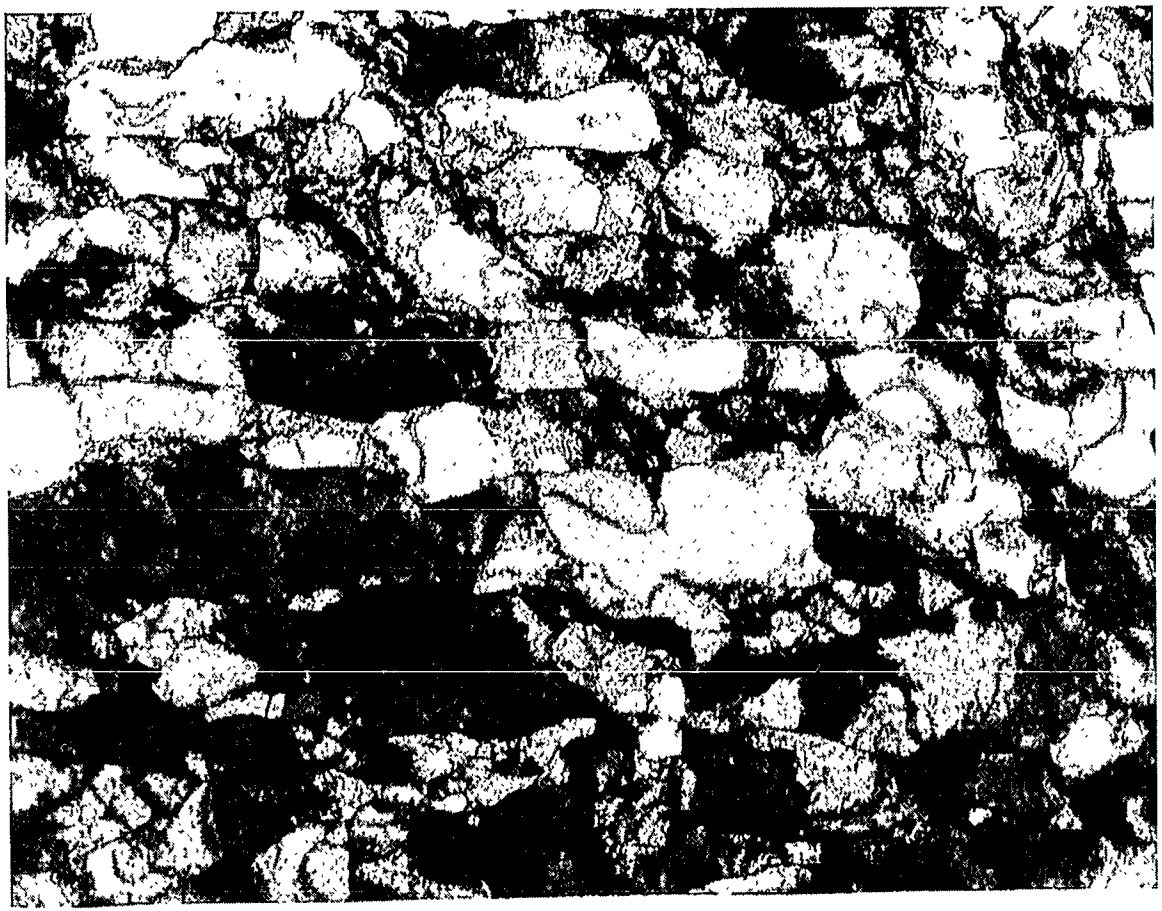

Figure 49: TEM micrograph of the recovered microstructure after deformation to a true stress of 189 MPa (27.4 ksi), approximately 25.1% true strain. Note the absence of a cellular dislocation structure. Dislocations accumulate at the subgrain boundaries similar to the recovered and unrecrystallized microstructure after deformation. Compare to Figures 27 through 31. Zone axis is [001]. (XBB 9408-5004)

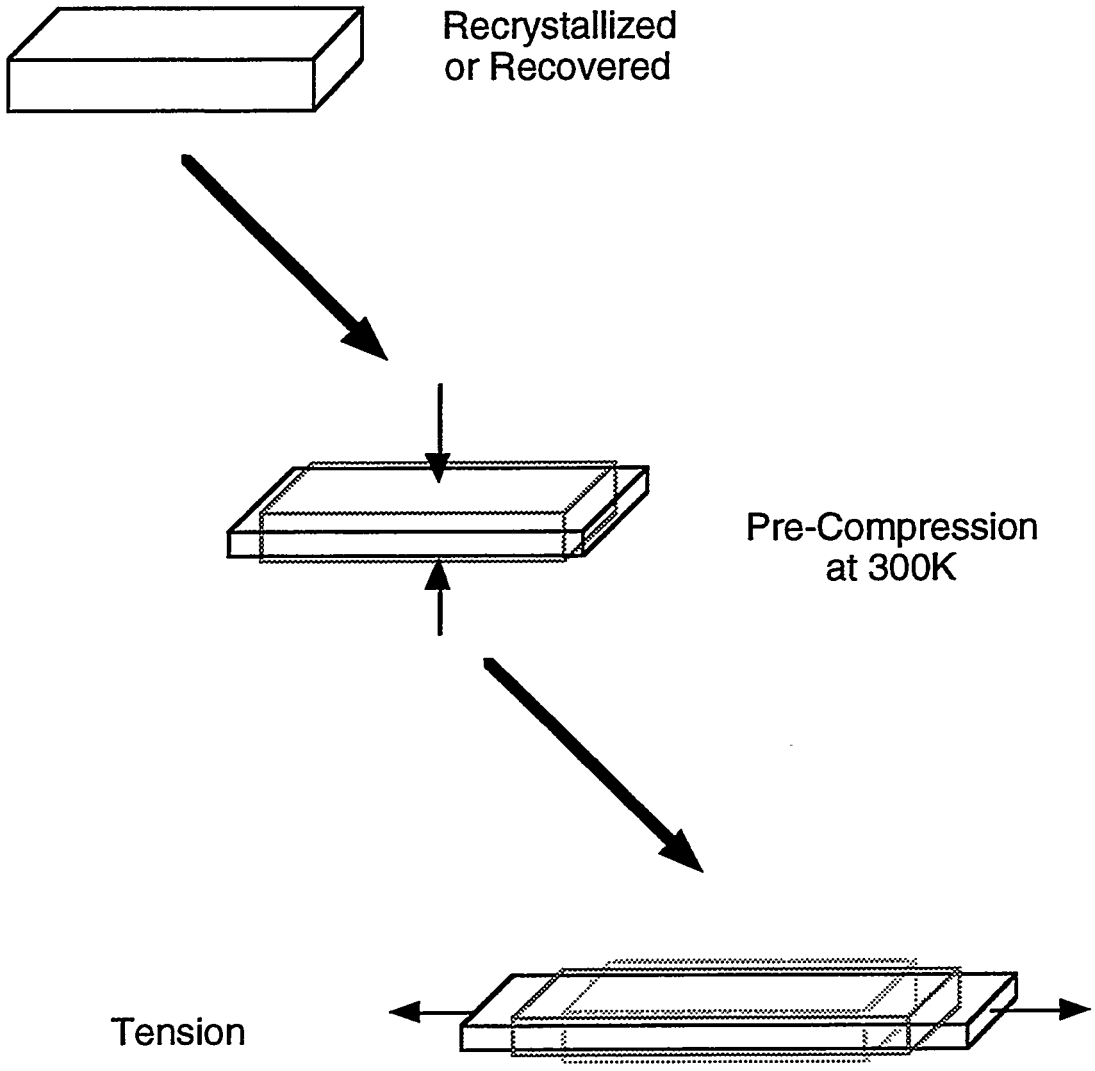

Figure 50: Schematic illustrating the strain path of the pre-compressed specimens. Compare to Figure 43.

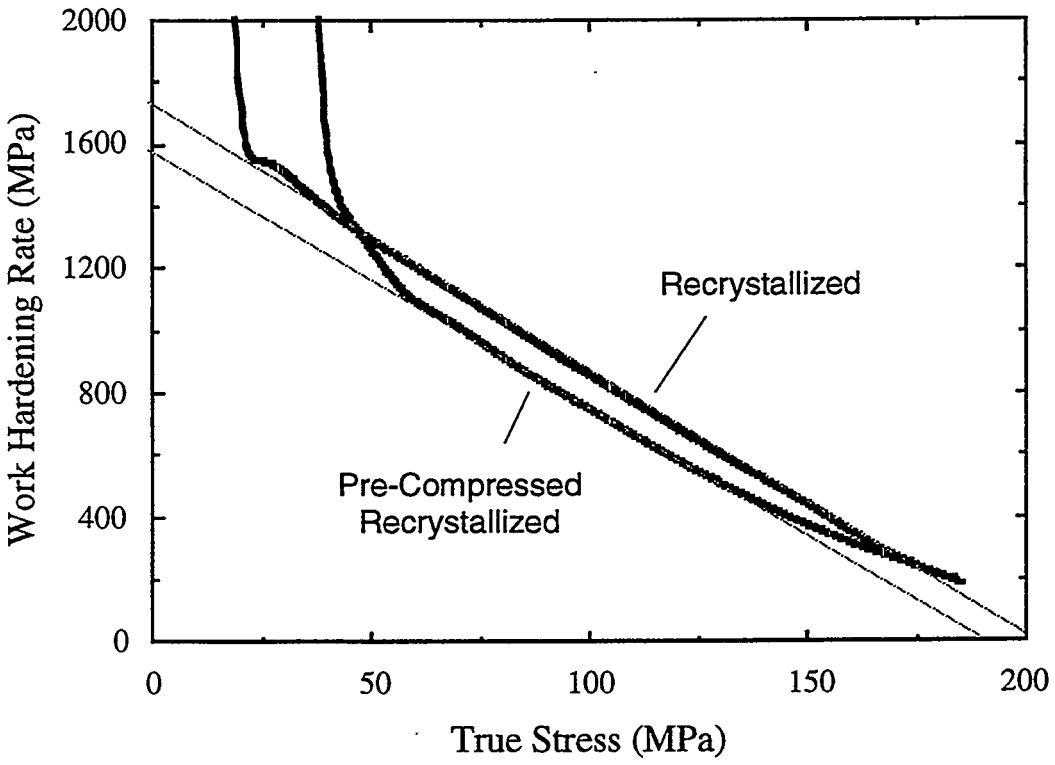

Figure 51: Plot of the work hardening rate versus true stress for the recrystallized and the pre-compressed recrystallized microstructures. Slopes of the latter regime for the two microstructures are highlighted by the dashed lines. Note the existence of a greater early regime in the pre-compressed microstructure.

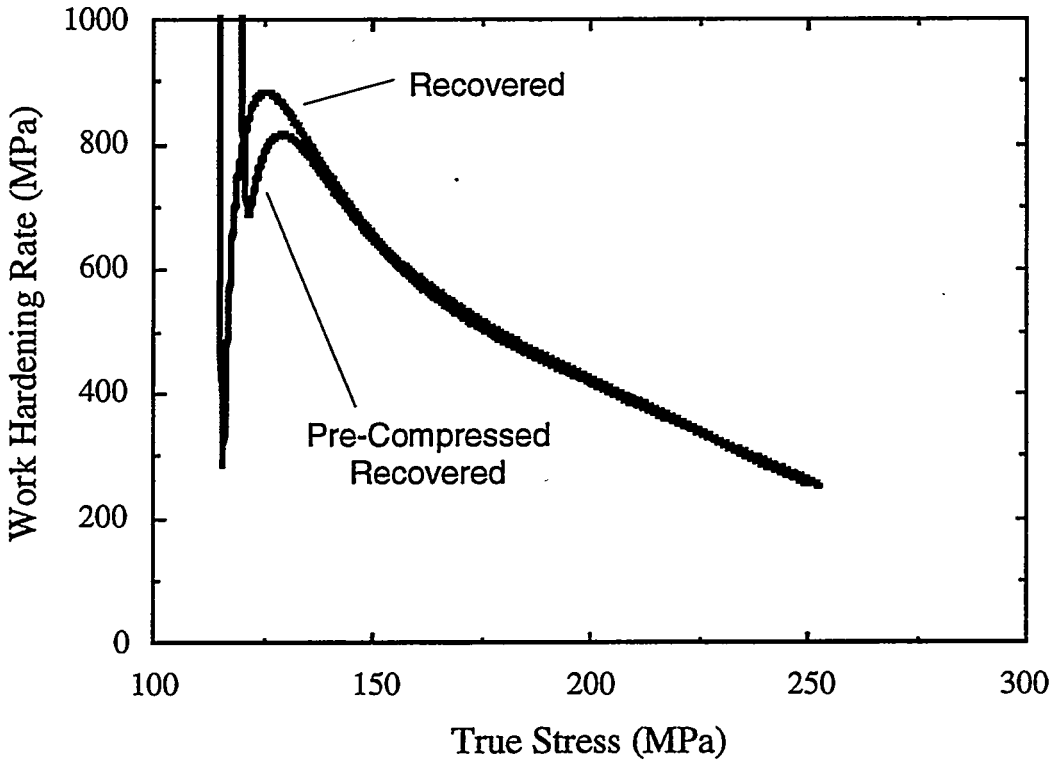

Figure 52: Plot of the work hardening rate versus true stress for the recovered and the pre-compressed recovered microstructures. Aside from a slight difference in the early regime, the work hardening curves for both microstructures are nearly identical.

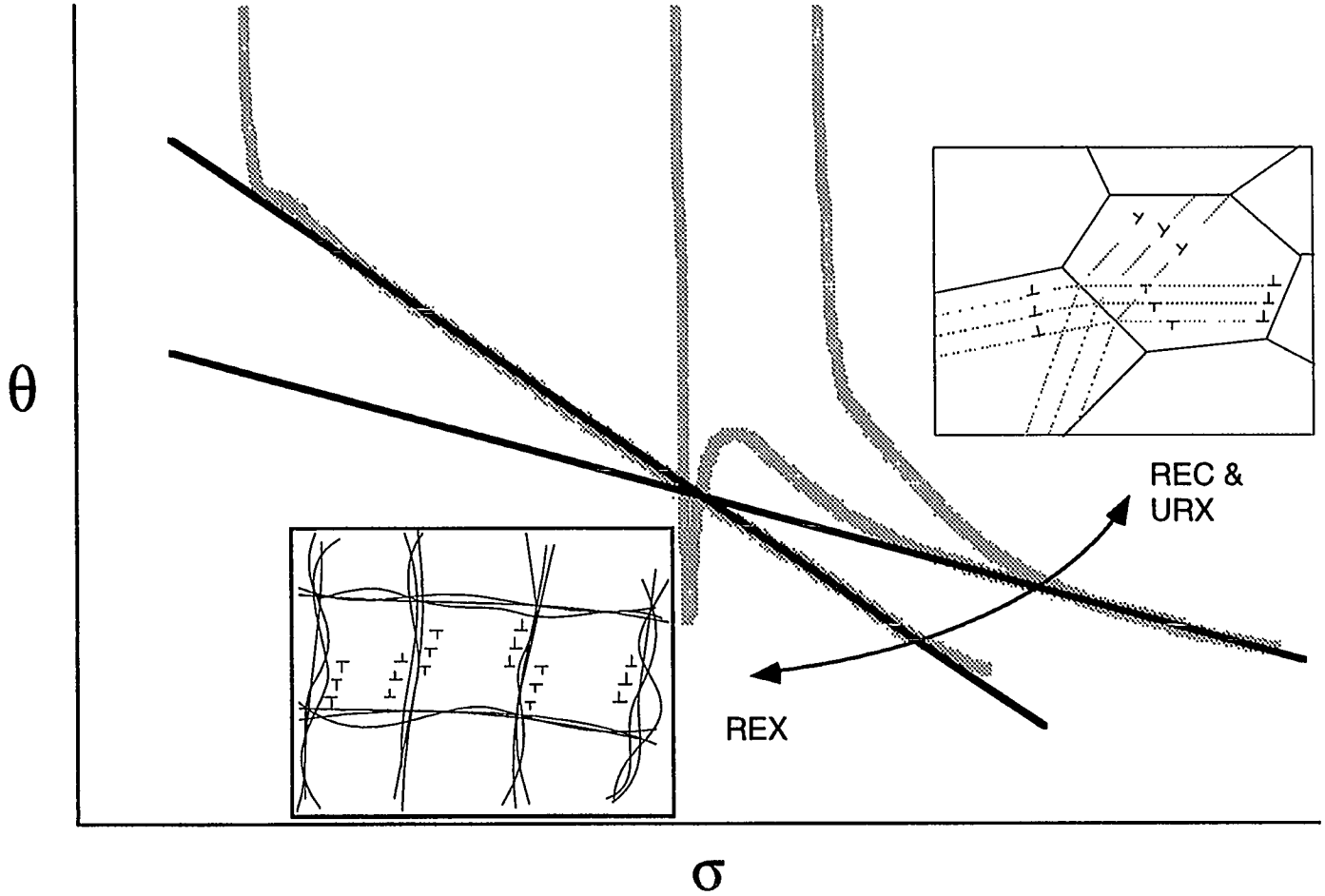

Figure 53: Schematic illustrating the different evolutionary paths of the dislocation network. The cellular dislocation structure that develops in the recrystallized microstructure allows for a higher dynamic recovery rate and steeper drop in the work hardening rate with stress. The subgrain morphology inherent to the recovered and unrecrystallized microstructures eliminates the cellular dislocation structure, reducing the dynamic recovery rate.

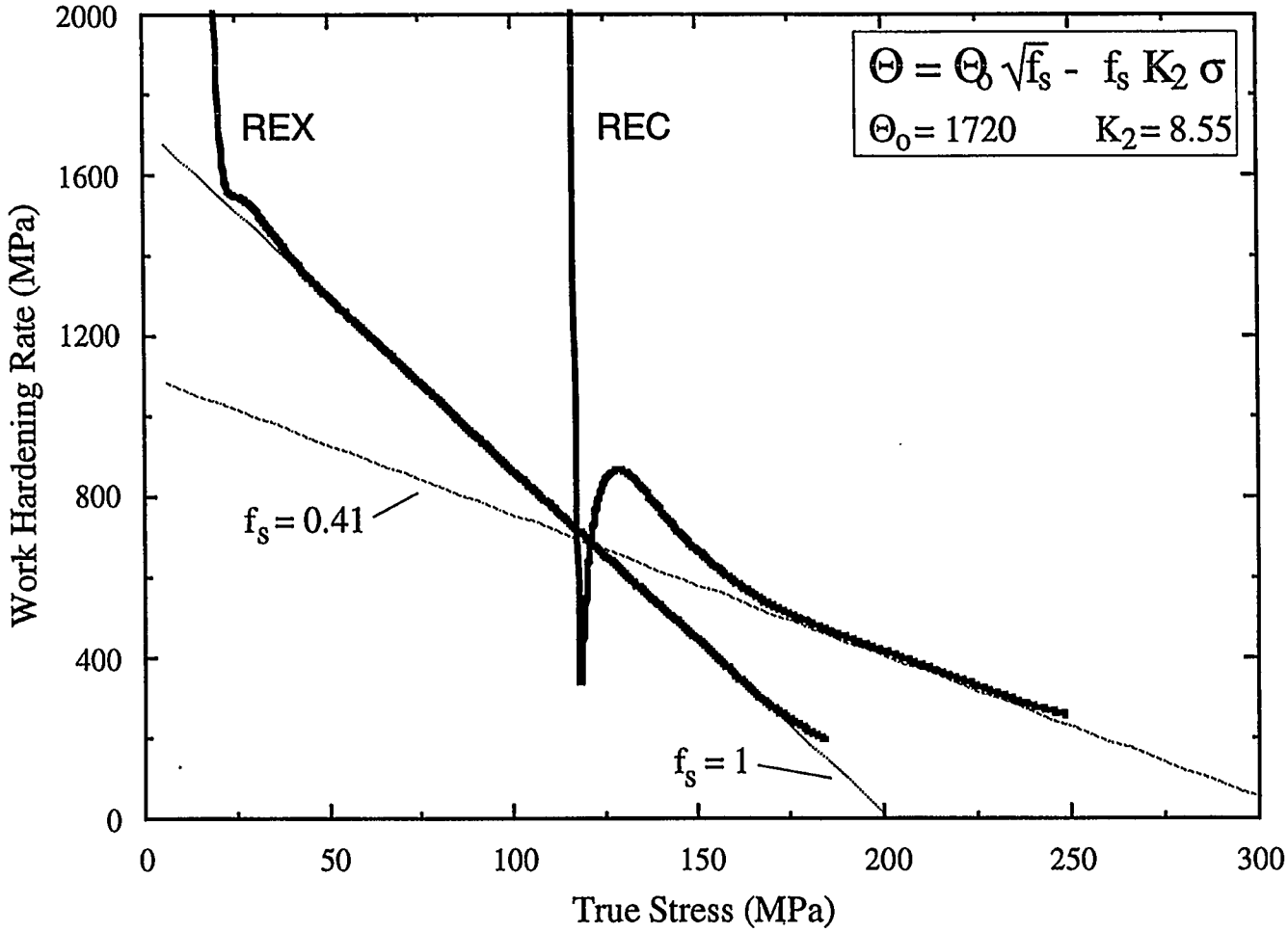

Figure 54: Plot of the work hardening rate versus true stress for the recrystallized (REX) and recovered (REC) microstructures. Shaded lines are calculated using Equation (50). Note the excellent fit of the predicted work hardening behavior for the recovered microstructure.

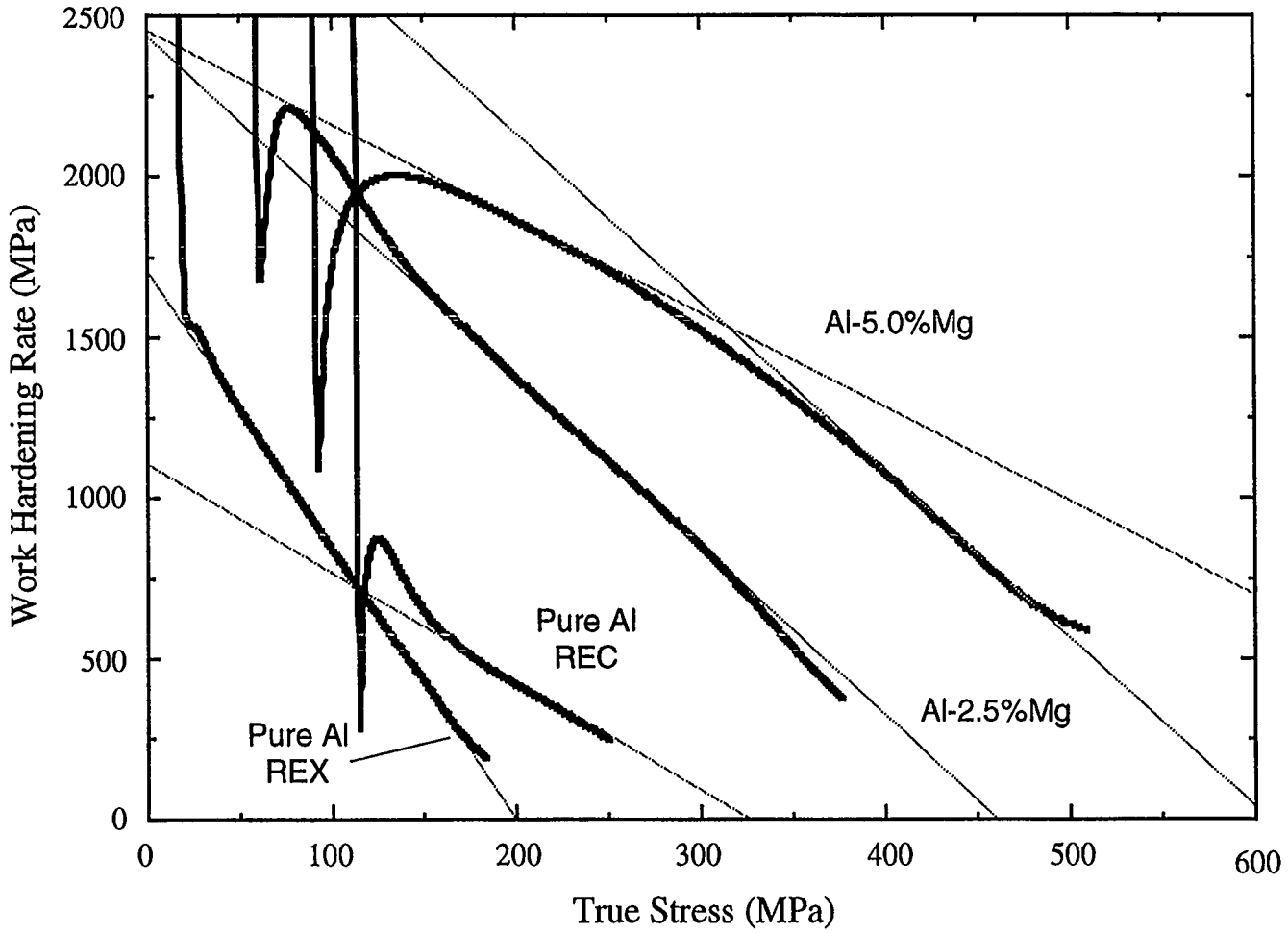

Figure 55: Plot of the work hardening rate versus true stress for the magnesium-bearing solid solutions and pure aluminum samples in the recrystallized (REX) and recovered (REC) conditions. Shaded lines represent the linear approximations used to obtain the parameters in Table XIII. Note that the addition of solutes accomplishes the same effect as the introduction of subgrains.

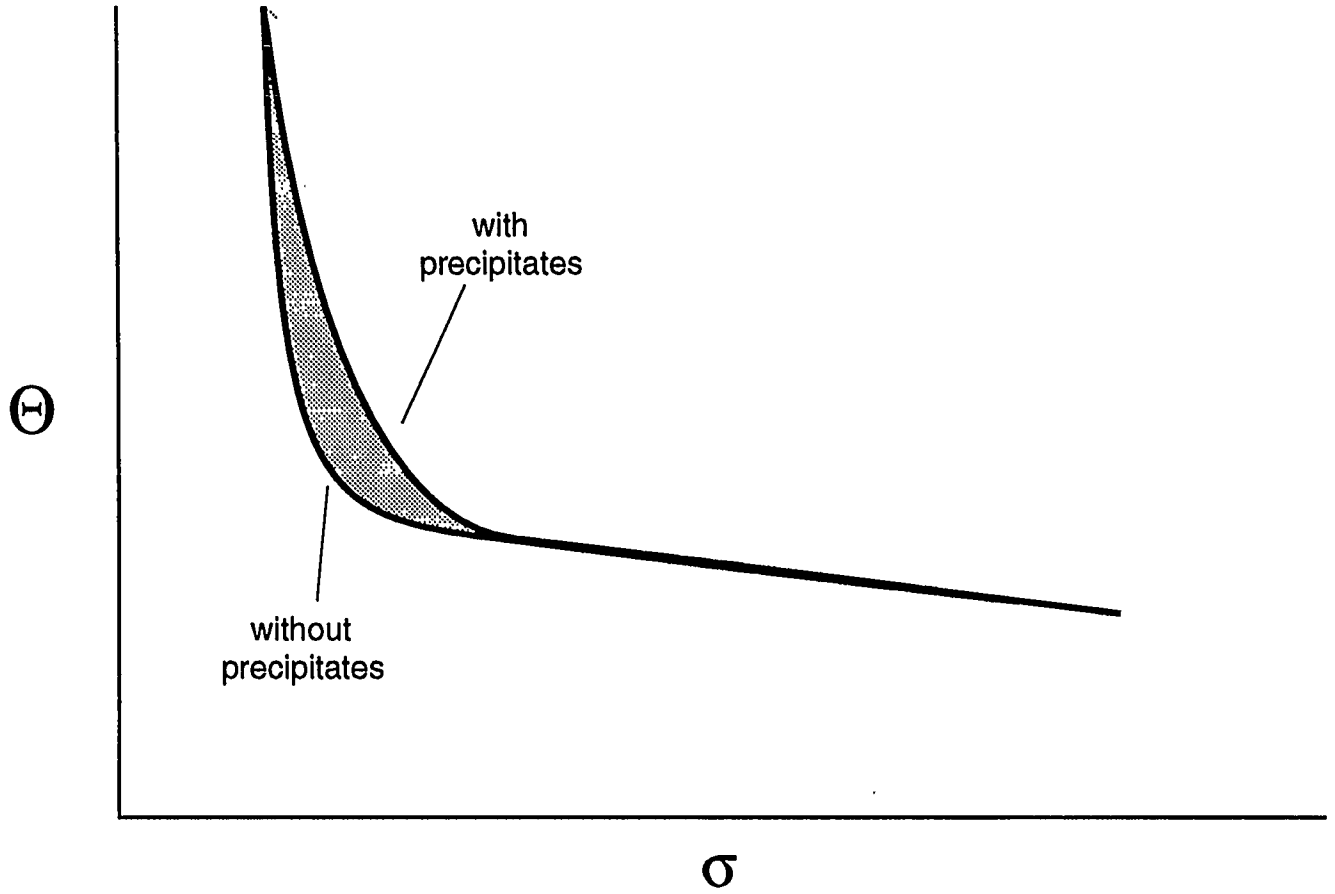

Figure 56: Schematic illustrating the influence of precipitates on the very-early work hardening regime. An decrease in the slope of the very-early work hardening regime is typically observed with the addition of precipitates. The shaded area indicates the loss in uniform elongation which results with this decrease (Equation (54)).